NANYANG TECHNOLOGICAL UNIVERSITY
SINGAPORE

BEHAVIOUR AND DESIGN OF HOT-ROLLED STAINLESS STEEL CHANNEL SECTION MEMBERS

LI SHUAI

SCHOOL OF CIVIL AND ENVIRONMENTAL ENGINEERING

2022

Behaviour and Design of Hot-Rolled Stainless Steel Channel Section Members

Li Shuai

School of Civil and Environmental Engineering

A thesis submitted to the Nanyang Technological University in partial fulfilment of the requirement for the degree of Doctor of Philosophy

2022

Statement of Originality

I hereby certify that the work embodied in this thesis is the result of original research, is free of plagiarised materials, and has not been submitted for a higher degree to any other University or Institution.

5/12/2022

. . . . . .

Date

LI SHUAI

. . . . . .

Li Shuai

Supervisor Declaration Statement

I have reviewed the content and presentation style of this thesis and declare it is free of plagiarism and of sufficient grammatical clarity to be examined. To the best of my knowledge, the research and writing are those of the candidate except as acknowledged in the Author Attribution Statement. I confirm that the investigations were conducted in accord with the ethics policies and integrity standards of Nanyang Technological University and that the research data are presented honestly and without prejudice.

5/12/2022

. . . . . .

Date

. . . . . .

Zhao Ou

Authorship Attribution Statement

This thesis contains material from 8 papers published in the following peer-reviewed journals in which I am listed as an author.

Chapter 3 is published as Lan, X., Li, S., and Zhao, O. Local buckling of hot-rolled stainless steel channel section stub columns after exposure to fire. *Journal of Constructional Steel Research*, 187, 106950 (2021). DOI: 10.1016/j.jcsr.2021.106950.

The contributions of the co-authors are as follows:

- Asst Prof Zhao provided the initial project direction and financial support.
- I co-designed the tests with Asst Prof Zhao and conducted all the laboratory work at the School of Civil and Environmental Engineering. I also analysed the data with Dr Lan.
- I performed the numerical modelling and design analyses.

Chapter 4 is published as

(i) Li, S., Zhang, L., and Zhao, O. Cross-section behavior and design of hot-rolled stainless steel channel sections under major-axis combined loading. *Journal of Structural Engineering (ASCE)*, 148, 04022110 (2022). DOI: 10.1061/(ASCE)ST.1943-541X.0003409.

(ii) Li, S., Su, A., Zhao, O. Post-fire behaviour and residual resistance of hot-rolled stainless steel channel sections under major-axis combined loading. *Engineering Structures*, 275, 115202 (2023). DOI: 10.1016/j.engstruct.2022.115202.

(iii) Li, S., Su, A., Zhao, O. Cross-section behaviour of press-braked ferritic stainless steel channel sections under combined compression and major-axis bending moment. *Thin-Walled Structures*, 188, 110775 (2023). DOI: 10.1016/j.tws.2023.110775.

The contributions of the co-authors are as follows:

- Asst Prof Zhao provided the initial project direction and financial support.
- I co-designed the tests with Asst Prof Zhao and conducted all the laboratory work at the School of Civil and Environmental Engineering. I also analysed the data with Dr Su.
- I performed the numerical modelling and design analyses.
- I prepared the original manuscript draft, which was revised by Asst Prof Zhao.
- Dr Zhang provided guidance in the interpretation of the experimental results.

Chapter 5 is published as

(i) Li, S., Zhang, L., and Zhao, O. Testing, modelling and design of hot-rolled stainless steel channel sections under combined compression and minor-axis bending moment. *Thin-Walled Structures*, 172, 108836 (2022). DOI: 10.1016/j.tws.2021.108836.

(ii) Li, S., and Zhao, O. Local buckling and capacity of press-braked ferritic stainless steel channel sections under minor-axis combined loading. *Thin-Walled Structures*, 178, 109507 (2022). DOI: 10.1016/j.tws.2022. 109507.

The contributions of the co-authors are as follows:

- Asst Prof Zhao provided the initial project direction and financial support.
- I co-designed the tests with Asst Prof Zhao and conducted all the laboratory work at the School of Civil and Environmental Engineering. I also analysed the data with Dr Zhang.
- I performed the numerical modelling and design analyses.
- I prepared the original manuscript draft, which was revised by Asst Prof Zhao.

Chapter 6 is published as

(i) Li, S., Zhang, L., Liang, Y., and Zhao, O. Experimental and numerical investigations of hot-rolled stainless steel channel section columns susceptible to flexural buckling. *Thin-Walled Structures*, 164, 107791 (2021). DOI:

10.1016/j.tws.2021.107791.

(ii) Li, S., and Zhao, O. Local–flexural interactive buckling behaviour and resistance of press-braked stainless steel slender channel section columns. *Engineering Structures*, 270, 114871 (2022). DOI: 10.1016/j.engstruct.2022.114871.

(iii) Li, S., and Zhao, O. Testing, simulation and design of press-braked ferritic stainless steel slender channel section columns failing by local–flexural interactive buckling. *Thin-Walled Structures*, 185, 110621 (2023). DOI: 10.1016/j.tws.2023.110621.

(iv) Li, S., and Zhao, O. Flexural buckling behaviour and residual resistances of hot-rolled stainless steel channel section columns after exposure to elevated temperatures. *Engineering Structures*, accepted (2023).

The contributions of the co-authors are as follows:

- Asst Prof Zhao provided the initial project direction and financial support.
- I co-designed the tests with Asst Prof Zhao and conducted all the laboratory work at the School of Civil and Environmental Engineering. I also analysed the data with Dr Zhang.
- I performed the numerical modelling and design analyses.
- I prepared the original manuscript draft, which was revised by Dr Liang and Asst Prof Zhao.

Chapter 7 is published as

(i) Li, S., Zhang, L., and Zhao, O. Global buckling and design of hot-rolled stainless steel channel section beam–columns. *Thin-Walled Structures*, 170, 108433 (2022). DOI: 10.1016/j.tws.2021.108433.

(ii) Li, S., Jiang, K., Zhao, O. Press-braked ferritic stainless steel slender channel section beam-columns: Tests, simulations and design. *Thin-Walled Structures*, 183, 110302 (2023). DOI: 10.1016/j.tws.2023.110302.

(iii) Zhang, L., Li, S., Tan, K. H., and Zhao, O. Experimental and numerical investigations of press-braked stainless steel channel section beam-columns. *Thin-Walled Structures*, 161, 107344 (2021). DOI: 10.1016/j.tws.2021.107344.

(iv) Li, S., and Zhao, O. Structural behaviour of press-braked austenitic stainless steel slender channel section beam-columns. *Engineering Structures*, 281, 115818 (2023). DOI: 10.1016/j.engstruct.2023.115818.

The contributions of the co-authors are as follows:

- Asst Prof Zhao provided the initial project direction and financial support.
- I co-designed the tests with Asst Prof Zhao and conducted all the laboratory work at the School of Civil and Environmental Engineering. I also analysed the data with Dr Jiang.
- I performed the numerical modelling and design analyses.
- I prepared the original manuscript draft, which was revised by Dr Zhang, Prof Tan and Asst Prof Zhao.

05/12/2022 LI SHUAI

. . . . . .

Date

. . . . . .

Li Shuai

ACKNOWLEDGEMENTS

The work presented in this thesis was conducted under the supervision of Dr Ou Zhao, Assistant Professor in the School of Civil and Environmental Engineering at Nanyang Technological University. I would wish to give my deepest gratitude to him for his professional guidance, invaluable advice and continuous encouragement throughout my whole PhD journey.

I highly appreciate the generous help and warm company of HPSACSRG research group, including Dr An He, Dr Fangying Wang, Dr Lulu Zhang, Dr Yao Sun, Dr Andi Su, Dr Yukai Zhong, Dr Youxin Ma, Dr Xiaoyi Lan, Dr Ke Jiang, Mr Yannan Jing, Mr Ziyi Wang, Mr Qianzhi Chen, Mr Yuxiao Shi, Mr Yonghui Xing, Ms Lingling Fan and Mr Jin Li.

The assistance of the technicians in the Construction Technology Laboratory and Protective Engineering Laboratory at Nanyang Technological University, where the laboratory experimental programmes reported in this thesis were performed, is greatly acknowledged. Special thanks are also given to Stainless Structurals Asia for sponsoring hot-rolled stainless steel channel section specimens.

Finally, I would like to express my deepest gratitude to my family for their unwavering support and encouragement throughout my doctoral journey. I am profoundly indebted to my beloved wife, Yiting Qiao, and my daughter, Xiangyi Li, whose constant presence and unconditional support have been invaluable to me. I am truly fortunate to have such an incredible family, and I will cherish their love and support for eternity.

TABLE OF CONTENTS

ACKNOWLEDGEMENTS ..... **i**
TABLE OF CONTENTS ..... **iii**
ABSTRACT ..... **vii**
LIST OF PUBLICATIONS ..... **ix**
LIST OF TABLES ..... **xi**
LIST OF FIGURES ..... **xiii**
LIST OF SYMBOLS ..... **xvii**

CHAPTER 1 – INTRODUCTION **1**
1.1 Background 1
1.2 Structural applications 3
1.3 Research objectives 5
1.4 Thesis outline 6

CHAPTER 2 – LITERATURE REVIEW **9**
2.1 Introduction 9
2.2 International design standards 9
2.3 Previous research on stainless steel channel sections 10
2.3.1 Material properties of stainless steel 10
2.3.2 Membrane residual stresses 13
2.3.3 Cross-section behaviour 14
2.3.4 Member behaviour 21
2.4 Concluding remarks 26

CHAPTER 3 – LOCAL BUCKLING OF CHANNEL SECTIONS UNDER PURE COMPRESSION **27**
3.1 Introduction 27
3.2 Testing 28
3.2.1 General 28

3.2.2 Material testing 29
3.2.3 Initial local geometric imperfection measurements 30
3.2.4 Membrane residual stress measurements 33
3.2.5 Stub column tests 39
3.3 Numerical modelling 43
3.3.1 General 43
3.3.2 Development and validation of FE models 43
3.3.3 Parametric studies 45
3.4 Assessment of existing international design standards 46
3.4.1 General 46
3.4.2 EN 1993-1-4 47
3.4.3 ANSI/AISC 370-21 51
3.5 Continuous strength method 52
3.6 Concluding remarks 57

CHAPTER 4 – LOCAL BUCKLING OF CHANNEL SECTIONS UNDER MAJOR-AXIS COMBINED LOADING 59
4.1 Introduction 59
4.2 Testing 60
4.2.1 General 60
4.2.2 Eccentric compression tests 60
4.3 Numerical modelling 66
4.3.1 General 66
4.3.2 Development and validation of FE models 66
4.3.3 Parametric studies 67
4.4 Assessment of existing international design standards 68
4.4.1 General 68
4.4.2 EN 1993-1-4 69
4.4.3 ANSI/AISC 370-21 71
4.5 Development of new design method 72
4.6 Concluding remarks 76

CHAPTER 5 – LOCAL BUCKLING OF CHANNEL SECTIONS UNDER MINOR-AXIS COMBINED LOADING 79
5.1 Introduction 79
5.2 Testing 80
5.2.1 General 80
5.2.2 Eccentric compression tests 81
5.3 Numerical modelling 86
5.3.1 General 86
5.3.2 Development and validation of FE models 86
5.3.3 Parametric studies 88
5.4 Assessment of existing international design standards 88
5.4.1 General 88
5.4.2 EN 1993-1-4 89
5.4.3 ANSI/AISC 370-21 92
5.5 Development of new design method 94
5.6 Concluding remarks 96

CHAPTER 6 – FLEXURAL BUCKLING OF CHANNEL SECTION COLUMNS 101
6.1 Introduction 101
6.2 Testing 102
6.2.1 General 102
6.2.2 Initial global and local geometric imperfection measurements 103
6.2.3 Pin-ended column tests 105
6.3 Numerical modelling 111
6.3.1 General 111
6.3.2 Development and validation of FE models 111
6.3.3 Parametric studies 115
6.4 Assessment of existing international design standards 116
6.4.1 General 116
6.4.2 EN 1993-1-4 117
6.4.3 ANSI/AISC 370-21 119

6.5 Development of new design method 121
6.6 Conclusions 123

CHAPTER 7 – GLOBAL BUCKLING OF CHANNEL SECTION BEAM-COLUMNS 125
7.1 Introduction 125
7.2 Testing 126
7.2.1 General 126
7.2.2 Beam-column (eccentric compression) tests 127
7.3 Numerical modelling 130
7.3.1 General 130
7.3.2 Development and validation of FE models 133
7.3.3 Parametric studies 134
7.4 Assessment of existing international design standards 135
7.4.1 General 135
7.4.2 EN 1993-1-4 138
7.4.3 ANSI/AISC 370-21 141
7.5 Development of new design method 143
7.6 Conclusions 148

CHAPTER 8 – CONCLUSIONS AND SUGGESTIONS FOR FUTURE RESEARCH 151
8.1 Conclusions 151
8.2 Suggestions for future work 154

REFERENCES 157

ABSTRACT

Stainless steel offers numerous advantages over carbon steel, including superior corrosion resistance, high material strength and exceptional ductility. Therefore, the use of stainless steel members in civil and offshore engineering becomes increasingly prevalent. Channel sections with simple geometry are widely used in structural applications. This thesis is focusing on the structural behaviour and design of hot-rolled stainless steel channel section members subjected to various loading conditions. An experimental programme adopted grade EN 1.4301 austenitic stainless steel and four hot-rolled stainless steel plain channel sections: C 80×40×5, C 100×50×5, C 100×50×6 and C 150×75×6. Material testing was performed to measure the material stress–strain responses and membrane residual stress measurements were carried out to determine the membrane residual stress distributions and amplitudes in the studied hot-rolled stainless steel channel sections. At cross-sectional level, six stub column tests and twenty eccentrically loaded stub column tests about the major and minor principal axes were performed to investigate the local buckling behaviour of channel sections under isolated and combined loadings, respectively. At member level, ten column tests and ten beam-column tests were conducted to study the flexural buckling behaviour of channel section columns and global buckling behaviour of channel section beam-columns, respectively. The experimental programme was supplemented by a numerical modelling programme, where finite element models were initially developed and validated against the test results and then adopted to perform parametric studies to generate further numerical data over a wide range of cross-section dimensions, member effective lengths and loading combinations. The obtained experimental and numerical data were then employed to assess the accuracy of the existing design rules for hot-rolled stainless steel channel section members, as given in the European code and American specification. The assessment results revealed that the current design codes result in conservative cross-section resistance predictions, but scattered member resistance predictions with both conservative and unsafe results, mainly owing to the lack of proper consideration of the pronounced material strain hardening and nonlinear material property of stainless steel in the design. To overcome these shortcomings, new design approaches were proposed and

shown to lead to a much higher level of design accuracy and consistency over the existing design standards. The reliability of the proposed design methods was demonstrated by means of statistical analyses, showing their suitability for incorporation into future revisions of international design codes for stainless steel structures.

LIST OF PUBLICATIONS

1. **Li, S.**, Zhang, L., Liang, Y., and Zhao, O. (2021). Experimental and numerical investigations of hot-rolled stainless steel channel section columns susceptible to flexural buckling. *Thin-Walled Structures*, 164, 107791.

2. **Li, S.**, Zhang, L., and Zhao, O. (2022). Global buckling and design of hot-rolled stainless steel channel section beam–columns. *Thin-Walled Structures*, 170, 108433.

3. **Li, S.**, Zhang, L., and Zhao, O. (2022). Testing, modelling and design of hot-rolled stainless steel channel sections under combined compression and minor-axis bending moment. *Thin-Walled Structures*, 172, 108836.

4. **Li, S.**, Zhang, L., and Zhao, O. (2022). Cross-section behavior and design of hot-rolled stainless steel channel sections under major-axis combined loading. *Journal of Structural Engineering (ASCE)*, 148, 04022110.

5. **Li, S.**, and Zhao, O. (2022). Local buckling and capacity of press-braked ferritic stainless steel channel sections under minor-axis combined loading. *Thin-Walled Structures*, 178, 109507.

6. **Li, S.**, and Zhao, O. (2022). Local–flexural interactive buckling behaviour and resistance of press-braked stainless steel slender channel section columns. *Engineering Structures*, 270, 114871.

7. **Li, S.**, Su, A., Zhao, O. (2022). Post-fire behaviour and residual resistance of hot-rolled stainless steel channel sections under major-axis combined loading. *Engineering Structures*, 115202.

8. **Li, S.**, Jiang, K., Zhao, O. (2023). Press-braked ferritic stainless steel slender channel section beam-columns: Tests, simulations and design. *Thin-Walled Structures*, 183, 110302.

9. **Li, S.,** and Zhao, O. (2023). Testing, simulation and design of press-braked ferritic stainless steel slender channel section columns failing by local–flexural interactive buckling. *Thin-Walled Structures*, 185, 110621.

10. **Li, S.**, and Zhao, O. (2023). Structural behaviour of press-braked austenitic stainless steel slender channel section beam-columns. *Engineering Structures*, 02688.

11. **Li, S.**, Su, A. and Zhao, O. (2023). Cross-section behaviour of press-braked ferritic stainless steel channel sections under combined compression and major-axis bending moment. *Thin-Walled Structures*, 185, 115818.

12. **Li, S.**, and Zhao, O. (2023). Flexural buckling behaviour and residual resistances of hot-rolled stainless steel channel section columns after exposure to elevated temperatures. *Engineering Structures*, accepted.

13. Zhang, L., **Li, S.**, Tan, K. H., and Zhao, O. (2021). Experimental and numerical investigations of press-braked stainless steel channel section beam-columns. *Thin-Walled Structures*, 161, 107344.

14. Lan, X., **Li, S.**, and Zhao, O. (2021). Local buckling of hot-rolled stainless steel channel section stub columns after exposure to fire. *Journal of Constructional Steel Research*, 187, 106950.

LIST OF TABLES

Table 2.1. Summary of previous tests on steel channel sections 19
Table 2.2. Summary of previous tests on steel channel section members 24
Table 3.1. Measured geometric dimensions and initial local geometric imperfections of hot-rolled stainless steel channel section stub column specimens. 28
Table 3.2. Summary of key measured material properties from tensile coupon tests. 31
Table 3.3. Measured peak membrane residual stresses in hot-rolled stainless steel channel sections. 37
Table 3.4. Summary of key stub column test results 41
Table 3.5. Comparisons of numerical failure loads with test failure loads for varying initial local geometric imperfection magnitudes..... 46
Table 3.6. Comparisons of test and numerical failure loads with predicted failure loads from different design methods..... 47
Table 3.7. Reliability analysis results calculated according to EN 1990. 55
Table 4.1. Geometric dimensions and initial local geometric imperfections of hot-rolled stainless steel channel section stub column specimens. 62
Table 4.2. Summary of major-axis eccentric compression test results 63
Table 4.3. Comparisons of numerical failure loads with test failure loads for varying initial local geometric imperfection magnitudes..... 67
Table 4.4. Comparisons of test and numerical failure loads with predicted failure loads from different design methods..... 68
Table 4.5. Reliability analysis results calculated according to EN 1990. 74
Table 5.1. Measured geometric dimensions and initial local geometric imperfections of hot-rolled stainless steel channel section stub column specimens. 80
Table 5.2. Summary of minor-axis eccentric compression test results. 83
Table 5.3. Comparisons of FE failure loads with test failure loads for different initial local geometric imperfection magnitudes. 87
Table 5.4. Comparisons of test and numerical failure loads with predicted failure loads from different design methods..... 89

Table 5.5. Reliability analysis results calculated according to EN 1990. 96
Table 6.1. Measured geometric dimensions and initial global and local geometric imperfections of hot-rolled stainless steel channel section column specimens. 102
Table 6.2. Summary of pin-ended column test results..... 108
Table 6.3. Comparisons of FE failure loads with test failure loads for varying initial global and local geometric imperfection magnitude combinations. 114
Table 6.4. Comparisons of test and FE failure loads with predicted flexural buckling resistances. 116
Table 6.5. Reliability analysis results determined according to EN 1990. 123
Table 7.1. Measured geometric dimensions and initial global and local geometric imperfections of hot-rolled stainless steel channel section beam-column specimens. 127
Table 7.2. Summary of beam-column test results..... 130
Table 7.3. Comparisons of FE failure loads with test failure loads for varying initial global and local geometric imperfection magnitude combinations. 134
Table 7.4. Comparisons of test and FE failure loads with predicted failure loads. 137
Table 7.5. Proposed coefficients for k_n. 145
Table 7.6. Reliability analysis results calculated according to EN 1990. 148

LIST OF FIGURES

Figure. 1.1. Corrosion in steel constructions 2
Figure. 1.2. Helix Pedestrian Bridge, Singapore 4
Figure. 1.3. Gateway Arch, St. Louis, Missouri 5
Figure. 1.4. Louvre Pyramid, Paris, France 5
Figure. 1.5. Press-braked, hot-rolled and laser-welded stainless steel channel sections (from left to right). 6
Figure. 2.1. Comparisons of typical stress–strain curves of stainless steel and conventional carbon steel..... 11
Figure 3.1. Notations of geometric parameters of hot-rolled stainless steel channel sections and locations of coupons. 29
Figure 3.2. Material tests. 31
Figure 3.3. Measured material stress–strain curves. 32
Figure 3.4. Test setup for initial local geometric imperfection measurements..... 33
Figure 3.5. Locations of strips cut for membrane residual stress measurements (in mm). 34
Figure 3.6. Locations and dimensions of strips within channel sections (in mm)... 34
Figure 3.7. Typical sectioned C 150×75×6 specimen..... 35
Figure 3.8. Measured membrane residual stress patterns and amplitudes (in MPa).37
Figure 3.9. Comparisons between measured membrane residual stress patterns and amplitudes and predictive model. 38
Figure 3.10. Membrane residual stress predictive model for hot-rolled stainless steel channel sections. 39
Figure 3.11. Stub column test setup. 40
Figure 3.12. Load–end shortening curves of hot-rolled stainless steel channel section stub column specimens. 41
Figure 3.13. Test and FE failure modes for typical stub column specimens. 42
Figure 3.14. Modelled membrane residual stress pattern and amplitudes (in MPa) for stub column specimen C2-S1..... 44

Figure 3.15. Evaluation of codified slenderness limit for outstand flanges in compression. 49
Figure 3.16. Evaluation of codified slenderness limit for internal web in compression. 49
Figure 3.17. Comparisons of test and numerical failure loads with failure load predictions from EN 1993-1-4 51
Figure 3.18. Comparisons of test and numerical failure loads with failure load predictions from ANSI/AISC 370-21 53
Figure 3.19. CSM bi-linear material model. 54
Figure 3.20. Comparisons of test and numerical failure loads with failure load predictions from CSM..... 56
Figure 3.21. Test and FE failure loads compared with failure load predictions from EN 1993-1-4 and CSM. 56
Figure 3.22. Test and FE failure loads compared with failure load predictions from ANSI/AISC 370-21 and CSM. 57
Figure 4.1. Measured distribution of initial local geometric imperfections for stub column specimen B2. 62
Figure 4.2. Major-axis eccentric compression test setup. 63
Figure 4.3. Load–mid-height lateral deflection curves for stub column specimens. 64
Figure 4.4. Test and FE failure modes for stub column specimen A5..... 65
Figure 4.5. Test and FE failure modes for stub column specimen B2..... 65
Figure 4.6. Test and FE data compared with EC3 design interaction curve..... 70
Figure 4.7. Test and FE data compared with AISC design interaction curve..... 72
Figure 4.8. Test and FE data compared with proposed design interaction curves... 75
Figure 4.9. Test and FE failure loads compared with predictions from EC3 and proposed design interaction curves. 75
Figure 4.10. Test and FE failure loads compared with predictions from AISC and proposed design interaction curves. 76
Figure 5.1. Setup for minor-axis eccentric compression tests 82
Figure 5.2. Experimental and numerical failure modes for specimen C5 failing in the ‘C’ orientation. 84

Figure 5.3. Experimental and numerical failure modes for specimen RC4 failing in the ‘reverse C’ orientation. 84
Figure 5.4. Experimental and numerical load–mid-height lateral deflection curves. 85
Figure 5.5. Comparisons of test and FE data against EC3 design interaction curve. 91
Figure 5.6. Comparisons of test and FE data against AISC design interaction curve. 93
Figure 5.7. Comparisons of test and FE data against new design interaction curve.97
Figure 5.8. Test and FE failure loads compared with failure load predictions from EN 1993-1-4 and new proposal. 98
Figure 5.9. Test and FE failure loads compared with failure load predictions from ANSI/AISC 370-21 and new proposal. 99
Figure 6.1. Test setup for initial global geometric imperfection measurements. .. 104
Figure 6.2. Sign convention of initial global geometric imperfection ω_g. 104
Figure 6.3. Test setup for initial local geometric imperfection measurements. 104
Figure 6.4. Pin-ended column test setup. 106
Figure 6.5. Sign convention for actual overall global geometric imperfection e_m. 107
Figure 6.6. Test failure modes for hot-rolled stainless steel channel section column specimens. 109
Figure 6.7. Test and FE load–mid-height lateral deflection curves for column specimens. 110
Figure 6.8. Modelled membrane residual stress pattern and amplitudes (in MPa) for specimen C2-L1. 112
Figure 6.9. Test and FE failure modes for specimen C1-L3 (with minor-axis flexural buckling in the ‘C’ orientation). 114
Figure 6.10. Test and FE failure modes for specimen C2-L4 (with minor-axis flexural buckling in the ‘reverse C’ orientation). 115
Figure 6.11. Comparisons of test and FE failure loads with codified and proposed design buckling curves. 118
Figure 6.12. Comparisons of test and FE failure loads with EC3 flexural buckling resistance predictions. 119

Figure 6.13. Comparisons of test and FE failure loads with AISC flexural buckling resistance predictions. 121
Figure 6.14. Comparisons of test and FE failure loads with flexural buckling resistance predictions from new design approach. 122
Figure 7.1. Beam-column test setup. 128
Figure 7.2. Test and FE failure modes for specimen A3 (with minor-axis global buckling in the 'reverse C' orientation). 131
Figure 7.3. Test and FE failure modes for specimen B3 (with minor-axis global buckling in the 'C' orientation)..... 131
Figure 7.4. Test and FE load–mid-height lateral deflection curves. 132
Figure 7.5. Definition of θ. 138
Figure 7.6. Comparisons of hot-rolled stainless steel channel section beam-column test and FE failure loads with predicted failure loads from EN 1993-1-4. 140
Figure 7.7. Comparisons of hot-rolled stainless steel channel section beam-column test and FE failure loads with predicted failure loads from ANSI/AISC 370-21. . 142
Figure 7.8. Typical numerically calculated k_n corresponding to n_b=0.3. 145
Figure 7.9. The upper set of the numerically calculated k_n. 146
Figure 7.10. Comparisons between proposed (solid) and numerically calculated (dotted) curves for k_n. 146
Figure 7.11. Comparisons of hot-rolled stainless steel channel section beam-column test and FE failure loads with predicted failure loads from new proposal..... 147

LIST OF SYMBOLS

A	Gross cross-section area
A_{eff}	Effective cross-section area
a_w	Ratio of web area to gross cross-section area
B_f	Outer flange width of channel section
B_w	Outer web width of channel section
b	Mean ratio of test and numerical to design model resistances
C_1, C_2, C_3, C_4	CSM material parameters
c	Flat element width
c_{eff}	Effective plate element width
c_f	Flat element length of flange of channel section
c_w	Flat element length of web of channel section
D_1, D_2, D_3	Parameters of new design interaction curve
E	Young's modulus
E_{sh}	Strain hardening slope
$E_{0.2}$	Tangent modulus at 0.2% material proof stress
e_m	Actual overall global geometric imperfection amplitude
e_0	Initial loading eccentricity
e_{0e}	Initial loading eccentricity to cross-section elastic neutral axis
e_{0p}	Initial loading eccentricity to cross-section plastic neutral axis
F_{cr}	AISC design flexural buckling stress
F_e	Euler buckling stress
f_y	Material yield stress
I_y	Second moment of area about major axis
I_z	Second moment of area about minor axis
$k_{d,n}$	Design (ultimate limit state) fractile factor
k_n	Proposed new interaction factor
k_z	EC3 interaction factor
k_σ	Plate buckling factor
L	Specimen length
L_e	Effective member length

L_0	Nominal length between gauge holes
$M_{csm,y,Rd}$	CSM cross-section bending moment resistance about major axis
$M_{csm,z,Rd}$	CSM cross-section bending moment resistance about minor axis
M_{cy}	AISC cross-section bending moment resistance about major axis
M_{cz}	AISC cross-section bending moment resistance about minor axis
$M_{EC3,y,Rd}$	EC3 cross-section bending moment resistance about major axis
$M_{EC3,z,Rd}$	EC3 cross-section bending moment resistance about minor axis
M_{eff}	Cross-section effective moment capacity
$M_{eff,y}$	Cross-section effective moment capacity about major axis
M_{el}	Cross-section elastic moment capacity
$M_{el,y}$	Cross-section elastic moment capacity about major axis
$M_{el,z}$	Cross-section elastic moment capacity about minor axis
M_{pl}	Cross-section plastic moment capacity
$M_{pl,y}$	Cross-section plastic moment capacity about major axis
$M_{pl,z}$	Cross-section plastic moment capacity about minor axis
M_R	Codified bending moment resistance
M_u	Failure moment
$M_{u,pred}$	Predicted failure moment
$M_{u,test}$	Test failure moment
$M_{uy,AISC}$	Predicted bending moment about major axis by ANSI/AISC 370-21
$M_{uy,EC3}$	Predicted bending moment about major axis by EN 1993-1-4
$M_{uy,p}$	Predicted major-axis bending moment by proposed design method
$M_{uz,AISC}$	Predicted bending moment about minor axis by ANSI/AISC 370-21
$M_{uz,EC3}$	Predicted bending moment about minor axis by EN 1993-1-4
$M_{uz,p}$	Predicted minor-axis bending moment by proposed design method
$M_{u,1st,el}$	First-order elastic bending moment at the failure load
$M_{u,2nd,el}$	Second-order elastic bending moment at the failure load
$M_{u,2nd,inel}$	Second-order inelastic bending moment at the failure load
m	Strain hardening exponent based on $\sigma_{0.2}$ and σ_u
N	Applied compression load
$N_{b,z,Rd}$	Column minor-axis flexural buckling resistance by EN 1993-1-4
$N_{br,z,Rd}$	Column minor-axis flexural buckling resistance by new EN 1993-1-4

N_c	AISC design cross-section compression resistance
N_{cr}	Euler buckling load about minor axis
$N_{csm,Rd}$	CSM design cross-section compression resistance
$N_{EC3,Rd}$	EC3 design cross-section compression resistance
N_{eff}	Cross-section effective compression capacity
N_{pl}	Cross-section yield load
N_R	Codified column buckling resistance
N_u	Failure load
$N_{u,AISC}$	Predicted failure load by ANSI/AISC 370-21
$N_{u,csm}$	Predicted failure load by CSM
$N_{u,EC3}$	Predicted failure load by EN 1993-1-4
$N_{u,FE}$	FE failure load
$N_{u,p}$	Predicted failure load by proposed design method
$N_{u,pred}$	Predicted failure load
$N_{u,test}$	Test failure load
n	Strain hardening exponent
n_b	Compression load level
$n'_{0.2,1.0}$	Strain hardening exponent based on $\sigma_{0.2}$ and $\sigma_{1.0}$
r	Corner inner radius
r_1	Reading of Demec gauge taken before sectioning
r_2	Reading of Demec gauge taken after sectioning
t	Cross-section thickness
t_1	Length of temperature reference bar before sectioning
t_2	Length of temperature reference bar after sectioning
V_r	Combined COV incorporating all the variable uncertainties
V_δ	COV of the tests and numerical simulations to the resistance model
$W_{eff,y}$	Effective section modulus about major axis
$W_{el,y}$	Elastic section modulus about major axis
$W_{el,z}$	Elastic section modulus about minor axis
$W_{pl,y}$	Plastic section modulus about major axis
$W_{pl,z}$	Plastic section modulus about minor axis
y_c	Distance from outmost compressive fibre to CSM design neutral axis

α_A	AISC amplification factor
α_{csm}	CSM bending parameter
α_{EC3}	Imperfection factor used in EN 1993-1-4
$\alpha, \beta_0, \beta_1, \beta_2$	AISC flexural buckling coefficients
γ_{M0}	Partial safety factor for cross-section resistance
γ_{M1}	Partial safety factor for member resistance
Δ	Lateral deflection at the mid-height of specimen
Δ_u	Mid-height lateral deflection at failure load
ε	Strain and EN 1993-1-4 material parameter
ε_c	Corrected strain
ε_{csm}	CSM predicted limiting compressive strain of cross-section
$\varepsilon_{csm,d}$	CSM design strain for the determination of bending resistance
$\varepsilon_{csm,t}$	CSM predicted limiting tensile strain of cross-section
ε_f	Strain at fracture
ε_{max}	Strain gauge values of the maximum compressive fibre
ε_{min}	Strain gauge values of the minimum compressive fibre
ε_{nom}	Engineering strain
ε_{ln}^{pl}	True plastic strain
ε_u	Strain at the ultimate stress
ε_y	Material yield strain
$\varepsilon_{0.2}$	Strain at 0.2% proof stress
$\varepsilon_{1.0}$	Strain at 1.0% proof stress
θ	Angle parameter
$\overline{\lambda}_l$	Plate element slenderness
$\overline{\lambda}_p$	Cross-section slenderness
$\overline{\lambda}_z$	Column non-dimensional slenderness about minor axis
$\overline{\lambda}_0$	Limiting slenderness
σ	Stress
σ_{cr}	Elastic critical local buckling stress of cross-section
σ_{csm}	CSM design stress
σ_{fc}	Peak compressive residual stress in flange of channel section

σ_{ft}	Peak tensile residual stress in flange of channel section
σ_{true}	True stress
σ_{nom}	Engineering stress
σ_u	Ultimate stress
σ_{wc}	Peak compressive residual stress in web of channel section
σ_{wt}	Peak tensile residual stress in web of channel section
$\sigma_{0.01}$	0.01% proof stress
$\sigma_{0.2}$	0.2% proof stress
$\sigma_{1.0}$	1.0% proof stress
δ	Maximum deviation of curved strip
δ_u	Axial shortening of specimen at failure load
ϕ	Buckling coefficient used in EN 1993-1-4.
χ	Reduction factor for column buckling resistance
ω_{f1}, ω_{f2}	Initial local geometric imperfection magnitudes of two flanges
ω_g	Initial mid-height global geometric imperfection amplitude
ω_w	Initial local geometric imperfection magnitude of web
ω_0	Initial local geometric imperfection magnitude of channel section

CHAPTER 1

INTRODUCTION

1.1 Background

Steel is becoming a preferred construction material in civil engineering and offers numerous advantages over concrete, including high material strength, light self-weight, greater erection speed, etc. However, conventional carbon steel suffers from corrosion, which can reduce cross-section thicknesses and increases initial geometric imperfections, with two typical examples shown in Figure. 1.1. In accordance with the current concern on sustainable construction, the full life-cycle performance of structures has been gaining attention from architectural and structural designers, and thus construction materials with superior sustainability are being increasingly adopted. This promotes the development of stainless steel, which specifies corrosion and heat resistant steel with a minimum of 10.5% chromium.

The corrosion resistance of stainless steel is attributed to a transparent and tightly adherent lay of chromium-rich oxide, which is stable, non-porous and self-repaired. Stainless steel is marked as a sustainable material and 100% recyclable after use with no degradation of mechanical and physical properties, leading to low maintenance and inspection costs during its service life. Moreover, stainless steel also possesses favourable mechanical properties, including high material strength and excellent ductility, in comparison with conventional carbon steel (Gardner 2005, 2019; Baddoo

2008; Gedge 2008). On the basis of the metallurgical structure, stainless steel is classified into five basic groups, including austenitic, ferritic, duplex, martensitic and precipitation hardening, of which the first three are applied to structural applications (Gardner 2005).

(a) Steel columns
(http://zh-cht.gofreedownload.net/free-photos/red/steel-beams-iron-construction-construction-183555/#.YvNjzuhByUm)

(b) Steel connections
(https://addcrazy.com/the-types-of-corrosion-in-steel-and-how-to-prevent-them/)

Figure. 1.1. Corrosion in steel constructions

Owing to the favourable mechanical properties offered by stainless steel, the annual consumption of stainless steel has increased at a compound growth rate of 5% over the past two decades, which is far more than the growth rate of other materials. Especially in civil and offshore engineering, the growth rate of stainless steel used as

a construction material has been even faster all over the world. For example, it is estimated that in 2006, 14% of the total quantity of stainless steel, which was about four million tons, were applied to construction applications worldwide (Baddoo 2008).

However, current stainless steel structures suffer from (i) the high initial material cost and (ii) the lack of efficient design codes. To overcome these shortcomings, substantial effort has been devoted to developing new fabrication methods and more efficient design rules. Recently, with the advancement in manufacturing and metallurgical techniques, direct hot-rolling of stainless steel channel sections becomes possible (https://www.montanstahl.com). In comparison with traditional welding and cold-forming, new hot-rolling reduces fabrication costs, on average, and therefore has a rather good potential in fabricating stainless steel cross-sections. Moreover, current design rules for stainless steel structures lead to inaccurate resistance predictions for stainless steel structural members and thus substantial material waste. For example, the European code EN 1993-1-4 (CEN 2015) for stainless steel sections were developed by directly mirroring those for normal strength carbon steel sections (CEN 2014), with no consideration of the pronounced material strain hardening and nonlinear material property of stainless steel. Therefore, extensive experimental and numerical studies on different types of stainless steel structural members under various loading conditions have been conducted, in order to examine their buckling behaviour and resistances, assess the accuracy of the existing design codes and develop more accurate and consistent design approaches.

1.2 Structural applications

Stainless steel has been traditionally only used for minor building components until the 1980s, including roofs, facades, floor plates and so on. Recently, advanced fabrication and production of stainless steel have matured, making it possible to provide stainless steel structural members with large cross-section sizes. Therefore, stainless steel has been increasingly used as load-bearing structural components in bridges, high-rise structures and buildings, with three typical examples presented in

Figures 1.2–1.4, respectively. More stainless steel structural applications have been reported in Baddoo et al. (1997), Gardner (2008a), Gedge (2008) and Baddoo (2008, 2013).

Figure. 1.2. Helix Pedestrian Bridge, Singapore
(https://www.singaporetravelhub.com/attractions/helix-bridge/)

Figure. 1.3. Gateway Arch, St. Louis, Missouri
(https://www.roywant.com/gallery/sampler%202005/large/31.jpg)

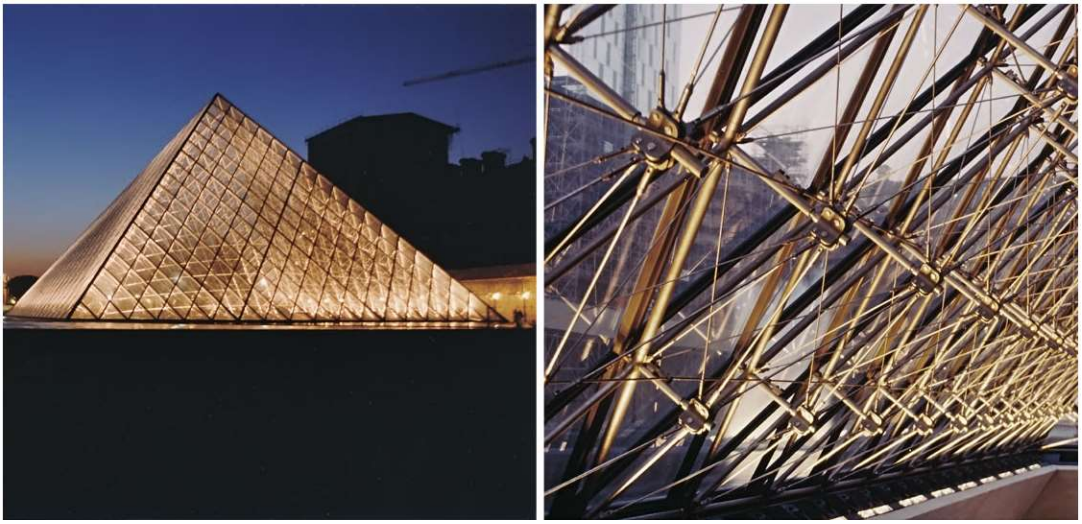

Figure. 1.4. Louvre Pyramid, Paris, France
(http://preview.tripyramid.com/project/louvre-pyramid-tension-rod-support-system/)

Channel sections with ease fabrication are widely used in structural applications. For example, channel sections are used as rafters spanning from eaves to ridges in lightweight frames, as bracing members in low-rise and medium-rise buildings to resist lateral forces and as frameworks to position wooden boards in wood-steel composite structures. Three fabrication methods have been used for stainless steel channel sections, including press-braking, hot-rolling and welding, and Figure. 1.5 presents channel sections fabricated by three different methods. It should be noted that hot-rolling not only leads to lower fabrication cost, but provides channel sections with a much lower level of membrane residual stresses than welding and with more homogeneous material properties and more consistent hardness than press-braking. The present study thus focuses on the structural behaviour and design of hot-rolled stainless steel channel section members.

1.3 Research objectives

Considering that stainless steel suffers from high material cost than conventional carbon steel, the material should be used to the utmost in structural applications. However, most of the design rules and formulae given in the current international codes for hot-rolled stainless steel channel section members were developed by

simply mirroring those for their conventional carbon steel counterparts, leading to a significantly low level of design efficiency. Therefore, studies on hot-rolled stainless steel channel sections and development of efficient design methods are the objectives of the present thesis.

Figure. 1.5. Press-braked, hot-rolled and laser-welded stainless steel channel sections (from left to right).
(https://www.montanstahl.com/blog/production-methods-press-brake-hot-roll-laser-weld/)

1.4 Thesis outline

There are eight chapters in this thesis, with a brief summary of the corresponding contents provided below.

Chapter 1 provides a brief introduction to the background of stainless steel and its structural applications in civil engineering. The research objectives and outline of this thesis are also reported.

Chapter 2 presents a broad review of the current international design standards and previous key experimental and numerical studies relevant to the present research, with the research gaps highlighted.

Chapter 3 describes experimental and numerical studies on the material responses, membrane residual stresses and local buckling behaviour of hot-rolled stainless steel

channel sections under pure compression. The obtained experimental and numerical data are used to assess the accuracy of the relevant codified design rules and continuous strength method.

Chapter 4 and Chapter 5 study the local buckling behaviour and cross-section resistances of hot-rolled stainless steel channel sections under combined compression and bending moment. Eccentrically loaded stub column tests about the minor and major principal axes are firstly performed and numerical modelling is then conducted to expand the test data pool. Based on the test and numerical data, the accuracy of the codified design interaction curves is assessed, followed by the development of new improved design interaction curves.

Chapter 6 reports a testing and numerical modelling programme on the flexural buckling behaviour and resistances of hot-rolled stainless steel channel section columns. The experimentally and numerically generated results are adopted to evaluate the accuracy of the codified buckling curves and a new buckling curve is then proposed.

Chapter 7 focuses on the global buckling behaviour of hot-rolled stainless steel channel section beam-columns under combined compression and minor-axis bending moment. Experimental and numerical studies are firstly conducted and the evaluation of the codified design interaction curves is then performed, with their shortcomings highlighted. Finally, an improved design interaction curve is developed.

Chapter 8 concludes the key findings of this research and provides suggestions for future research work.

CHAPTER 2

LITERATURE REVIEW

2.1 Introduction

This chapter reports an extensive review of previous research work relevant to the present thesis. A brief review of current international design standards for stainless steel structures, including the European code and American specification, is firstly provided. Previous relevant investigations into the behaviour of steel channel section members are then summarised and presented, including material properties, membrane residual stresses, cross-section behaviour and member behaviour. Finally, research gap is highlighted and thus the subject of this study.

2.2 International design standards

The earliest European guidance for stainless steel, referring to 'Design Manual for Structural Stainless Steel', was issued by Euro Inox in 1994. On the basis of this guidance, the European Standards Committee (CEN) published a European pre-standard for stainless steel in 1996, which was known as 'ENV 1993-1-4: Design of Steel Structures – Part 1-4: General Rules – Supplementary Rules for Stainless Steels', and then released a formal European code – EN 1993-1-4 in 2006. The existing

European code for stainless steel structures EN 1993-1-4 (CEN 2015) was supplemented by one amendment based on EN 1993-1-4 in 2015 (CEN 2006a).

American Iron and Steel Institute (AISI) published the world's first design standard for structural stainless steel – 'Specification for the Design of Light Gauge Cold-Formed Stainless Steel Structure Members' (AISI 1962). The existing American specifications for structural stainless steel are 'Specification for the Design of Cold-formed Stainless Steel Structural Members' issued by the American Society of Civil Engineers (ASCE) in 2002 and 'Specification for Structural Stainless Steel Buildings' released by the American Institute of Steel Construction (AISC) in 2021.

Though several design standards have been developed for stainless steel structures, only the European code 1993-1-4 (CEN 2015) and American specification ANSI/AISC 370-21 (AISC 2021) specify design provisions for hot-rolled stainless steel channel section members, with their accuracy assessed in this thesis.

2.3 Previous research on stainless steel channel sections

2.3.1 Material properties of stainless steel

Figure. 2.1 presents the comparisons of the typical stress–strain curves of stainless steel and conventional carbon steel. Specifically, stainless steel exhibits a nonlinear stress–strain response with no obvious yield point but a high level of strain hardening and ductility, while conventional carbon steel displays a linear elastic stress–strain response at the initial stage until the attainment of a clearly defined yield point, which is followed by a yield plateau and then some strain hardening. Note that the material yield stress of stainless steel is equal to the proof stress at the 0.2% offset strain $\sigma_{0.2}$. It can be found that stainless steel generally presents higher material strength and material ductility. For example, in comparison with the most commonly used S355 carbon steel with ultimate stress of 510 MPa and ultimate strain of 15%–20%,

austenitic stainless steel features a higher ultimate stress of 650–750 MPa and a much higher ultimate strain of 50%–60%.

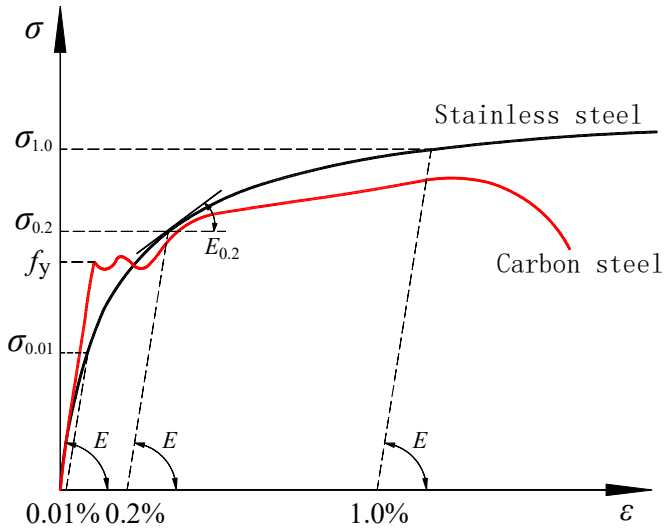

Figure. 2.1. Comparisons of typical stress–strain curves of stainless steel and conventional carbon steel

An idealised bi-linear material model is used to represent the whole stress–strain response of conventional carbon steel, while a Ramberg–Osgood (R–O) material model is employed to capture the nonlinear stress–strain response of stainless steel. The R–O material model was firstly developed by Ramberg and Osgood (1943) and then revised by Hill (1944), as given by Equation (2.1), where ε and σ are the material strain and stress, respectively, E is the Young's modulus, $\sigma_{0.2}$ is the 0.2% proof stress, and n is the strain hardening exponent to reflect the roundness of the stress–strain curve and can be calculated by Equation (2.2), where $\sigma_{0.01}$ is the 0.01% proof stress. Considering that the R–O material model (Ramberg and Osgood 1943; Hill 1944) failed to predict the stress–strain relationship beyond the 0.2% proof stress though it led to accurate predictions of the stress–strain relationship before the 0.2% proof stress, a two-stage R–O material model was proposed by Mirambell and Real (2000), in order to accurately predict the whole range of stress–strain response. In the two-stage R–O material model, Equation (2.1) is used for the first stage up to the 0.2% proof stress, while the second stage beyond the 0.2% proof stress until the ultimate stress is expressed by Equation (2.3), where $E_{0.2}$ is the tangent modulus at the 0.2% proof stress given by Equation (2.4), σ_u is the ultimate stress, $\varepsilon_{0.2}$ is the strain at the

0.2% proof stress, ε_u is the strain at the ultimate stress and m is the strain hardening exponent fitted to the second stage of the stress–strain curve.

$$\varepsilon = \frac{\sigma}{E} + 0.002\left(\frac{\sigma}{\sigma_{0.2}}\right)^n \tag{2.1}$$

$$n = \frac{\ln(20)}{\ln(\sigma_{0.2}/\sigma_{0.01})} \tag{2.2}$$

$$\varepsilon = \frac{\sigma - \sigma_{0.2}}{E_{0.2}} + \left(\varepsilon_u - \varepsilon_{0.2} - \frac{\sigma_u - \sigma_{0.2}}{E_{0.2}}\right)\left(\frac{\sigma - \sigma_{0.2}}{\sigma_u - \sigma_{0.2}}\right)^m + \varepsilon_{0.2} \quad \text{for } \sigma_{0.2} < \sigma \le \sigma_u \tag{2.3}$$

$$E_{0.2} = \frac{E}{1 + 0.002n\frac{E}{\sigma_{0.2}}} \tag{2.4}$$

The two-stage R–O material model (Mirambell and Real 2000) was then simplified by Rasmussen (2003) using basic parameters (E, $\sigma_{0.2}$, n), as given by Equation (2.5), where σ_u, ε_u and m are calculated by Equations (2.6)–(2.8), respectively.

$$\varepsilon = \frac{\sigma - \sigma_{0.2}}{E_{0.2}} + \varepsilon_u\left(\frac{\sigma - \sigma_{0.2}}{\sigma_u - \sigma_{0.2}}\right)^m + \varepsilon_{0.2} \quad \text{for } \sigma_{0.2} < \sigma \le \sigma_u \tag{2.5}$$

$$\frac{\sigma_{0.2}}{\sigma_u} = \begin{cases} 0.2 + 185\frac{\sigma_{0.2}}{E} & \text{for austenitic and duplex stainless steel} \\ \dfrac{0.2 + 185\frac{\sigma_{0.2}}{E}}{1 - 0.0375(n-5)} & \text{for other stainless steel alloys} \end{cases} \tag{2.6}$$

$$\varepsilon_u = 1 - \frac{\sigma_{0.2}}{\sigma_u} \tag{2.7}$$

$$m = 1 + 3.5\frac{\sigma_{0.2}}{\sigma_u} \tag{2.8}$$

In view of the fact that the R–O material model (Rasmussen 2003) cannot be directly used to predict the compressive stress–strain response of stainless steel, Gardner and Nethercot (2004) developed a new formula for the second stage of the R–O material model using the 1.0% proof stress $\sigma_{1.0}$ in place of the ultimate stress σ_u, as expressed by Eq. (2.9), where $\varepsilon_{1.0}$ is the strain at the 1.0% proof stress and $n'_{0.2,1.0}$ is the strain

hardening exponent featuring the degree of nonlinearity of the stress–strain curve beyond the 0.2% proof stress. This two-stage R–O material model (Gardner and Nethercot 2004) was shown to provide good agreement with the experimental (compressive and tensile) stress–strain curves up to strain of approximately 10%, which can be applied to practical numerical modelling and design analysis and is also adopted in this thesis (Gardner 2005). Recently, Quach et al. (2008) and Hradil et al. (2013) proposed a three-stage material model to simulate the structural behaviour of stainless steel joints and tensile members, which requires the whole range of stress–strain curve up to the ultimate strain to be accurately predicted.

$$\varepsilon = \frac{\sigma - \sigma_{0.2}}{E_{0.2}} + \left(\varepsilon_{1.0} - \varepsilon_{0.2} - \frac{\sigma_{1.0} - \sigma_{0.2}}{E_{0.2}} \right) \left(\frac{\sigma - \sigma_{0.2}}{\sigma_{1.0} - \sigma_{0.2}} \right)^{n'_{0.2,1.0}} + \varepsilon_{0.2} \quad \text{for } \sigma_{0.2} < \sigma \le \sigma_u \quad (2.9)$$

2.3.2 Membrane residual stresses

Residual stresses are important features of hot-rolled steel sections and can lead to premature failure and reduce ultimate resistances of structural members. Lay and Ward (1969) and Szalai and Papp (2005) described the formation of residual stresses in hot-rolled steel sections, which were attributed to different cooling temperatures of the constituent plates of the cross-section and the straightening process used after the cooling process. As reported in Gardner and Cruise (2009), bending residual stresses in hot-rolled structural sections were generally low, only membrane residual stresses in hot-rolled steel sections were measured and the corresponding predictive models of membrane residual stresses were developed. Galambos and Ketter (1959), Young (1972) and Szalai and Papp (2005) performed a series of membrane residual stress measurements on hot-rolled carbon steel I-sections by means of the sectioning method and developed several predictive models, which followed the same general pattern but using different distribution parameters and magnitudes. The Swedish regulations BSK 99 (BSK 2003) and European convention ECCS (ECCS 1976) specify predictive models to determine the distributions and amplitudes of membrane residual stresses in hot-rolled and welded carbon steel I-sections; note that membrane residual stresses in hot-rolled carbon steel I-sections are much less than those in welded carbon steel I-sections. Madugula et al. (1997) conducted membrane residual

stress measurements on 42 hot-rolled carbon steel angle sections, where the measured results were scattered and no predictive models were proposed. The membrane residual stresses in hot-rolled stainless steel angle sections were measured and presented in Cruise and Gardner (2008), where membrane residual stresses were found to be insignificant. To date, research on membrane residual stresses in hot-rolled stainless steel channel sections remains unexplored, with measurements and predictive models of membrane residual stresses reported in Chapter 3.

2.3.3 Cross-section behaviour

2.3.3.1 Previous experimental investigations

Considering that studies into stainless steel channel sections are limited, previous testing, numerical modelling and design of normal strength steel and high strength steel channel sections are firstly reviewed herein. Table 2.1 reports the details of experimental studies into press-braked and welded steel lipped and plain channel sections under isolated and combined loadings. Specifically, Rasmussen and Hancock (1989), Ungermann et al. (2012a, 2012b, 2014), Li et al. (2020) and Mahar et al. (2021) studied the local buckling behaviour and resistance of press-braked and welded normal strength steel plain channel sections under pure compression and developed new design methods to address the shortcomings of the existing design methods. Sivakumaran and Abdel-Rahman (1988), Shanmugam and Dhanalakshmi (2001), Yan and Young (2002), Young and Hancock (2003), Young (2004), Dinis and Camotim (2004), Silvestre and Camotim (2006), Zhang et al. (2007) and Wang et al. (2016) experimentally and numerically investigated the local buckling, distortional buckling and local–distortional interactive buckling behaviour and resistance of press-braked normal strength steel lipped channel sections under pure compression, highlighted a significant post-buckling strength reserve and developed improved design methods to supplement the codified design rules. Yu and Schafer (2002, 2006) performed four-point bending tests on press-braked normal strength steel lipped channel section beams to study their local buckling and distortional

buckling behaviour, assessed the relevant codified design rules and proposed new design methods. Ungermann et al. (2012a, 2012b, 2014) studied the cross-section behaviour and resistances of press-braked normal strength steel plain channel sections under combined compression and bending and local buckling was shown to be the only one failure mode for all tested stub column specimens; based on the test and numerical results, the accuracy of the codified and revised design rules was assessed. Wang et al. (2020a) and Zhang et al. (2019) conducted stub column tests on press-braked high strength steel plain channel sections under pure compression, investigated their local buckling behaviour and cross-section compression resistance and assessed the accuracy of the codified and newly proposed design methods. Kwon and Hancock (1992), Yang and Hancock (2004) and Kwon et al. (2009) investigated the local buckling, distortional buckling and local–distortional interactive buckling behaviour of press-braked high strength steel lipped channel sections under pure compression through testing and numerical modelling and analysed their post-buckling behaviour, with the codified design rules assessed and new design methods developed. Maduliat et al. (2012), Wang et al. (2019) and Zhang et al. (2020c) performed four-point bending tests and numerical modelling on press-braked high strength steel plain and lipped channel sections to study their in-plane flexural behaviour and resistance and evaluated the accuracy of the codified design rules by comparing the obtained test and numerical results against the design cross-section resistances. To address the inaccuracy and cumbersome calculation procedure of existing design methods for press-braked normal and high strength steel channel sections under isolated and combined loadings, direct strength method was developed, which allowed for beneficial interaction between cross-section plate elements and directly related the cross-section resistance to the cross-section slenderness (Schafer and Ádány 2006; Ádány and Schafer 2008; Schafer 2008; Li and Schafer 2010; Young et al. 2013).

Kuwamura (2003), Dobrić et al. (2017) and Zhang et al. (2020a) studied the local buckling behaviour and cross-section resistances of press-braked stainless steel plain channel sections under pure compression based on testing and numerical modelling, while Kuwamura (2003), Lecce and Rasmussen (2006a, 2006b), Fan et al. (2014) and

Chen et al. (2018, 2020a) conducted testing and numerical modelling on press-braked stainless steel lipped channel sections under pure compression to investigate their local buckling and distortional buckling behaviour. The local buckling behaviour and in-plane flexural resistances of press-braked and laser-welded stainless steel channel section beams were experimentally and numerically investigated by Zhang et al. (2020a) and Theofanous et al. (2015), respectively. The local buckling behaviour and distortional buckling behaviour of press-braked stainless steel lipped channel sections under pure bending were studied and reported in Fan et al. (2021, 2022), with the accuracy of codified design rules assessed. Liang et al. (2019a, 2019b, 2020) and Zhang et al. (2021b, 2021c) conducted experimental and numerical programmes to investigate the local buckling behaviour and cross-section resistances of laser-welded and press-braked stainless steel channel section stub columns under combined compression and bending, highlighted the inaccuracy of codified design interaction curves and developed new improved design interaction curves. Fan et al. (2014) and Chen et al. (2018) presented experimental and numerical studies into the local buckling and distortional buckling behaviour and resistances of press-braked stainless steel lipped channel sections under combined compression and bending and assessed the existing design methods based on the obtained test and numerical data. All the aforementioned studies highlighted that the current design codes result in unduly conservative cross-section resistance predictions for stainless steel channel sections under isolated and combined loadings, owing to the use of 0.2% proof stress as the design stress without considering material strain hardening of stainless steel. To overcome this shortcoming, a deformation-based continuous strength method (Afshan and Gardner 2013; Zhao et al. 2017; Zhao and Gardner 2018), considering material strain hardening in calculating cross-section resistances of stainless steel channel sections, was developed and shown to result in much improved design accuracy.

2.3.3.2 Codified design provisions for local buckling

The existing international design codes employ the cross-section classification framework and an elastic, perfectly plastic material model for the design of hot-rolled

stainless steel channel sections with susceptibility to local buckling. The class of a hot-rolled stainless steel channel section is defined according to its most slender constituent plate element. The cross-section resistances of hot-rolled stainless steel channel sections under isolated loading depend on their cross-section classes. Specifically, the European code EN 1993-1-4 (2015) specifies four cross-section classes: Class 1 and 2 (plastic) sections under bending are capable of attaining the plastic moment capacities M_{pl}, Class 3 (elastic) sections under bending can achieve the elastic moment capacities M_{el} and Class 4 (slender) sections under bending fail before the material 0.2% proof stresses (the design stresses) are achieved, with the design bending resistances limited to the effective moment capacities M_{eff}. Hot-rolled stainless steel channel sections under bending are defined as compact, non-compact and slender sections in the American specification ANSI/AISC 370-21 (AISC 2021). ANSI/AISC 370-21 (2021) adopts M_{pl} as the design bending resistances for compact channel section beams and considers partial plasticity in the prediction of design bending resistances for non-compact channels section beams, while for slender channel section beams, the effective moment capacities M_{eff} are taken as their design bending resistances. Regarding cross-section compression resistances, both the European code (CEN 2015) and American specification (AISC 2021) adopt the cross-section yield load N_{pl} for non-slender (Class 1–3) channel section stub columns and the effective compression capacities N_{eff} for slender (Class 4) channel section stub columns. The effective cross-section compression and bending resistances for slender channel sections are determined using effective width method, which was firstly proposed by Winter (1947) and then revised in each design code. The effective width method treats a cross-section as an assemblage of isolated plate elements without considering element interaction and reduces the plate element width to account for the loss of effectiveness caused by local buckling. For the design of channel sections under combined compression and bending, the European code (CEN 2015) employs a linear interaction formula, which is a simple linear summation of the utilisation ratio for each stress resultant with an upper limit taken as unity, while the American specification (AISC 2021) uses a bi-linear interaction formula. Detailed discussions on the codified local buckling design provisions for hot-rolled stainless steel channel sections under isolated and combined loadings are given in Chapters 3–5.

2.3.3.3 Continuous strength method

Continuous strength method (CSM) is an advanced deformation-based design method, which was proposed by Gardner (2002) and Gardner and Nethercot (2004), further developed by Gardner and Ashraf (2006), Ashraf et al. (2006, 2008a, 2008b) and Gardner (2008b) and finalised by Afshan and Gardner (2013), Zhao et al. (2017) and Zhao and Gardner (2018). The main advantage of the CSM (Afshan and Gardner 2013; Zhao et al. 2017; Zhao and Gardner 2018) lies in (i) the adoption of a continuous 'base curve' to quantify the deformation capacity (reflected by the maximum attainable compressive stain) of the considered cross-section under the applied loading and (ii) the employment of a bi-linear (elastic, linear strain hardening) material model to allow the design stress greater than the 0.2% proof stress $\sigma_{0.2}$ to be achieved. The CSM uses a continuous treatment in place of the codified cross-section classification framework and considers the favourable cross-section element interaction and material strain hardening of stainless steel, thus leading to a high level of design accuracy and consistency in the prediction of cross-section resistances (Ashraf et al. 2008a, 2008b; Saliba and Gardner 2013; Liew and Gardner 2015; Zhao et al. 2015a, 2015b, 2016b, 2016c; Buchanan et al. 2016; Sun et al. 2019; Sun and Zhao 2019; Liang et al. 2019b, 2020; Zhang et al. 2019, 2021b, 2021c). Detailed discussions on the CSM for hot-rolled stainless steel channel sections are provided in Chapters 3–5.

Table 2.1. Summary of previous tests on steel channel sections

No.	Reference	Material	Section type	Loading condition	No. of tests	Failure mode
1	Rasmussen and Hancock (1989)	NSS	Welded plain channel	Compression	7	LB
2	Ungermann et al. (2012a)	NSS	Press-braked plain channel	Compression	5	LB
				Combined loading	5	LB
3	Li et al. (2020)	NSS	Press-braked plain channel	Compression	12	LB
4	Sivakumaran and Abdel-Rahman (1988)	NSS	Press-braked lipped channel	Compression	20	LB
5	Yan and Young (2002)	NSS	Press-braked lipped channel	Compression	3	LB
					12	LB+DB
6	Young and Hancock (2003)	NSS	Press-braked lipped channel	Compression	42	DB
7	Zhang et al. (2007)	NSS	Press-braked lipped channel	Compression	10	LB+DB
8	Wang et al. (2016)	NSS	Press-braked lipped channel	Compression	4	LB
					2	LB+DB
9	Yu and Schafer (2002)	NSS	Press-braked lipped channel	Bending	24	LB
10	Yu and Schafer (2006)	NSS	Press-braked lipped channel	Bending	20	DB
11	Wang et al. (2020a)	HSS	Press-braked plain channel	Compression	10	LB
12	Zhang et al. (2019)	HSS	Press-braked plain channel	Compression	16	LB
13	Kwon and Hancock (1992)	HSS	Press-braked lipped channel	Compression	6	DB
					16	LB+DB
14	Yang and Hancock (2004)	HSS	Press-braked lipped channel	Compression	9	LB
					12	LB+DB
15	Kwon et al. (2009)	HSS	Press-braked lipped channel	Compression	17	LB+DB
16	Wang et al. (2019)	HSS	Press-braked plain channel	Bending	20	LB

17	Zhang et al. (2020c)	HSS	Press-braked plain channel	Bending	12	LB
18	Maduliat et al. (2012)	HSS	Press-braked plain channel	Bending	2	LB
			Press-braked lipped channel		40	LB+DB
19	Kuwamura (2003)	SS	Press-braked plain channel	Compression	11	LB
			Press-braked lipped channel		12	LB
20	Dobrić et al. (2017)	SS	Press-braked plain channel	Compression	4	LB
21	Zhang et al. (2020a)	SS	Press-braked plain channel	Compression	4	LB
				Bending	4	LB
22	Lecce and Rasmussen (2006a)	SS	Press-braked lipped channel	Compression	19	DB
23	Fan et al. (2014)	SS	Press-braked lipped channel	Compression	10	LB
				Combined loading	28	LB
24	Chen et al. (2018)	SS	Press-braked lipped channel	Compression	1	LB
					4	DB
				Combined loading	6	LB
					7	DB
25	Theofanous et al. (2015)	SS	Laser-welded plain channel	Bending	12	LB
26	Fan et al. (2021)	SS	Press-braked lipped channel	Bending	6	LB
27	Fan et al. (2022)	SS	Press-braked lipped channel	Bending	8	DB
28	Liang et al. (2019a, 2020)	SS	Laser-welded plain channel	Combined loading	23	LB
29	Zhang et al. (2021b, 2021c)	SS	Press-braked plain channel	Combined loading	20	LB

Note: NSS represents normal strength steel; HSS represents high strength steel; SS represents stainless steel; LB represents local buckling; DB represents distortional buckling.

2.3.4 Member behaviour

2.3.4.1 Previous experimental investigations

A brief review of previous research into the structural behaviour and resistance of steel channel section members failing by isolated and interactive buckling is firstly provided herein, with the experimental details reported in Table 2.2. Specifically, Rasmussen and Hancock (1989), Young and Rasmussen (1995, 1998a, 1998b, 1999), Kwon et al. (2007), Ungermann et al. (2012a, 2012b, 2014), Ye et al. (2018a, b) and Li et al. (2021b) conducted a series of pin-ended and fix-ended compression tests on welded and press-braked normal strength steel plain channel section columns to investigate their flexural buckling, local–flexural interactive buckling and local–flexural-torsional interactive buckling behaviour, and highlighted the inaccuracy of the codified design rules by comparing the test failure loads against the design resistances. Young and Rasmussen (1998c), Yan and Young (2002), Zhang et al. (2007), Camotim and Dinis (2011), Gunalan and Mahendran (2013), Santos et al. (2014), Wang et al. (2016), Anbarasu and Murugapandian (2016) and Ye et al. (2018a, b) experimentally and numerically investigated the buckling behaviour and resistance of press-braked normal strength steel lipped channel section columns, including flexural buckling, flexural-torsional buckling, local–flexural interactive buckling, local–flexural-torsional interactive buckling, distortional–flexural interactive buckling, distortional–flexural-torsional interactive buckling, local–distortional–flexural interactive buckling, local–distortional–flexural-torsional interactive buckling; based on the obtained test and numerical data, the relevant codified design rules were evaluated and new improved design provisions were developed. Rasmussen and Hancock (1989), Zhang et al. (2007), Ungermann et al. (2012a, 2012b, 2014), Torabian et al. (2015) and Wang et al. (2016) conducted a series of pin-ended compression tests on press-braked normal strength steel lipped channel section beam-columns with short, intermediate and long member lengths subjected to combined compression and bending moment and the obtained experimental observations revealed that their failure modes were highly dependent on stress distribution. Wang

et al. (2020b), Zhang et al. (2022) and Zhang and Zhao (2022) studied the flexural buckling behaviour and resistance of press-braked high strength steel channel section columns through testing and numerical modelling and highlighted the shortcomings of codified buckling curves. Gunalan and Mahendran (2013) studied the flexural-torsional buckling behaviour of press-braked high strength steel lipped channel section columns based on testing and numerical modelling, found the conservatism of current codified design buckling curves and developed new improved design buckling curves. Experimental studies into the local–flexural interactive buckling, local–flexural-torsional interactive buckling, local–distortional–flexural interactive buckling and local–distortional–flexural-torsional interactive buckling behaviour of press-braked high strength steel columns with plain and lipped channel sections were conducted by Kwon et al. (2009) and Zhang and Zhao (2022), with the progression of different buckling modes analysed and existing design methods assessed. To improve the design accuracy of press-braked normal and high strength steel channel section members failing by isolated and interactive buckling, direct strength method was extended to the member design and calculated the reduction in member resistance caused by local bucking based on the gross cross-section. (Schafer 2002, 2019; Torabian et al. 2014; Torabian and Schafer 2018; Dinis et al. 2020).

Dobrić et al. (2020) and Zhang et al. (2020b) experimentally and numerically investigated the flexural buckling and flexural-torsional buckling behaviour of press-braked stainless steel plain channel section columns, highlighted the inaccuracy of the codified buckling curves and proposed new improved buckling curves. Pin-ended and fixed-ended compression tests and numerical modelling on press-braked stainless steel lipped channel section columns were conducted by Becque and Rasmussen (2009a, b), Rossi et al. (2010a, b), Anbarasu and Ashraf (2016) and Chen et al. (2018, 2022) to investigate their local–flexural interactive buckling behaviour, local–flexural-torsional interactive buckling behaviour, distortional–flexural interactive buckling behaviour, distortional–flexural-torsional interactive buckling behaviour. Zhang et al. (2021a) conducted testing and numerical modelling on press-braked stainless steel plain channel section beam-columns, studied their global buckling

behaviour and highlighted the inaccuracy of the current codified design interaction curves.

2.3.4.2 Codified design provisions for member buckling

The current European code (CEN 2015) and American specification (AISC 2021) employ the same concept of buckling curves for the design of hot-rolled stainless steel channel section columns failing by flexural buckling. It is worth noting that the effects of initial geometric imperfections and residual stresses on column buckling resistances have been inherently considered in the design buckling curves. Detailed discussions on the codified column buckling curves are provided in Chapter 6. For the design of hot-rolled stainless steel channel section beam-columns, interaction curves are employed in both design codes (CEN 2015; AISC 2021), where the column buckling resistance and cross-section bending resistance are taken as the end points, while the interaction factor is adopted to define the shape of the design interaction curve. Detailed discussions on the codified design interaction curves for hot-rolled stainless steel channel section beam-columns are given in Chapter 7.

Table 2.2. Summary of previous tests on steel channel section members

No.	Reference	Material	Channel section type	Loading condition	No. of tests	Failure mode
1	Rasmussen and Hancock (1989)	NSS	Welded plain channel	Compression	18	FB
				Combined loading	17	GB
2	Young and Rasmussen (1998a)	NSS	Press-braked plain channel	Compression	15	LB+FB
					5	FB
3	Kwon et al. (2007)	NSS	Welded plain channel	Compression	4	LB+FB/FTB
4	Ungermann et al. (2012a)	NSS	Welded plain channel	Compression	4	LB+FB
				Combined loading	2	GB
			Press-braked plain channel	Compression	8	LB+FB
5	Ye et al. (2018a)	NSS	Press-braked plain channel	Compression	9	LB+FB
			Press-braked lipped channel	Compression	27	LB+FB
6	Li et al. (2021b)	NSS	Press-braked plain channel	Compression	12	LB+FB
7	Yan and Young (2002)	NSS	Press-braked lipped channel	Compression	3	LB+DB+FTB
					9	LB+FTB
8	Zhang et al. (2007)	NSS	Press-braked lipped channel	Compression	1	LB+DB+FB
					7	DB+FB
					4	LB+FB
				Combined loading	12	GB
9	Santos et al. (2014)	NSS	Press-braked lipped channel	Compression	17	DB+FB/FTB
10	Wang et al. (2016)	NSS	Press-braked lipped channel	Compression	6	LB+FB
					6	LB+DB+FB
				Combined loading	12	GB

11	Gunalan and Mahendran (2013)	NSS	Press-braked lipped channel	Compression	4	FTB
		HSS	Press-braked lipped channel	Compression	2	FTB
12	Torabian et al. (2015)	NSS	Press-braked lipped channel	Combined loading	55	GB
13	Wang et al. (2020b)	HSS	Press-braked plain channel	Compression	10	FB
14	Zhang et al. (2022)	HSS	Press-braked plain channel	Compression	10	FB
15	Zhang and Zhao (2022)	HSS	Press-braked plain channel	Compression	6	FB
					6	LB+FB
16	Kwon et al. (2009)	HSS	Press-braked lipped channel	Compression	8	LB+FB/FTB
					2	LB+DB+FB/FTB
17	Zhang et al. (2020b)	SS	Press-braked plain channel	Compression	12	FB
18	Becque and Rasmussen (2009a)	SS	Press-braked lipped channel	Compression	29	LB+FB
19	Rossi et al. (2010a)	SS	Press-braked lipped channel	Compression	48	DB+FTB
20	Chen et al. (2018)	SS	Press-braked lipped channel	Compression	2	DB+FB/FTB
				Combined loading	6	GB
21	Chen et al. (2022)	SS	Press-braked lipped channel	Compression	21	DB+FB/FTB
22	Zhang et al. (2021a)	SS	Press-braked plain channel	Combined loading	10	GB

Note: NSS represents normal strength steel; HSS represents high strength steel; SS represents stainless steel; LB represents local buckling; DB represents distortional buckling; FB represents flexural buckling; FTB represents flexural-torsional buckling; GB represents global buckling.

2.4 Concluding remarks

This chapter has presented an overview of previous research relevant to the present thesis, including (i) development of international design codes for stainless steel structural members, (ii) material properties of stainless steel, (iii) membrane residual stresses in thin-walled steel structural sections, (iv) buckling behaviour of stainless steel channel sections and members under isolated and combined loadings and (v) codified and advanced design approaches. The literature review generally shows that (i) the distributions and amplitudes of membrane residual stresses in hot-rolled stainless steel channel sections, (ii) the local buckling behaviour of hot-rolled stainless steel channel sections under isolated and combined loadings, (iii) the flexural buckling behaviour of hot-rolled stainless steel channel section columns and (iv) the global buckling behaviour of hot-rolled stainless steel channel section beam-columns remain unexplored. Therefore, testing, numerical modelling and design of hot-rolled stainless steel channel section members are the objectives of the present thesis.

CHAPTER 3

LOCAL BUCKLING OF CHANNEL SECTIONS UNDER PURE COMPRESSION

3.1 Introduction

This chapter presents experimental and numerical studies of the local buckling behaviour and cross-section resistances of hot-rolled stainless steel channel sections under pure compression. An experimental programme was firstly conducted and included material testing, membrane residual stress measurements, initial local geometric imperfection measurements and six stub column tests. Following the experimental programme, a numerical modelling programme was performed, where finite element models were developed to replicate the test observations and then used to perform parametric studies to generate further numerical data over a wide range of cross-section aspect ratios and dimensions. The obtained test and numerical data were then used to assess the slenderness limits and local buckling design rules given in the European code EN 1993-1-4 (CEN 2015) and American specification ANSI/AISC 370-21 (AISC 2021) for hot-rolled stainless steel channel sections under pure compression. The accuracy of the continuous strength method (Afshan and Gardner 2013; Zhao et al. 2017; Zhao and Gardner 2018) for the design of hot-rolled stainless steel channel sections under pure compression was also evaluated. The partial findings of this research work have been reported in Li et al. (2021a).

3.2 Testing

3.2.1 General

Given that there have been no stub column tests conducted on hot-rolled stainless steel channel sections, an experimental programme was firstly conducted. Three plain channel sections – C 80×40×5, C 100×50×5 and C 100×50×6, hot-rolled from grade EN 1.4301 austenitic stainless steel sheets, were adopted in the experimental programme. The cross-section labelling system consists of a letter 'C' (indicating a channel section) and the nominal cross-section sizes in millimetres (outer web width B_w × outer flange width B_f × wall thickness t). On the basis of the slenderness limits given in the European code EN 1993-1-4 (CEN 2015), C 80×40×5 and C 100×50×6 are classified as Class 2, while C 100×50×5 is categorised as Class 3. Two stub column specimens with the same member length were prepared for each channel section. The identifier for each stub column specimen includes the cross-section label ('C1', 'C2' and 'C3' signifying C 80×40×5, C 100×50×5 and C 100×50×6, respectively), a letter ('S' representing 'stub column') and a number ('1' or '2'). Table 3.1 reports the measured geometric dimensions for the six stub column specimens, where L is the member length, B_w is the outer web width, B_f is the outer flange width, t is the wall thickness and r is the corner inner radius. Figure 3.1 shows the notations of geometric parameters of hot-rolled stainless steel channel sections.

Table 3.1. Measured geometric dimensions and initial local geometric imperfections of hot-rolled stainless steel channel section stub column specimens.

Cross-section	Specimen ID	L (mm)	B_w (mm)	B_f (mm)	t (mm)	r (mm)	ω_{f1} (mm)	ω_{f2} (mm)	ω_w (mm)	ω_0 (mm)
80×40×5	C1-S1	178.2	80.46	39.75	4.79	4.74	0.03	0.02	0.01	0.03
	C1-S2	178.3	80.39	39.80	4.72	4.75	0.02	0.05	0.04	0.05
100×50×5	C2-S1	225.8	98.91	49.75	4.80	4.84	0.03	0.03	0.04	0.04
	C2-S2	219.0	98.93	49.69	4.72	4.76	0.03	0.04	0.03	0.04
100×50×6	C3-S1	224.2	100.11	49.15	5.62	5.61	0.06	0.02	0.05	0.06
	C3-S2	224.4	100.16	49.18	5.72	5.74	0.03	0.05	0.02	0.05

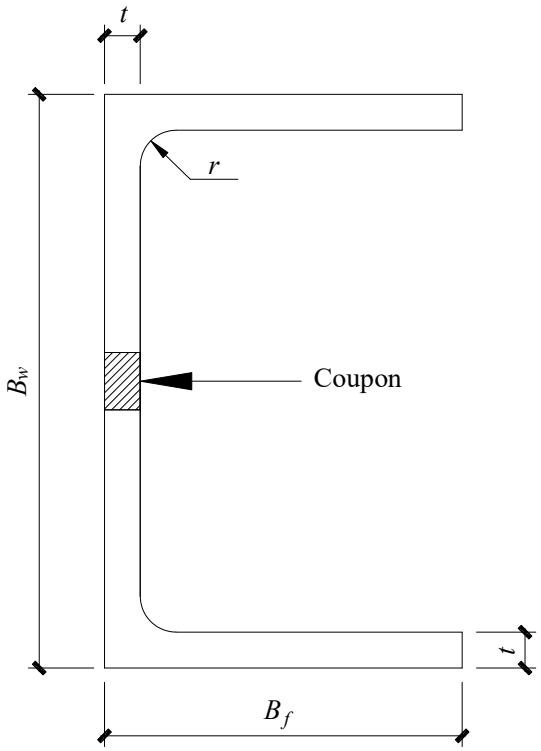

Figure 3.1. Notations of geometric parameters of hot-rolled stainless steel channel sections and locations of coupons.

3.2.2 Material testing

Tensile coupon tests were carried out to obtain the material properties of the adopted hot-rolled stainless steel channel sections. Flat coupons were extracted from the middle parts of the web and flanges in the longitudinal direction – see Figure 3.1, and the coupon dimensions were machined in accordance with the requirements given in the European code EN ISO 6892-1 (CEN 2016), as illustrated in Figure 3.2(a). A Schenck 250 kN hydraulic testing machine was adopted to conduct the material tensile coupon tests under displacement control, with the rates equal to 0.05 mm/min and 0.8 mm/min before and after the material 0.2% proof stress, respectively. The material test setup is shown in Figure 3.2(b), where two strain gauges are attached to the mid-height of the coupon to measure tensile strains in the longitudinal direction and an extensometer is mounted onto the necked part of the coupon to record the elongation over the gauge length of 50 mm. The label of each coupon includes the

cross-section identifier and the location indicator within channel section ('F1', 'F2' and 'W' signifying flanges and web, respectively). The obtained key material properties are reported in Table 3.2, where E is the Young's modulus, $\sigma_{0.2}$ is the 0.2% proof stress, σ_u is the ultimate stress, ε_u is the strain at the ultimate stress, ε_f is the strain at fracture, and n and $n'_{0.2,1.0}$ are the parameters used in the Ramberg–Osgood (R–O) material model expressed by Equations (2.1) and (2.9) (Gardner and Nethercot 2004; Arrayago et al. 2015). Figure 3.3(a) and Figure 3.3(b) show the measured material stress–strain curves of the adopted channel sections.

3.2.3 Initial local geometric imperfection measurements

The structural behaviour and resistances of thin-walled steel channel section members are affected by their initial geometric imperfections. Therefore, the initial local geometric imperfections of each hot-rolled stainless steel channel section stub column specimen were measured. The test setup, recommended by Schafer and Peköz (1998) and having been successfully used in previous initial local geometric imperfection measurements (Theofanous and Gardner 2015; Zhang et al. 2020a, 2021b, 2021c), was also employed. Figure 3.4 displays the test setup, where a stub column specimen is mounted on the flat work bench of a CNC router and three LVDTs, perpendicularly pointing to the constituent plate elements of the specimen, are moved along the member longitudinal direction. The initial local geometric imperfection magnitude of each constituent plate element was calculated as the maximum deviation from the measured data to a reference line (obtained through a prior linear regression analysis based on the whole measured data set). Table 3.1 reports the measured initial local geometric imperfection magnitudes of the three constituent plate elements of each stub column specimen, where ω_{f1} and ω_{f2} denote the values of the two flanges, while ω_w denotes the value of the web. The initial local geometric imperfection magnitude of each stub column specimen ω_0 is taken as the maximum of ω_{f1}, ω_{f2} and ω_w, as also reported in Table 3.1.

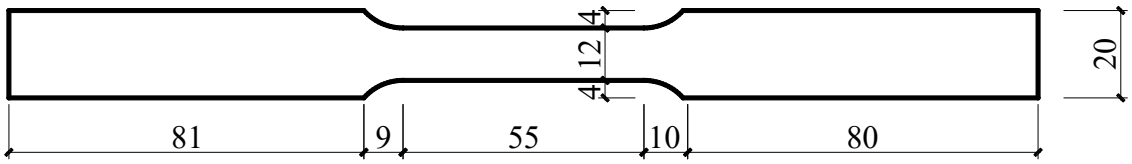

(a) Coupon dimensions

(b) Test setup.

Figure 3.2. Material tests.

Table 3.2. Summary of key measured material properties from tensile coupon tests.

Cross-section	Coupon ID	E (GPa)	$\sigma_{0.2}$ (MPa)	σ_u (MPa)	ε_u (%)	ε_f (%)	R–O parameters n	R–O parameters $n'_{0.2,1.0}$
C 80×40×5	C1-W	205	363	700	53.0	66.9	6.4	2.4
	C1-F1	200	354	757	58.0	75.0	8.1	1.6
	C1-F2	202	352	721	58.6	69.4	7.4	2.1
C 100×50×5	C2-W	204	352	707	50.0	62.1	8.4	2.5
	C2-F1	202	327	743	57.7	73.0	12.8	2.4
	C2-F2	203	316	741	60.0	65.4	11.7	1.9

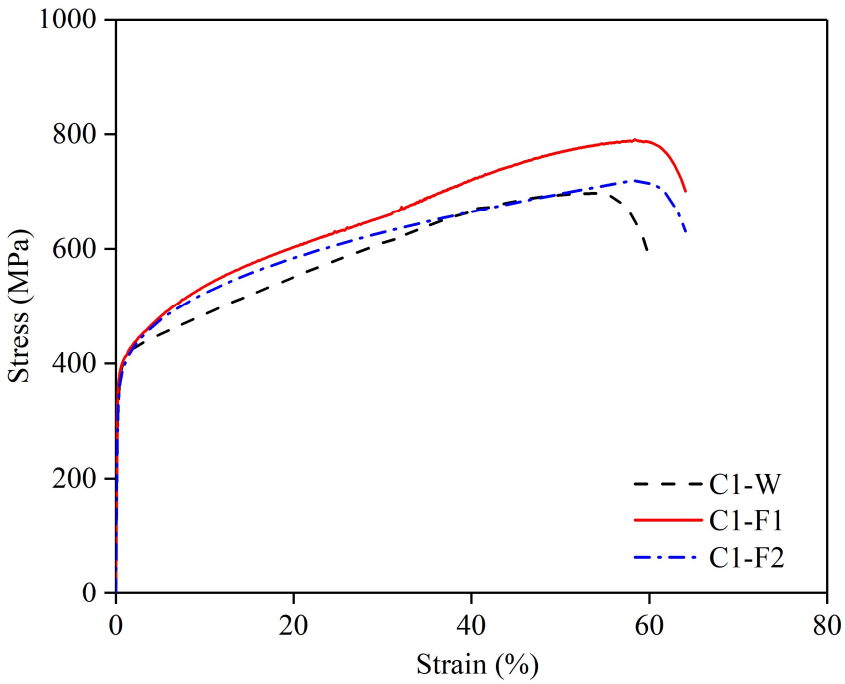

(a) 80×40×5

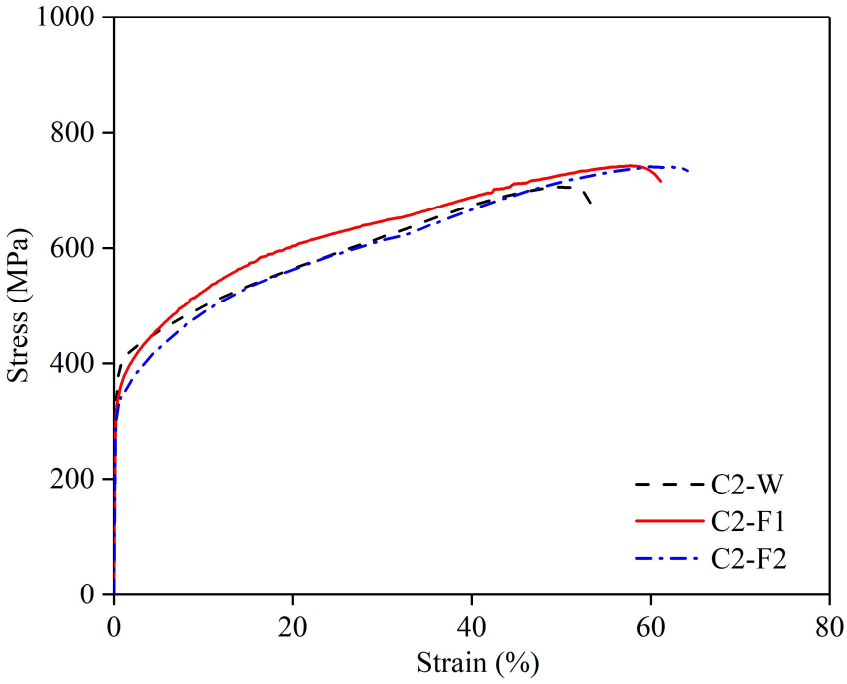

(b) 100×50×5

Figure 3.3. Measured material stress–strain curves.

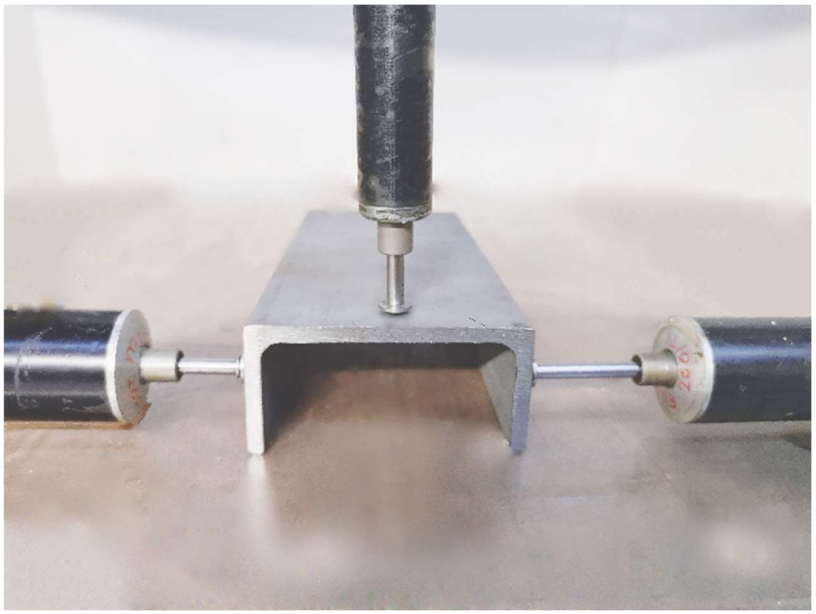

Figure 3.4. Test setup for initial local geometric imperfection measurements.

3.2.4 Membrane residual stress measurements

Membrane residual stress measurements were conducted on two large-sized (representative) hot-rolled stainless steel channel sections C 100×50×5 and C 150×75×6, based on the sectioning method and the recommended procedures given in Ziemian (2010). Figure 3.5 and Figure 3.6 display the locations and dimensions of strips within the two representative hot-rolled stainless steel channel sections before sectioning; the nominal lengths of the strips are 150 mm, with the widths ranging from 6 mm to 10 mm (depending on regions). Prior to sectioning, two gauge holes with a diameter of 1.98 mm were drilled along the centreline of the outer face of each strip and at a distance of 25 mm from the strip ends, through the use of an automatic dot puncher, leading to the nominal length between the two gauge holes L_0 equal to 100 mm; the actual strip length between the two gauge holes was then measured by using a Demec gauge. Upon length measurements of the strips within channel sections, each specimen was cut into strips, allowing for the release of membrane residual stresses; a typical sectioned C 150×75×6 specimen is shown in Figure 3.7. The Demec gauge was again adopted to measure the strip lengths after sectioning. For each strip, the readings of the Demec gauge taken before and after sectioning are

denoted as r_1 and r_2, respectively. To eliminate the influence of temperature changes during the membrane residual stress measurements, a temperature reference bar, made of the same material as the hot-rolled stainless steel channel section stub column specimens, was used, with the lengths measured before and after the sectioning process denoted as t_1 and t_2, respectively.

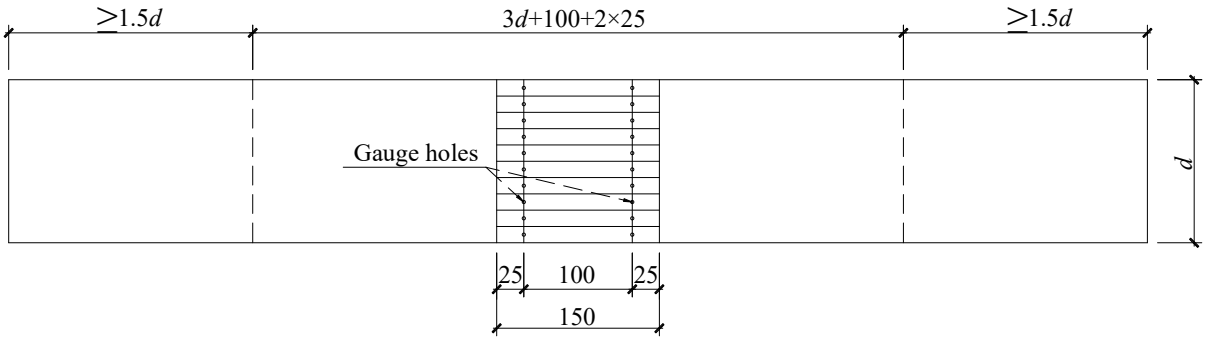

Figure 3.5. Locations of strips cut for membrane residual stress measurements (in mm).

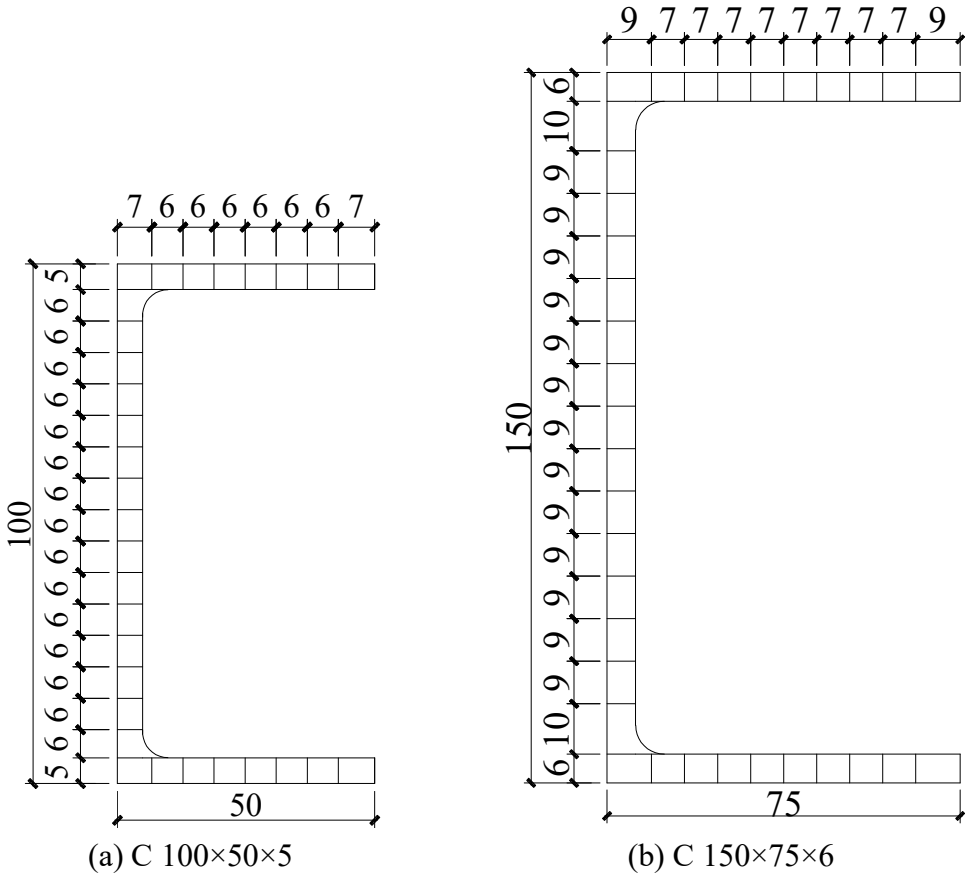

(a) C 100×50×5 (b) C 150×75×6

Figure 3.6. Locations and dimensions of strips within channel sections (in mm).

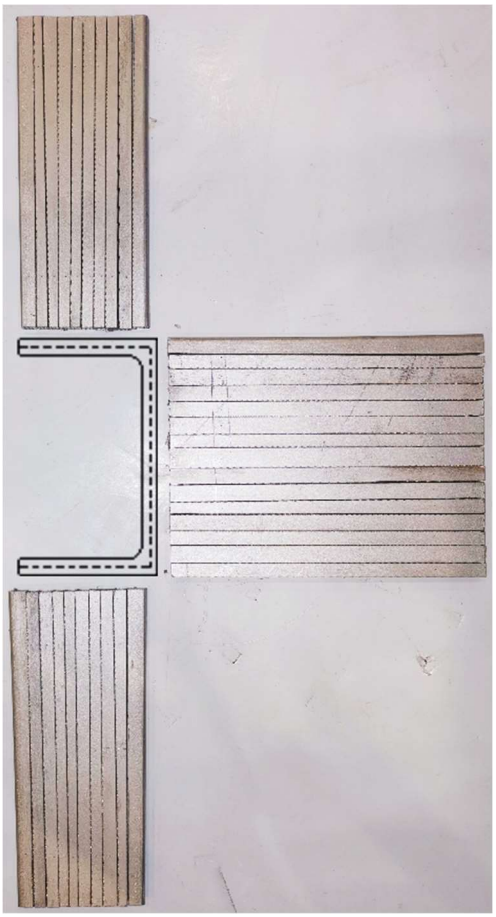

Figure 3.7. Typical sectioned C 150×75×6 specimen.

On the basis of the readings obtained from the Demec gauge and temperature reference bar before and after sectioning, the relieved membrane residual strains can be calculated from Equation (3.1); note that positive (calculated) strains signify tensile membrane residual stresses, while negative strains determined from Equation (3.1) indicate compressive membrane residual stresses. For strips within the web-to-flange junction regions, where high through-thickness residual stress gradients exist and result in slightly curved strips after sectioning, the relieved membrane residual strains calculated from Equation (3.1) were further corrected according to Equation (3.2) (Tebedge et al. 1973) to eliminate the influence of longitudinal curvature, where δ is the maximum deviation from a straight reference line connecting the two gauge holes of the strip.

$$\varepsilon = \frac{\left(r_1 - t_1\right) - \left(r_2 - t_2\right)}{L_0 + \left(r_1 - t_1\right)} \tag{3.1}$$

$$\varepsilon_c = \varepsilon + \frac{\left(\delta / L_0\right)^2}{6\left(\delta / L_0\right)^4 + 1} \tag{3.2}$$

Upon determination of the relieved membrane residual strains for all the strips, the corresponding membrane residual stresses were then calculated through multiplying the relieved membrane residual strains by the Young's moduli obtained from the material tensile coupon tests, as shown in Figure 3.8(a) and Figure 3.8(b) for the two hot-rolled stainless steel channel sections C 100×50×5 and C 150×75×6; note that positive and negative values signify tensile and compressive membrane residual stresses, respectively. The obtained maximum tensile and compressive membrane residual stresses were normalised by the corresponding measured yield stresses (the 0.2% proof stresses), as reported in Table 3.3, where the subscripts '*w*' and '*f*' represent the web and flange, respectively, while the subscripts '*c*' and '*t*' denote the compressive and tensile membrane residual stresses, respectively. Figure 3.9(a) and Figure 3.9(b) show the measured membrane residual stress patterns and amplitudes in a normalised format; note that the normalised position at the origin point 0.0 corresponds to the web-to-flange junction, while the normalised position at point 1.0 represents the mid-point of the web or the flange tip. On the basis of the experimental data, a predictive model, as shown in Figure 3.10, was proposed for predicting membrane residual stresses in hot-rolled stainless steel channel sections, with linear distribution patterns for the flange and half of the web and the maximum compressive (or tensile) membrane residual stress magnitudes equal to $0.3\sigma_{0.2}$. The proposed predictive model was shown to agree well with the measured membrane residual stress data – see Figure 3.9.

Table 3.3. Measured peak membrane residual stresses in hot-rolled stainless steel channel sections.

Cross-section	$\sigma_{wt}/\sigma_{0.2}$	$\sigma_{ft}/\sigma_{0.2}$	$\sigma_{wc}/\sigma_{0.2}$	$\sigma_{fc}/\sigma_{0.2}$
C 100×50×5	0.20	0.18	-0.23	-0.16
	0.22	0.25	-0.23	-0.24
C 150×75×6	0.23	0.26	-0.20	-0.22
	0.25	0.17	-0.20	-0.16

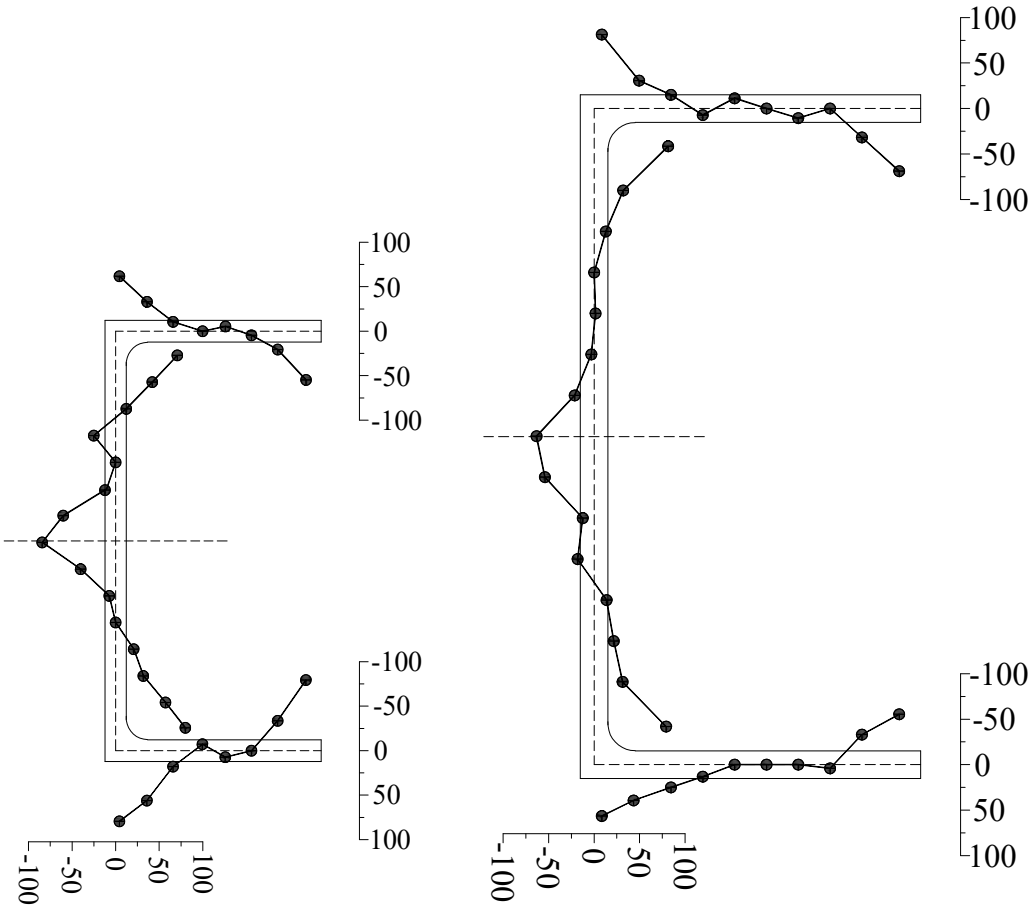

(a) C 100×50×5 (b) C 150×75×6

Figure 3.8. Measured membrane residual stress patterns and amplitudes (in MPa).

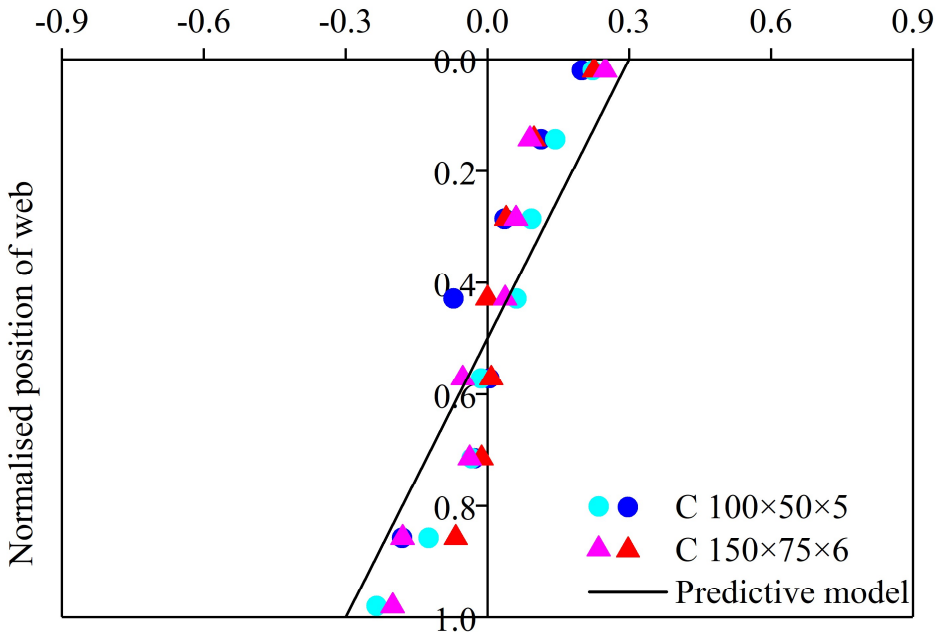

(a) Web

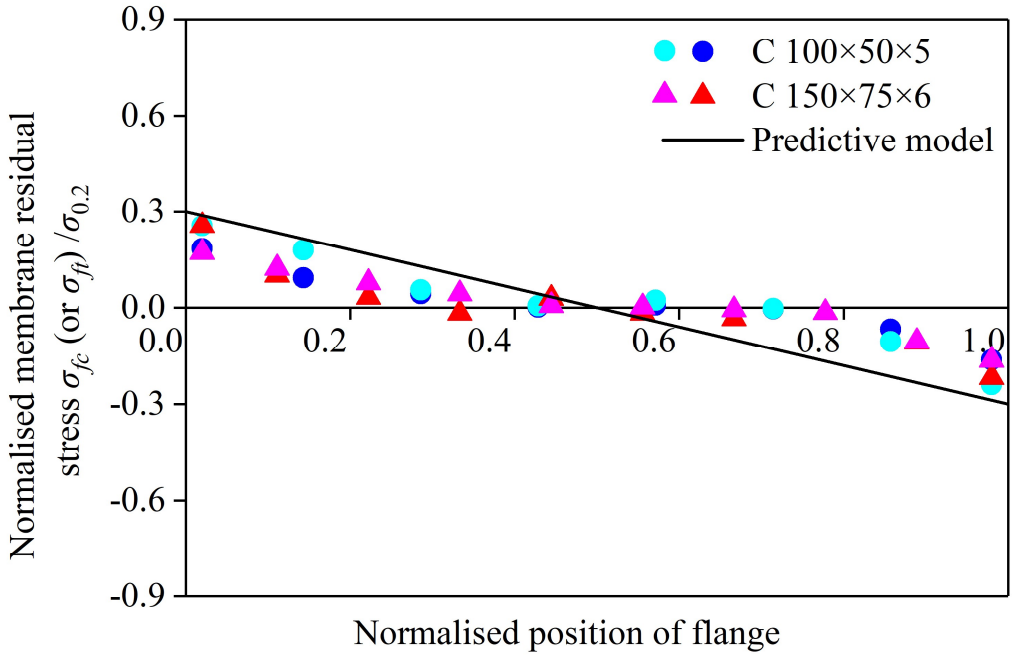

(b) Flange

Figure 3.9. Comparisons between measured membrane residual stress patterns and amplitudes and predictive model.

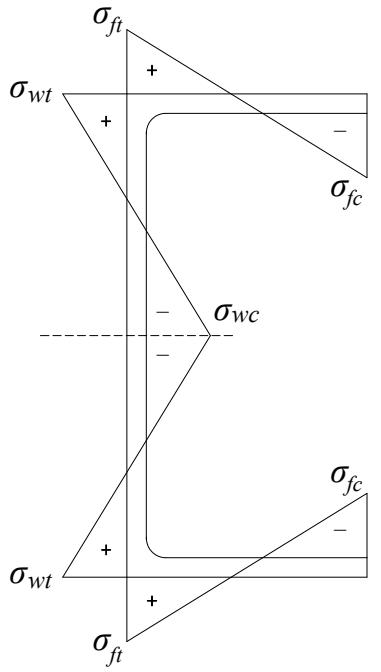

Figure 3.10. Membrane residual stress predictive model for hot-rolled stainless steel channel sections.

3.2.5 Stub column tests

Compression tests were carried out to study the local buckling behaviour and resistances of hot-rolled stainless steel channel section stub column specimens under pure compression. Before testing, milling and deburring were performed on the stub column specimen ends such that flat and parallel end surfaces of the stub column specimens and thus uniformly distributed compressive stresses over the whole end sections were achieved during testing. All the compression tests were conducted using a displacement-controlled Instron 2000 kN hydraulic testing machine at a rate of 0.3 mm/min. The test setup is presented in Figure 3.11, where (i) fixed bearing platens are equipped at the two ends of the testing machine to provide fixed-ended boundary conditions, (ii) clamping devices are employed at the specimen ends to prevent cross-sections from any deformation, (iii) three LVDTs are positioned at the stub column specimen end to measure the end shortening and (iv) two strain gauges are attached to the web and flange at mid-height to measure the longitudinal strains.

Note that the LVDT readings include both the end shortenings of the specimen and the deformations of the bearing platens of the testing machine. Therefore, the actual end shortenings of each stub column specimen were corrected based on the strain gauge data by subtracting the deformations of the bearing platens of the testing machine from the LVDT readings (Centre for Advanced Structural Engineering, 1990; Gardner and Nethercot, 2004). The corrected load–end shortening curves for all the adopted hot-rolled stainless steel channel section stub column specimens are presented in Figure 3.12, while the key test results are reported in Table 3.4, where $N_{u,test}$ is the failure load, δ_u is the end shortening at failure and $N_{u,test}/(A\sigma_{0.2})$ is the ratio of the test failure load to cross-section yield load, where A is the gross cross-section area. All the six hot-rolled stainless steel channel section stub column specimens failed by local buckling, with typical failure modes shown in Figure 3.13.

Figure 3.11. Stub column test setup.

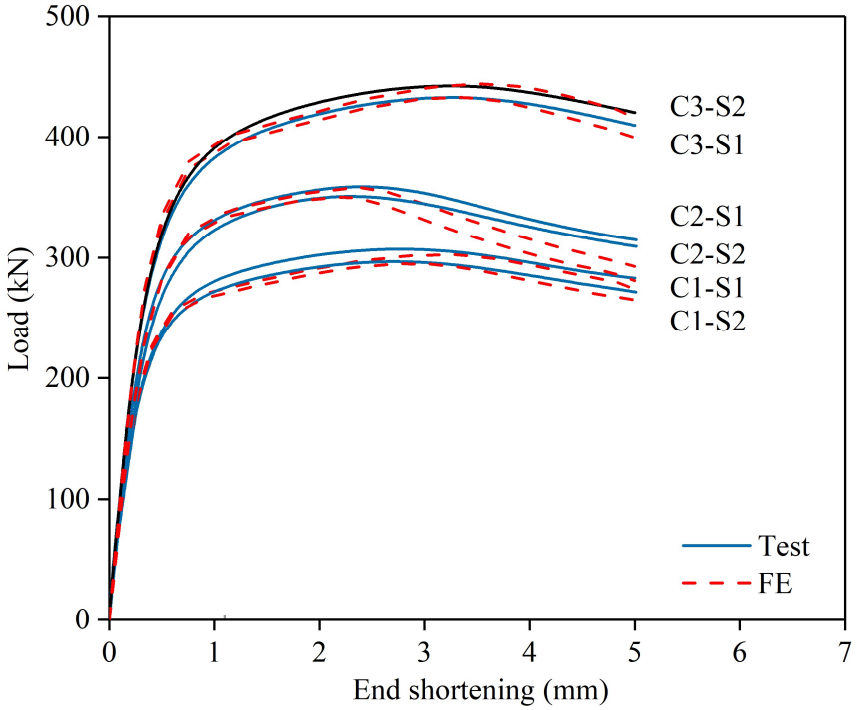

Figure 3.12. Load–end shortening curves of hot-rolled stainless steel channel section stub column specimens.

Table 3.4. Summary of key stub column test results

Cross section	Specimen ID	$N_{u,test}$ (kN)	δ_u (mm)	$N_{u,test}/(A\sigma_{0.2})$ (kNm)
80×40×5	C1-S1	307.1	2.79	1.19
	C1-S2	296.7	2.70	1.17
100×50×5	C2-S1	358.8	2.39	1.11
	C2-S2	350.9	2.31	1.10
100×50×6	C3-S1	432.7	3.24	1.15
	C3-S2	442.2	3.26	1.15

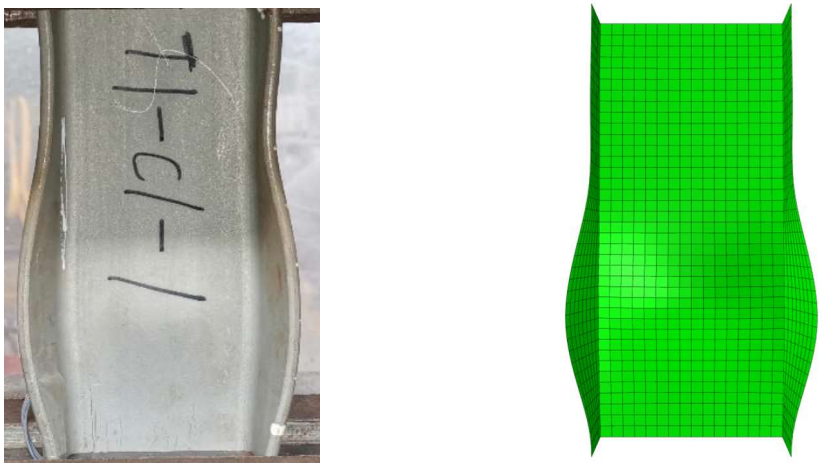

(a) C1-S1

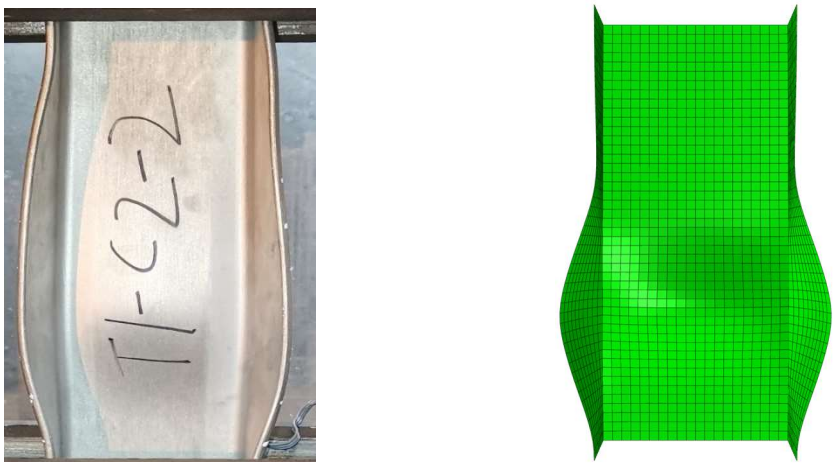

(b) C2-S2

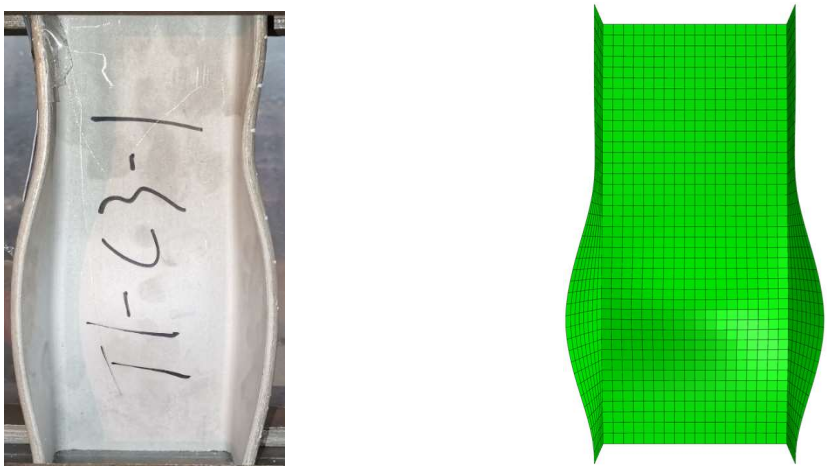

(c) C3-S1

Figure 3.13. Test and FE failure modes for typical stub column specimens.

3.3 Numerical modelling

3.3.1 General

Following the experimental programme, a numerical modelling programme was conducted using the finite element (FE) package ABAQUS (ABAQUS 2014). FE models were firstly developed and validated against the test results and then used to perform parametric studies to generate further numerical data.

3.3.2 Development and validation of FE models

The four-node doubly curved shell element S4R (ABAQUS 2014), which is provided in the ABAQUS element library and allows for finite membrane strains and large rotations, has been widely and successfully adopted in previous nonlinear numerical modelling of thin-walled steel (carbon steel (Xiang et al. 2019; Wang et al. 2020a, 2020b), aluminium alloy (Zhu et al. 2019; Zhou and Young 2020) and stainless steel (Becque and Rasmussen 2009b; Dobrić et al. 2017, 2020; Liang et al. 2019a, 2019b, 2020; Lan et al. 2021)) channel section members and was also employed herein. A prior mesh sensitivity study considering mesh sizes varying between $0.2t \times 0.2t$ and $2t \times 2t$ was conducted to seek suitable element sizes which could result in a good balance between computational efficiency and accuracy. The final selected element size was taken equal to $t \times t$. Regarding the material modelling of hot-rolled stainless steel channel sections, the plastic material model with isotropic hardening was employed. Specifically, the engineering stress–strain curves measured from tensile coupon tests were firstly converted into the true stress–plastic strain curves, based on Equations (3.3) and (3.4), where σ_{nom} is the engineering stress, ε_{nom} is the engineering strain, σ_{true} is the true stress, and ε_{ln}^{pl} is the true plastic strain, and then assigned to the stub column FE models. Given that bending residual stresses have been incorporated into the measured engineering stress–strain curves, only membrane residual stresses were modelled in the stub column FE models (Gardner and Cruise 2009; Huang and

Young 2012; Chen and Young 2021). The predictive model presented in Section 3.2.4 was used to calculate the membrane residual stresses, which were then inputted into the stub column FE models using the 'Predefined Field' command (ABAQUS 2014); Figure 3.14 displays the membrane residual stress pattern and amplitudes incorporated into the FE model for the typical stub column specimen C2-S1.

$$\sigma_{true} = \sigma_{nom}\left(1+\varepsilon_{nom}\right) \tag{3.3}$$

$$\varepsilon_{ln}^{pl} = \ln\left(1+\varepsilon_{nom}\right) - \frac{\sigma_{true}}{E} \tag{3.4}$$

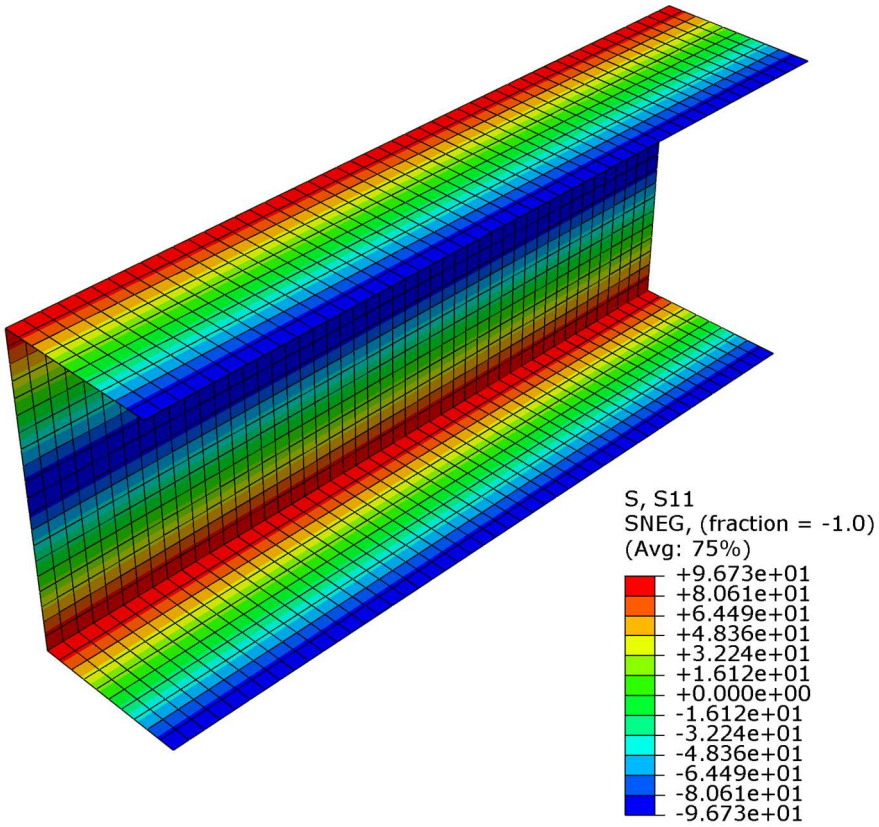

Figure 3.14. Modelled membrane residual stress pattern and amplitudes (in MPa) for stub column specimen C2-S1.

For ease of application of boundary conditions, each end section of the channel section stub column FE model was coupled to a concentric reference point; then, the bottom reference point was fully restrained, while the top reference point was only allowed for longitudinal translation, to mimic the fixed-ended boundary conditions used in the stub column tests. Initial local geometric imperfections were included into

each stub column FE model, with the distribution pattern taken as the lowest elastic local buckling mode shape. Two local imperfection magnitudes, including the measured value ω_0 and a generalised value t/100, were used to factor the distribution pattern. Upon development of the hot-rolled stainless steel channel section stub column FE models, the modified Risk method, considering material and geometric nonlinearities, was conducted to obtain the numerical failure loads, load–end shortening curves and failure modes.

Validation of the developed stub column FE models was conducted by comparing the numerical results with their experimental counterparts. Table 3.5 reports the numerical to test failure load ratios $N_{u,FE}/N_{u,test}$ for all the hot-rolled stainless steel channel section stub column specimens, with the results revealing that both the measured and generalised local imperfection magnitudes result in accurate predictions of the test failure loads. Comparisons between the test and numerical load–end shortening curves for all the stub column specimens are presented in Figure 3.12, where the test load–deformation histories are generally shown to be well captured by their numerical counterparts. Figure 3.13 displays the test and numerical failure modes for typical stub column specimens, indicating good agreement. In summary, the test structural responses of the hot-rolled stainless steel channel section stub column specimens under pure compression can be well simulated by the developed FE modes, which are therefore regarded as having been validated.

3.3.3 Parametric studies

Having been validated in Section 3.3.2, the developed stub column FE models were adopted to perform parametric studies to generate further numerical data on hot-rolled stainless steel channel section stub columns over a wide range of cross-section aspect ratios and dimensions. In the parametric studies, the adopted modelling procedures and techniques were the same as those described in Section 3.3.2, but with the use of the generalised local imperfection magnitude – t/100 and the material properties of the hot-rolled stainless steel channel section C 80×40×5. Regarding the cross-section geometric dimensions of the modelled hot-rolled stainless steel channel section stub

columns, the outer web widths B_w were fixed at 150 mm, while five outer flange widths B_f equal to 50 mm, 60 mm, 75 mm, 100 mm and 150 mm were selected, with the wall thicknesses t varied between 2.7 mm and 21.4 mm, leading to five cross-section web-to-flange aspect ratios (1.0, 1.5, 2.0, 2.5 and 3.0) and a range of cross-section sizes being considered. It is worth highlighting that the modelled channel sections covered all four classes in EN 1993-1-4 (CEN 2015). The length of each stub column FE model was taken as three times the mean outer web and flange widths (Ziemian 2010). Finally, 60 numerical data have been generated for hot-rolled stainless steel channel section stub columns under pure compression.

Table 3.5. Comparisons of numerical failure loads with test failure loads for varying initial local geometric imperfection magnitudes.

Cross section	Specimen ID	$N_{u,FE}/N_{u,test}$	
		ω_0	$t/100$
80×40×5	C1-S1	0.99	0.98
	C1-S2	0.99	0.99
100×50×5	C2-S1	1.00	0.99
	C2-S2	1.00	0.98
100×50×6	C3-S1	1.00	1.00
	C3-S2	1.00	1.00
	Mean	1.00	0.99
	COV	0.01	0.01

3.4 Assessment of existing international design standards

3.4.1 General

The relevant design rules, as given in EN 1993-1-4 (CEN 2015) and ANSI/AISC 370-21 (AISC 2021), for hot-rolled stainless steel channel sections under pure compression, were firstly described and discussed. Their accuracy and consistency were then assessed by comparing the test and numerical failure loads N_u with the design failure loads $N_{u,pred}$. Note that all the partial safety factors adopted in the existing design codes were taken as unity, leading to unfactored design resistances

being assessed. Table 3.6 reports the mean test and numerical to predicted cross-section resistance ratio ($N_u/N_{u,pred}$) and the corresponding coefficient of variation (COV) for each design method.

Table 3.6. Comparisons of test and numerical failure loads with predicted failure loads from different design methods.

No. of test data: 6 No. of FE data: 60	$N_u/N_{u,EC3}$	$N_u/N_{u,AISC}$	$N_u/N_{u,csm}$
Mean	1.15	1.20	1.06
COV	0.07	0.07	0.02

3.4.2 EN 1993-1-4

3.4.2.1 Overview

The European code EN 1993-1-4 (EC3) (CEN 2015) provides supplementary design rules for stainless steel structures in addition to the general design rules for mild steel structures set out in EN 1993-1-1 (2014). For the design of hot-rolled stainless steel channel sections prone to local buckling, the existing European code EN 1993-1-4 (CEN 2015) adopts the framework: (i) cross-section classification based on the codified slenderness limits and (ii) determination of compression resistance for the classified cross-section. In Section 3.4.2.2, the accuracy of the codified slenderness limits for the cross-section classification of hot-rolled stainless steel channel section stub columns was assessed, while the relevant design rules for determining cross-section compression resistances were evaluated in Section 3.4.2.3.

3.4.2.2 Class 3 slenderness limits

EN 1993-1-4 (CEN 2015) specifies four cross-sections in compression – Class 1, 2, 3 and 4. For Class 1–3 (non-slender) cross-sections, local buckling occurs after the material yield stress is attained, with the compression resistance at failure greater than

or equal to the yield load, while for Class 4 (slender) cross-sections, the earlier occurrence of local buckling prevents them from the attainment of the material yield stress, with the resulting compressive resistance at failure less than the yield load. The class of a hot-rolled stainless steel channel section is defined according to its most slender constituent plate element, and the classification of a plate element is defined by comparing its width-to-thickness ratio $c/t\varepsilon$ against the EC3 codified slenderness limits, where c is the flat element width and $\varepsilon=[(235/\sigma_{0.2})/(E/210000)]^{0.5}$ is a material parameter. Specifically, the flat element width of the outstand flange is equal to the outer flange width excluding the web thickness $c_f=B_f-t$, while the flat element width of the internal web is taken as the outer web width excluding the flange thicknesses $c_w=B_w-2t$. The codified slenderness limit for classifying non-slender and slender outstand flanges in compression is taken as $c_f/t\varepsilon=14$, while the slenderness limit for classifying non-slender and slender internal webs in compression is equal to $c_w/t\varepsilon=37$.

The accuracy of the slenderness limit of 14 for outstand flanges in compression is evaluated, with the results presented in Figure 3.15, where the test and numerical failure loads for hot-rolled stainless steel channel section stub columns N_u are normalised by the cross-section yield loads $N_{pl}=A\sigma_{0.2}$ and plotted against $c_f/t\varepsilon$. Similar graphical evaluation of the accuracy of the slenderness limit of 37 for internal web in compression is shown in Figure 3.16, where the normalised test and numerical data points N_u/N_{pl} are plotted against $c_w/t\varepsilon$. The graphical evaluation results revealed that the codified slenderness limits are accurate for cross-section classification of hot-rolled stainless steel channel section stub columns.

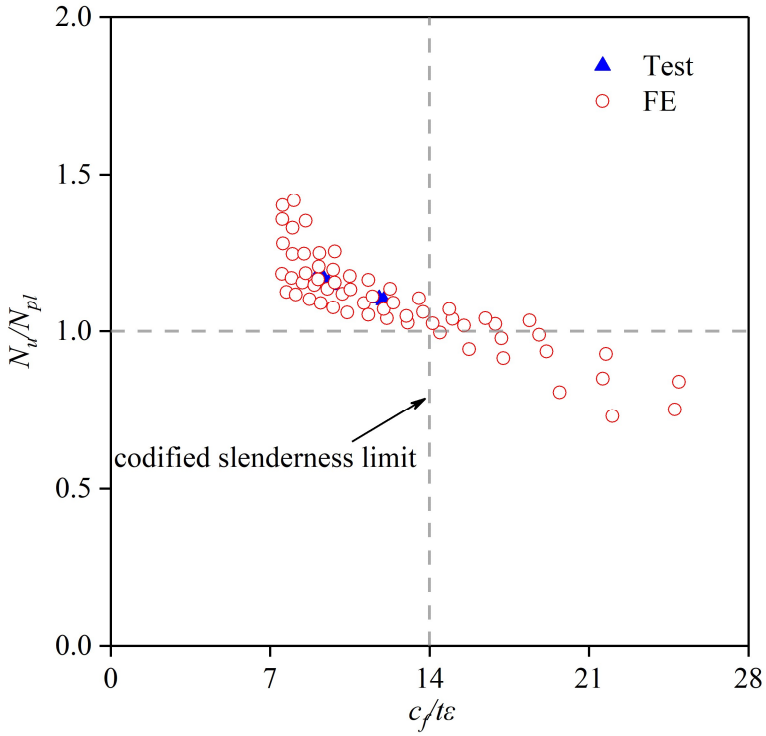

Figure 3.15. Evaluation of codified slenderness limit for outstand flanges in compression.

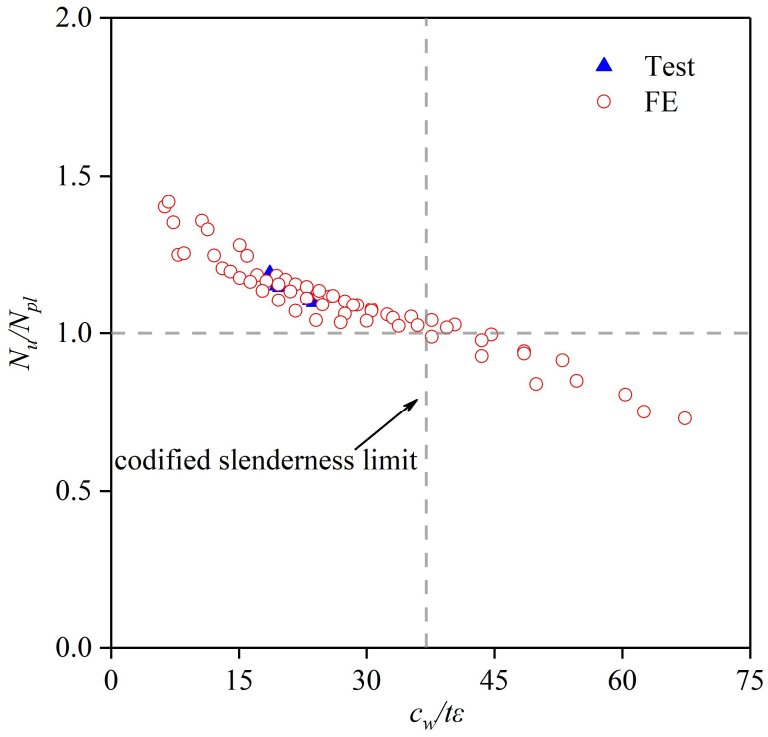

Figure 3.16. Evaluation of codified slenderness limit for internal web in compression.

3.4.2.3 Cross-section compression resistances

The European code EN 1993-1-4 (CEN 2015) specifies that the cross-section compression resistance $N_{u,EC3}$ is equal to the yield load $N_{pl}=A\sigma_{0.2}$ for Class 1–3 cross-sections but the effective compression resistance $N_{eff}=A_{eff}\sigma_{0.2}$ for Class 4 cross-sections, as given by Equation (3.5), where A_{eff} is the effective cross-section area. For a slender channel section, the effective cross-section area is equal to the summation of the gross areas of the non-slender plate elements that are not susceptible to local buckling and the effective areas of the slender plate elements that are susceptible to local buckling. The effective area of each slender plate element is calculated as the wall thickness t multiplied by the effective plate element width c_{eff}, as determined based on the effective width method by Equation (3.6), where $\bar{\lambda}_l$ is the plate element slenderness given by Equation (3.7), where k_σ is the EC3 plate buckling factor and equal to 0.43 for outstand flanges in compression but 4.0 for internal web in compression (CEN 2006b).

$$N_{u,EC3} = \begin{cases} A\sigma_{0.2} & \text{for Class } 1-3 \text{ cross-sections} \\ A_{eff}\sigma_{0.2} & \text{for Class 4 cross-sections} \end{cases} \tag{3.5}$$

$$c_{eff} = \begin{cases} c\left(\dfrac{1}{\bar{\lambda}_l} - \dfrac{0.188}{\bar{\lambda}_l^2}\right) \le c & \text{for outstand flanges} \\ c\left(\dfrac{1}{\bar{\lambda}_l} - \dfrac{0.22}{\bar{\lambda}_l^2}\right) \le c & \text{for internal webs} \end{cases} \tag{3.6}$$

$$\bar{\lambda}_l = \frac{c}{28.4t\varepsilon\sqrt{k_\sigma}} \tag{3.7}$$

14

The failure load predictions of hot-rolled stainless steel channel sections under pure compression, as calculated from the EC3 design rules, were assessed against the test and numerical failure loads. Table 3.6 reports the mean test and numerical to predicted failure load ratio $N_u/N_{u,EC3}$ of 1.15 with the corresponding COV of 0.07, while Figure 3.17 presents the normalised test and numerical data points plotted against the plate element slendernesses $\bar{\lambda}_l$. The quantitative and graphical assessment results revealed that the EC3 design rules result in rather conservative and

scattered failure load predictions, owing to the lack of proper consideration of favourable material strain hardening and beneficial element interaction.

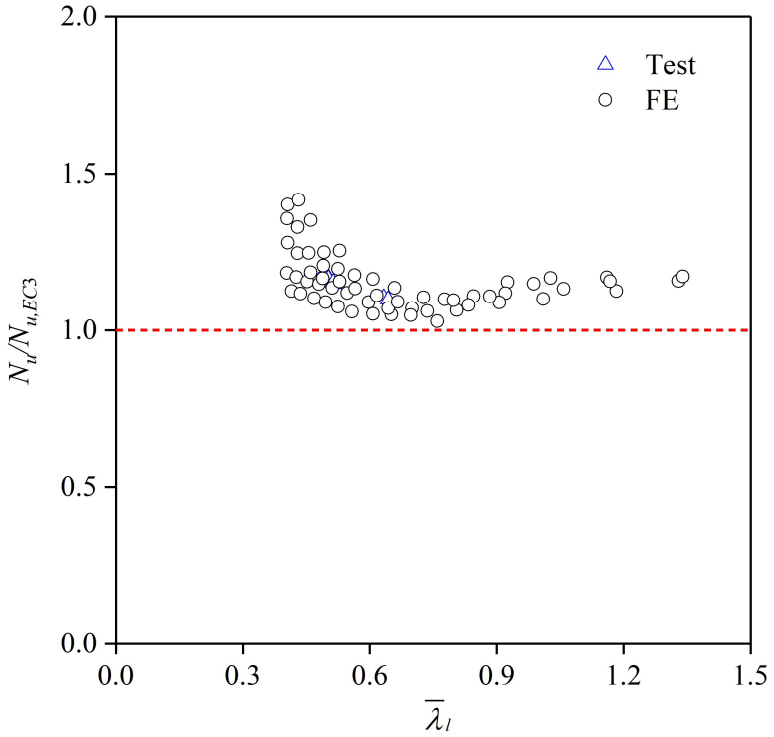

Figure 3.17. Comparisons of test and numerical failure loads with failure load predictions from EN 1993-1-4.

3.4.3 ANSI/AISC 370-21

For the design of hot-rolled stainless steel channel sections under pure compression, the existing American specification ANSI/AISC 370-21 (AISC) (AISC 2021) also adopts the framework: (i) cross-section classification based on the codified slenderness limits and (ii) calculation of compression resistance for the classified cross-section. Cross-sections under compression are categorised as non-slender and slender sections in ANSI/AISC 370-21 (AISC 2021), which correspond to Class 1–3 and Class 4 sections given in EN 1993-1-4 (CEN 2015), respectively. The AISC cross-section compression resistance is equal to the cross-section yield load $N_{pl}=A\sigma_{0.2}$ for non-slender cross-sections but the effective compression resistance $N_{eff}=A_{eff}\sigma_{0.2}$

for slender cross-sections, as expressed by Equation (3.7). Note that ANSI/AISC 370-21 (AISC 2021) adopts the same effective width formulation for both stiffened (internal) and unstiffened (outstand) plate elements, as given by Equation (3.8).

$$N_{u,AISC} = \begin{cases} A\sigma_{0.2} & \text{for no-slender cross-sections} \\ A_{eff}\sigma_{0.2} & \text{for slender cross-sections} \end{cases} \tag{3.7}$$

$$c_{eff} = 0.772c\left(\frac{1}{\overline{\lambda}_l} - \frac{0.1}{\overline{\lambda}_l^2}\right) \leq c \tag{3.8}$$

The cross-section compression resistance predictions for hot-rolled stainless steel channel section stub columns were firstly calculated by the AISC design rules and then compared against the test and numerical data. Figure 3.18 shows the graphical comparison results, where the test and numerical to predicted failure load ratios $N_u/N_{u,AISC}$ are plotted against the plate element slendernesses $\overline{\lambda}_l$, revealing a high level of conservatism. This is also evident by the quantitative assessment results, as reported in Table 3.6, where the mean ratio $N_u/N_{u,AISC}$ is equal to 1.20 and the corresponding COV is taken as 0.07. The high level of conservatism of the AISC design rules is attributed to the neglect of favourable material strain hardening and beneficial element interaction.

3.5 Continuous strength method

The existing international design standards for stainless steel structures ignore the beneficial material strain hardening and plate element interaction and were shown to lead to conservative resistance predictions for hot-rolled stainless steel channel section stub columns. This prompted the development of continuous strength method (Afshan and Gardner 2013; Zhao et al. 2017). The CSM is an advanced deformation-based design method, which was developed to enable rational consideration of material strain hardening and plate element interaction in calculating cross-section resistances.

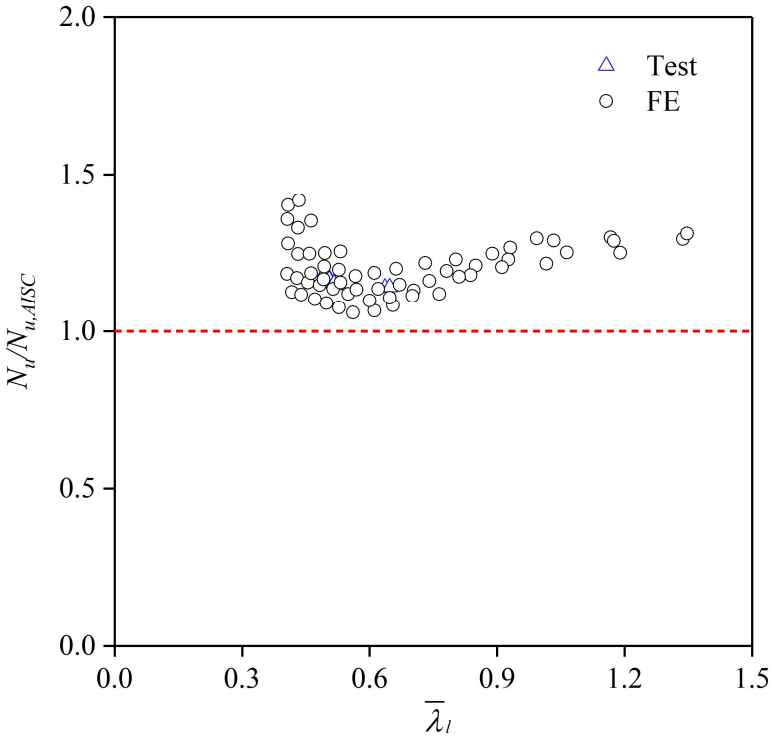

Figure 3.18. Comparisons of test and numerical failure loads with failure load predictions from ANSI/AISC 370-21.

The first step towards using the CSM to determine cross-section resistances lies in the calculation of the cross-section limiting (maximum attainable) compressive strain ε_{csm}, which reflects the deformation capacity of the considered cross-section under the applied loading. This can be achieved based on the CSM base curve (Afshan and Gardner 2013; Zhao et al. 2017), as given by Equation (3.9), where ε_{csm} is the limiting compressive strain, $\varepsilon_y=\sigma_{0.2}/E$ is the material yield strain and $\overline{\lambda}_p=(\sigma_{0.2}/\sigma_{cr})^{0.5}$ is the cross-section slenderness, where σ_{cr} is the elastic critical local buckling stress under the applied loading (Schafer and Ádány 2006). Then, an elastic, linear hardening material model (Buchanan et al. 2016), featuring four material parameters (C_1, C_2, C_3 and C_4) and shown in Figure 3.19, is used to allow the CSM design stress greater than the material 0.2% proof stress to be achieved. C_1 is employed in Equation (3.9) to define a cut-off strain, while C_2 is used in Equation (3.10) to define the strain hardening slope E_{sh}; C_3 and C_4 are used to predict the material ultimate strain $\varepsilon_u=C_3(1-\sigma_{0.2}/\sigma_u)+C_4$. For austenitic stainless steel, C_1, C_2, C_3 and C_4 are taken as 0.10, 0.16, 1.00 and 0.00, respectively (Buchanan et al. 2016). Following calculation of the limiting compressive strain ε_{csm} and the strain hardening slope E_{sh}, the CSM design

compressive stress σ_{csm} is calculated by Equation (3.11). The CSM cross-section compression resistance $N_{u,csm}$ is then determined by Equation (3.12) as the product of the CSM design compressive stress σ_{csm} and the gross cross-section area A.

$$\frac{\varepsilon_{csm}}{\varepsilon_y} = \begin{cases} \dfrac{0.25}{\bar{\lambda}_p^{3.6}} \le \min\left(15, \dfrac{C_1\varepsilon_u}{\varepsilon_y}\right) & \text{for } \bar{\lambda}_p \le 0.68 \\ \left(1 - \dfrac{0.222}{\bar{\lambda}_p^{1.050}}\right) \dfrac{1}{\bar{\lambda}_p^{1.050}} & \text{for } \bar{\lambda}_p > 0.68 \end{cases} \tag{3.9}$$

$$E_{sh} = \frac{\sigma_u - \sigma_{0.2}}{C_2\varepsilon_u - \varepsilon_y} \tag{3.10}$$

$$\sigma_{csm} = \begin{cases} E\varepsilon_{csm} & \text{for } \varepsilon_{csm} < \varepsilon_y \\ \sigma_{0.2} + E_{sh}\left(\varepsilon_{csm} - \varepsilon_y\right) & \text{for } \varepsilon_{csm} \ge \varepsilon_y \end{cases} \tag{3.11}$$

$$N_{u,csm} = A\sigma_{csm} \tag{3.12}$$

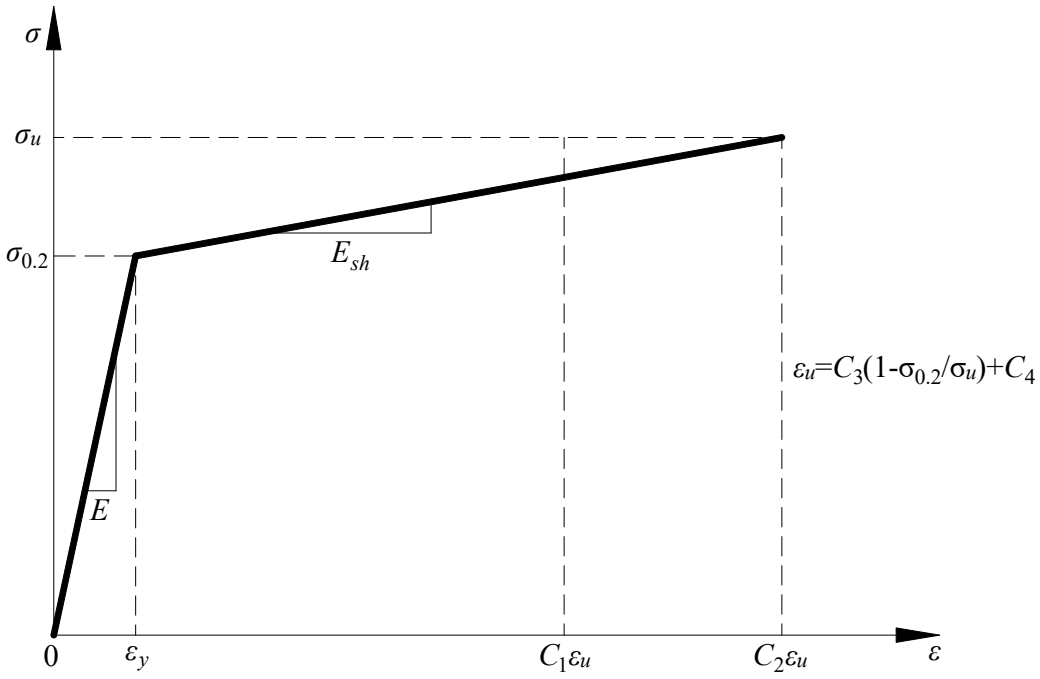

Figure 3.19. CSM bi-linear material model.

The accuracy of the CSM for hot-rolled stainless steel channel section stub columns was assessed by comparing the test and numerical results against the CSM design cross-section resistances, with the quantitative and graphical comparison results reported in Table 3.6 and Figure 3.20, respectively. The comparison results reveal

that the CSM leads to accurate and consistent cross-section compression resistance predictions for hot-rolled stainless steel channel section stub columns, owing to the rational consideration of the favourable material strain hardening and cross-section plate element interaction. Figure 3.21 and Figure 3.22 present the comparisons of the failure load predictions calculated by the codified design rules and the CSM, also revealing the improved design accuracy of the CSM.

The reliability of the CSM for hot-rolled stainless steel channel section stub columns was evaluated, based on the requirements and procedures given in EN 1990 (CEN 2002). In this reliability analysis, the material over-strength ratio for austenitic stainless steel was taken as 1.3, with the COV of 0.06, and the COV of the geometric dimensions of stainless steel sections was taken as 0.05, as recommended by Afshan et al. (2015). Table 3.7 reports the key obtained statistical parameters, where $k_{d,n}$ is the design (ultimate limit state) fractile factor, b is the mean ratio of test and numerical resistances to design model resistances, V_δ is the COV of the test and numerical resistances relative to the resistance model, V_r is the combined COV incorporating all the variable uncertainties and γ_{M0} is the (required) partial safety factor. The calculated (required) partial safety factor, as reported in Table 3.7, is less than the current limit value of 1.1 in EN 1993-1-4 (CEN 2015), thus confirming the reliability of the CSM for hot-rolled stainless steel channel section stub columns.

Table 3.7. Reliability analysis results calculated according to EN 1990.

No. of data	$k_{d,n}$	b	V_δ	V_r	γ_{M0}
66	3.24	1.06	0.02	0.08	0.94

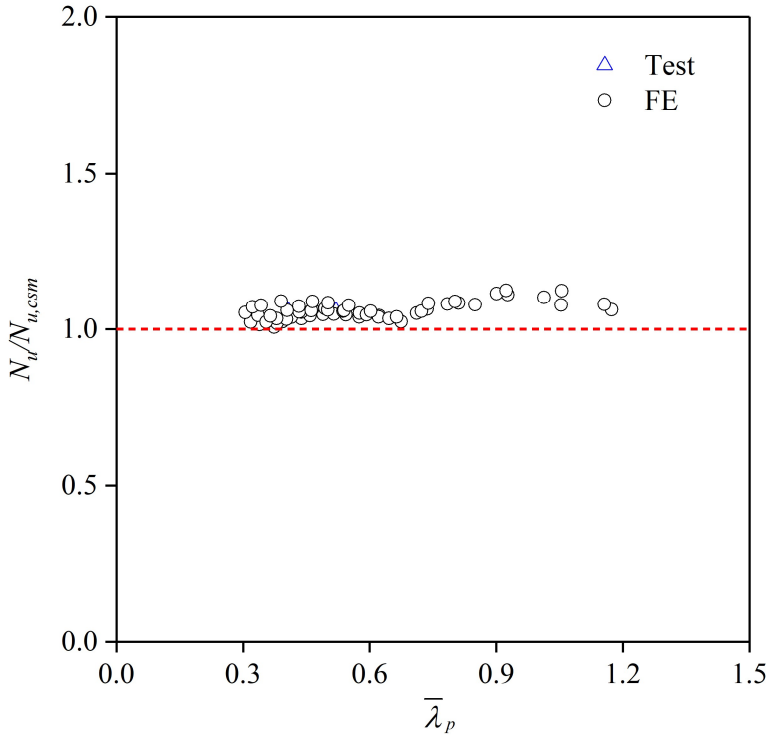

Figure 3.20. Comparisons of test and numerical failure loads with failure load predictions from CSM.

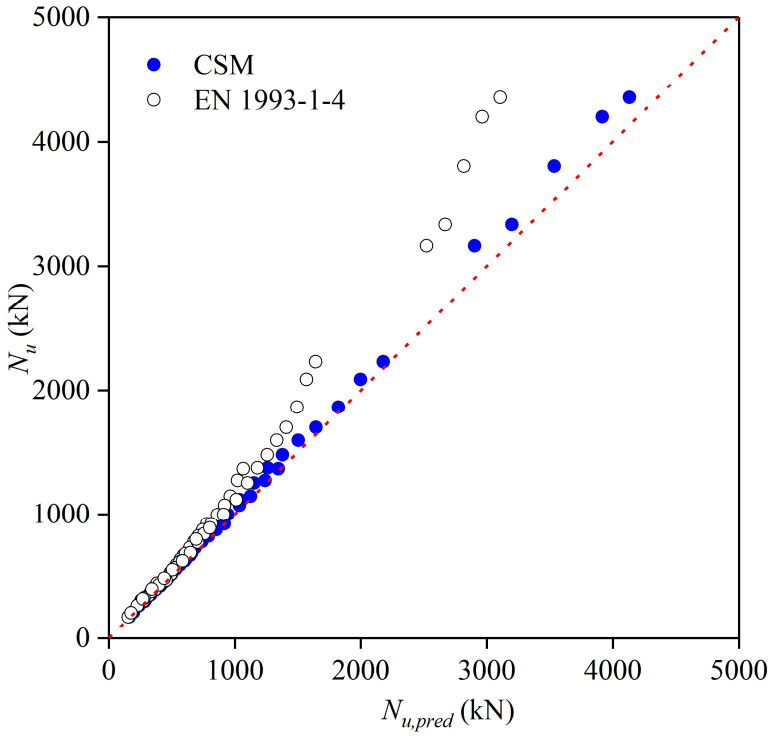

Figure 3.21. Test and FE failure loads compared with failure load predictions from EN 1993-1-4 and CSM.

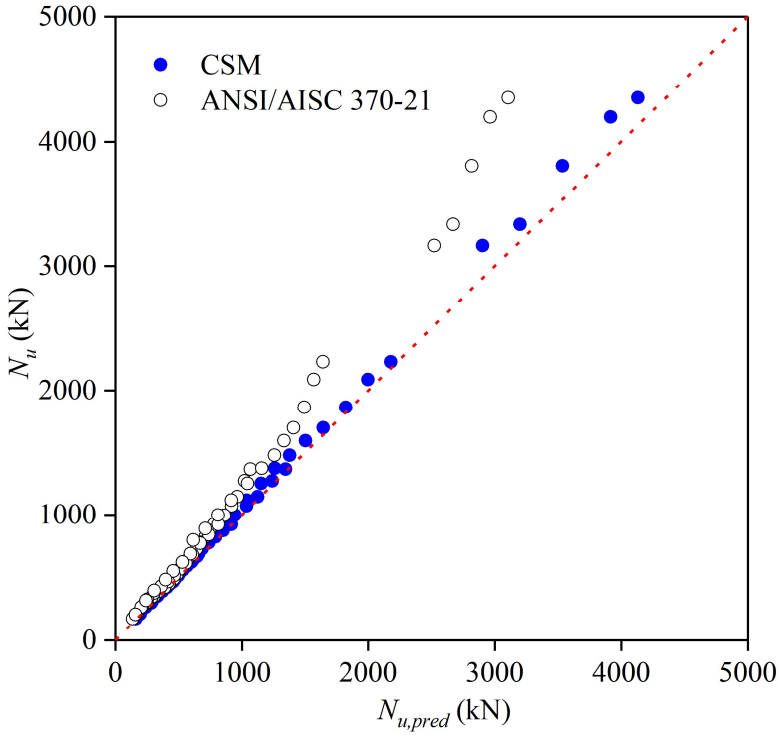

Figure 3.22. Test and FE failure loads compared with failure load predictions from ANSI/AISC 370-21 and CSM.

3.6 Concluding remarks

The local buckling behaviour and resistances of hot-rolled stainless steel channel sections under pure compression have been studied, underpinned by testing and numerical modelling, and reported in this chapter. The testing programme, including material testing, membrane residual stress measurements, initial local geometric imperfection measurements and six stub column tests, was firstly conducted. The experimental programme was supplemented by a numerical modelling programme, where FE models were developed and validated against the test results and then used to perform parametric studies to generate further numerical data over a wide range of cross-section aspect ratios and dimensions. The obtained test and numerical data were employed to assess the relevant design rules, as set out in EN 1993-1-4 (CEN 2015) and ANSI/AISC 370-21 (AISC 2021). The assessment results revealed that (i) the codified slenderness limits in EN 1993-1-4 (CEN 2015) are accurate for outstand and

internal plate elements in compression and can be safely employed for the classification of hot-rolled stainless steel channel sections; (ii) EN 1993-1-4 (CEN 2015) and ANSI/AISC 370-21 (AISC 2021) result in conservative cross-section compression resistance predictions, due to the neglect of material strain hardening and plate element interaction and (iii) the CSM (Afshan and Gardner 2013; Zhao et al. 2017), allowing for rational consideration of material strain hardening and plate element interaction, leads to accurate and consistent resistance predictions of hot-rolled stainless steel channel section stub columns.

CHAPTER 4

LOCAL BUCKLING OF CHANNEL SECTIONS UNDER MAJOR-AXIS COMBINED LOADING

4.1 Introduction

This chapter reports an experimental and numerical investigation of the local buckling behaviour and cross-section resistance of hot-rolled stainless steel channel sections subjected to combined compression and major-axis bending. An experimental programme was firstly carried out and included initial local geometric imperfection measurements and ten eccentric compression tests. This was accompanied by a numerical modelling programme, where finite element models were developed to replicate the test observations and then used to perform parametric studies to generate additional numerical data over a wide range of cross-section dimensions and loading combinations. The test and numerical data were employed to assess the accuracy of the relevant design interaction curves, as given in the European code (CEN 2015) and the American specification (AISC 2021), followed by the development of new design interaction curves. The findings of this research have been reported by Li et al. (2022a).

4.2 Testing

4.2.1 General

In view of the fact that there have been no major-axis eccentric compression tests on hot-rolled stainless steel channel sections, an experimental programme was firstly performed. Plain channel sections with two different dimensions – C 80×40×5 and C 100×50×5, fabricated by hot-rolling from grade EN 1.4301 austenitic stainless steel sheets, were used and categorised as Class 2 and Class 3, respectively, according to the Eurocode slenderness limits (CEN 2015). For each of the two used channel sections, five stub column specimens with identical nominal member length were fabricated and later tested under major-axis eccentric compression at different initial loading eccentricities. The labelling system for each specimen comprised a letter ('A' representing C 80×40×5 and 'B' signifying C 100×50×5) and a special number. Table 4.1 reports the key measured geometric dimensions and initial local geometric imperfections of the ten hot-rolled stainless steel channel section stub column specimens. Note that the test setup and procedures used for initial local geometric imperfection measurements were the same as those detailed in Section 3.2.3, but with three LVDTs moving transversely along the flanges and web at a series of key cross-sections of each stub column specimen. Figure 4.1 displays the measured distribution of initial local geometric imperfections for a typical stub column specimen B2 at mid-height.

4.2.2 Eccentric compression tests

Major-axis eccentric compression tests were carried out on the hot-rolled stainless steel channel section stub column specimens to investigate their cross-section behaviour and resistance under major-axis combined loading. Various initial loading eccentricities to the cross-section major axis were applied for testing, leading to a wide range of combinations of bending and compression. Each stub column specimen

was compressed in an INSTRON 5000-kN universal testing machine under displacement control at a speed of 0.2 mm/min. As displayed in Figure 4.2, the knife-edge device consisted of a pit plate with a semi-circular groove and a wedge plate with a knife-edge wedge and was equipped at each end of the testing machine, in order to provide pin-ended boundary conditions to the specimen ends. Before testing, each specimen, welded with 15-mm-thick steel plates at its ends, was positioned between the knife-edge devices, with its position properly aligned and adjusted to achieve that (i) its longitudinal axis was perpendicular to the knife-edge devices and (ii) its cross-section major axis was parallel with the knife edges, with the distance being roughly the same as the pre-specified initial loading eccentricity.

Regarding the instrumentation adopted in the major-axis eccentric compression tests, as displayed in Figure 4.2, an LVDT, perpendicularly pointing to the flange at mid-height, was used for measuring the lateral deflections, while two strain gauges, stuck onto the exterior fibres of the flanges at mid-height in the longitudinal direction, were used for measuring the strains. The strain gauge and LVDT readings were used for calculation of the actual initial loading eccentricity for each specimen e_0, according to Equation (4.1) (Zhao et al. 2015, 2016a), where I_y is the major-axis second moment of area, ε_{max}-ε_{min} is the difference in strain measured from the two strain gauges, Δ is the lateral deflection at mid-height measured by the LVDT and N is the eccentric compression force. Note that the derivation of Equation (4.1) is based on the assumption of linear and elastic structural behaviour and the eccentric compression loads adopted in the calculation of e_0 were limited to 15% of the expected failure loads.

$$e_0 = \frac{EI_y(\varepsilon_{max} - \varepsilon_{min})}{NB_w} - \Delta \tag{4.1}$$

Table 4.1. Geometric dimensions and initial local geometric imperfections of hot-rolled stainless steel channel section stub column specimens.

Cross-section	Specimen ID	L (mm)	B_w (mm)	B_f (mm)	t (mm)	r (mm)	ω_{f1} (mm)	ω_{f2} (mm)	ω_w (mm)	ω_0 (mm)
C 80×40×5	A1	182.3	80.56	40.52	5.06	4.95	0.05	0.05	0.05	0.05
	A2	180.9	80.79	40.13	5.07	4.88	0.02	0.04	0.04	0.04
	A3	177.5	80.60	40.45	5.01	4.96	0.03	0.03	0.03	0.03
	A4	178.3	80.47	40.14	4.93	4.91	0.03	0.04	0.03	0.04
	A5	177.6	80.41	39.97	4.83	4.82	0.02	0.02	0.05	0.05
C 100×50×5	B1	225.0	98.75	49.54	4.85	4.87	0.03	0.01	0.01	0.03
	B2	223.0	98.98	49.76	5.02	4.95	0.04	0.02	0.01	0.04
	B3	224.0	98.98	49.77	5.07	5.01	0.05	0.05	0.03	0.05
	B4	223.0	98.99	49.63	5.07	4.98	0.03	0.02	0.01	0.03
	B5	223.6	98.92	49.60	4.99	4.89	0.03	0.02	0.02	0.03

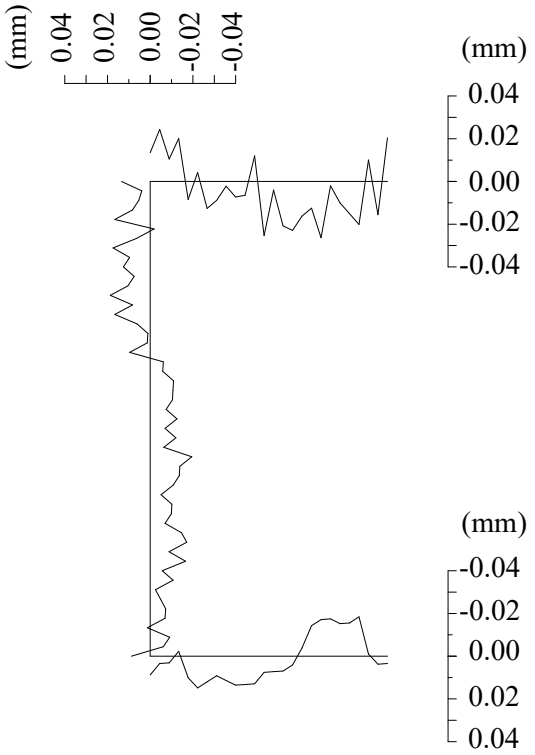

Figure 4.1. Measured distribution of initial local geometric imperfections for stub column specimen B2.

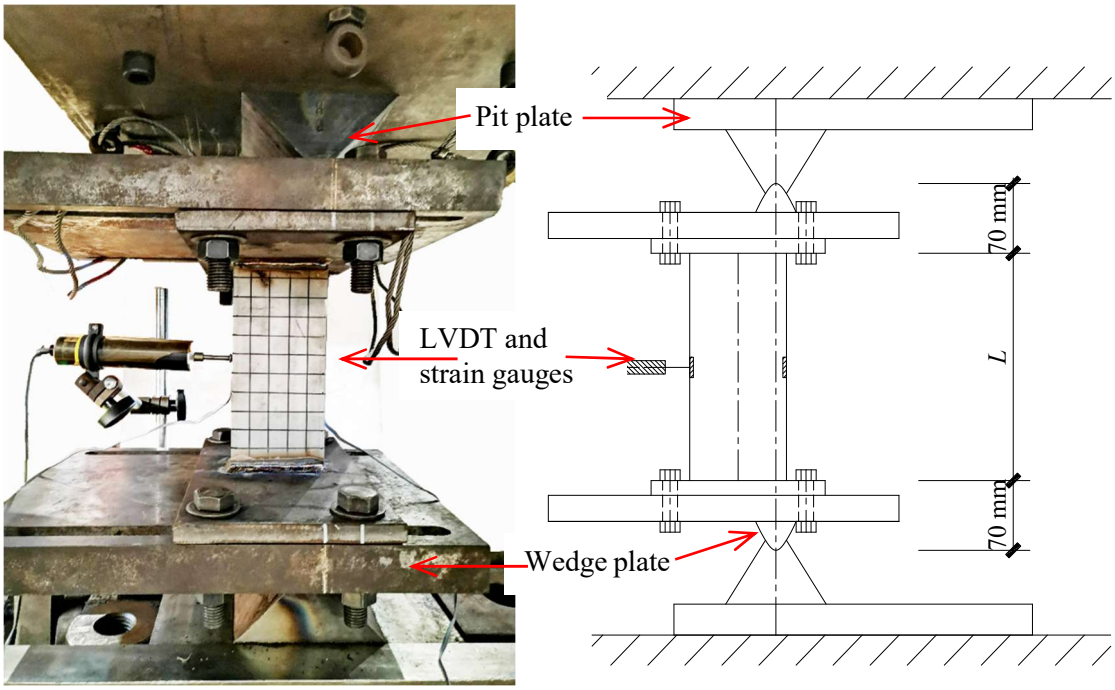

Figure 4.2. Major-axis eccentric compression test setup.

Table 4.2 reports the key experimental results, including the actual initial loading eccentricity e_0, the failure load $N_{u,test}$ and the corresponding mid-height lateral deflection Δ_u, and the failure moment $M_{u,test}=N_{u,test}(e_0+\Delta_u)$ at mid-height. The load–mid-height lateral deflection curves, as measured for the C 80×40×5 and C 100×50×5 specimens, are shown in Figure 4.3. Typical failure modes for specimens A5 and B2 are presented in Figure 4.4 and Figure 4.5, respectively, featuring visible deformation which is mainly localized at the compressive flange.

Table 4.2. Summary of major-axis eccentric compression test results.

Cross section	Specimen ID	e_0 (mm)	$N_{u,test}$ (kN)	Δ_u (mm)	$M_{u,test}$ (kNm)
C 80×40×5	A1	4.9	288.3	3.1	2.3
	A2	15.0	231.5	3.2	4.2
	A3	34.6	167.8	3.4	6.4
	A4	51.4	125.3	3.5	6.9
	A5	68.0	107.7	3.1	7.7
C 100×50×5	B1	10.4	276.9	1.9	3.4
	B2	24.7	242.5	2.2	6.5
	B3	38.6	210.3	2.2	8.6
	B4	60.4	161.4	1.7	10.0
	B5	98.7	119.8	1.9	12.1

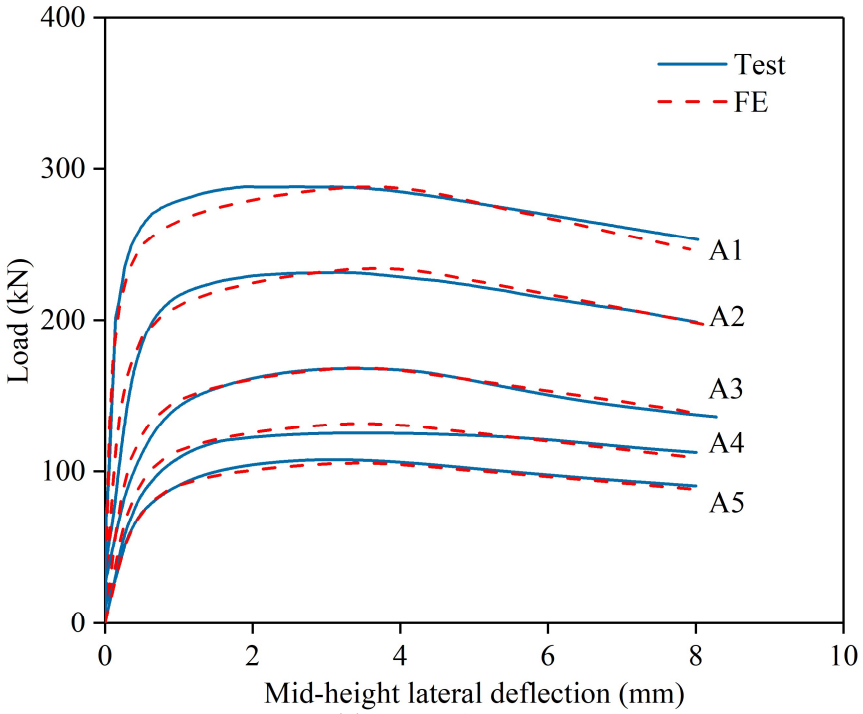

(a) C 80×40×5

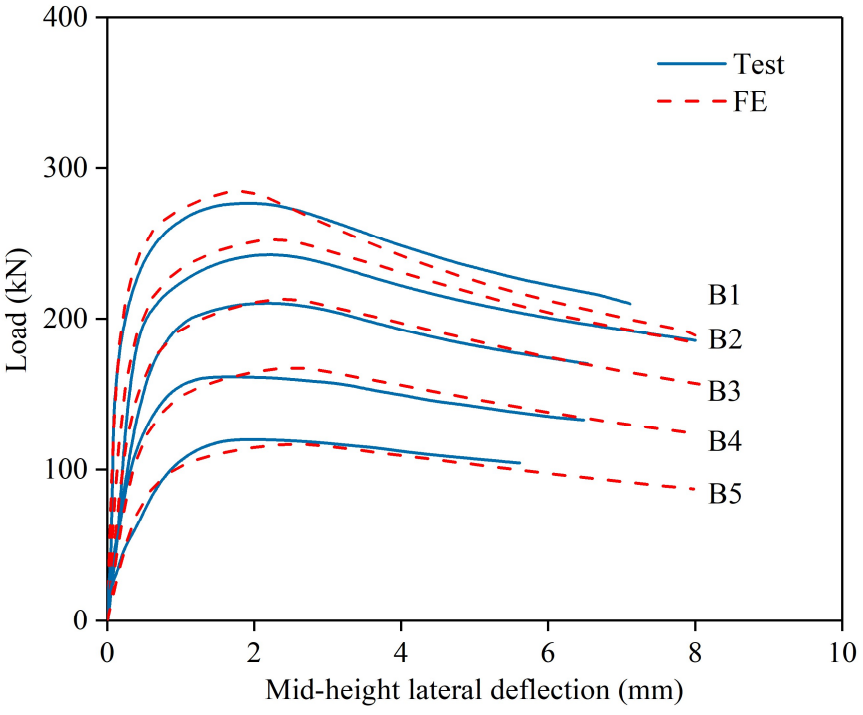

(b) C 100×50×5

Figure 4.3. Load–mid-height lateral deflection curves for stub column specimens.

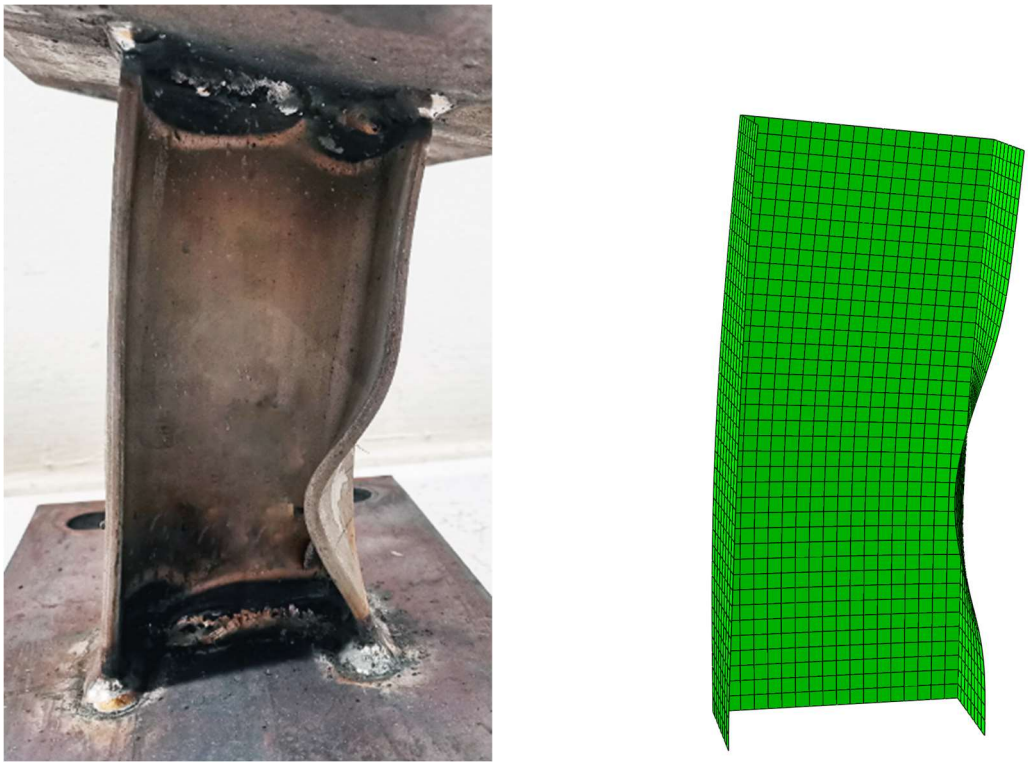

Figure 4.4. Test and FE failure modes for stub column specimen A5.

Figure 4.5. Test and FE failure modes for stub column specimen B2

4.3 Numerical modelling

4.3.1 General

In conjunction with the experimental programme, a numerical modelling programme was carried out through utilizing the finite element software ABAQUS (ABAQUS 2014). FE models were firstly developed, followed by validation against the test observations. Parametric studies were also conducted to generate additional numerical data.

4.3.2 Development and validation of FE models

For the development of FE models for hot-rolled stainless steel channel section stub columns under major-axis combined loading, the procedures and techniques of the selection of mesh sizes, modelling of material properties and incorporation of membrane residual stresses and initial local geometric imperfections were the same as the those described in Section 3.3.2. To facilitate the modelling of pin-ended boundary conditions, the end section of each stub column FE model was firstly coupled to an eccentric reference point, which was located to the cross-section major axis at a distance of e_0 and also longitudinally offset from the end section by 70 mm, with the aim of accurately reflecting the experimental setup, where the distance between the end cross section of specimen and the rotation centre of knife-edge device is 70 mm – see Figure 4.2. Subsequently, the reference point at the top was set to be free for longitudinal translation and major-axis rotation, while its counterpart at the bottom was only set to be free for major-axis rotation. Two local imperfection magnitudes, including the measured magnitude ω_0 and a generalised magnitude $t/100$, were used to scale the obtained initial local geometric imperfection distribution pattern. Finally, materially and geometrically nonlinear 'Riks' analysis (ABAQUS 2014) was performed to solve each stub column FE model to obtain the numerical failure load and mode as well as load–deformation history.

Validation of the developed stub column FE models was carried out through comparing the test against numerical results. Table 4.3 lists the ratios of the FE to test failure loads for all the specimens, demonstrating that both the measured and generalised imperfection values result in satisfactory agreement between the FE and test failure loads. The FE and test local buckling failure modes for representative specimens A5 and B2 are exhibited in Figure 4.4 and Figure 4.5, showing satisfactory agreement. Comparisons between the FE and test load–deformation histories for all the specimens are displayed in Figure 4.3, also showing good agreement. To summarise, the FE modes can replicate the test observations and were thus regarded as having been validated.

Table 4.3. Comparisons of numerical failure loads with test failure loads for varying initial local geometric imperfection magnitudes.

Cross section	Specimen ID	$N_{u,FE}/N_{u,test}$	
		ω_0	$t/100$
C 80×40×5	A1	1.00	1.00
	A2	1.01	1.01
	A3	1.00	1.00
	A4	1.05	1.05
	A5	0.98	0.98
C 100×50×5	B1	1.03	1.03
	B2	1.04	1.04
	B3	1.01	1.01
	B4	1.04	1.03
	B5	0.97	0.97
	Mean	1.01	1.01
	COV	0.03	0.03

4.3.3 Parametric studies

Upon validation, parametric studies were carried out using the developed stub column FE models, in order to generate additional numerical data over a wide range of cross-section dimensions and loading combinations. The used modelling techniques, procedures and assumptions were the same as those described in Section 4.3.2, but with the use of the measured material properties of C 80×40×5 and the generalised local imperfection magnitude of $t/100$. Regarding the modelled geometries, the outer

web widths were kept constant as 270 mm, while the outer flange widths ranged from 90 mm to 270 mm, with the wall thicknesses varied from 6.2 mm to 34.5 mm, leading to a wide range of cross-section dimensions; note that the modelled channel sections covered all four geometric classes (i.e. Class 1–4) of EN 1993-1-4 (CEN 2015). The length of each FE model was equal to three times the mean outer web and flange widths (Ziemian 2010). The adopted initial loading eccentricities ranged from 5 mm to 1000 mm. A total of 200 numerical data have been generated.

4.4 Assessment of existing international design standards

4.4.1 General

In the present section, the accuracy of the existing design interaction curves, as set out in EN 1993-1-4 (CEN 2015) and ANSI/AISC 370-21 (AISC 2013), for hot-rolled stainless steel channel sections under major-axis combined loading was assessed through comparing the experimental and numerical failure loads N_u with the unfactored failure load predictions $N_{u,pred}$. The shortcomings of the codified design interaction curves were analysed. Table 4.4 reports the quantitative assessment results, including the mean ratios $N_u/N_{u,pred}$ and the corresponding COVs for each of the codified design interaction curves.

Table 4.4. Comparisons of test and numerical failure loads with predicted failure loads from different design methods.

(a) EN 1993-1-4

Cross-section category	Number of tests	Number of FE simulations	$N_u/N_{u,EC3}$	
			Mean	COV
Class 1 and 2	5	100	1.34	0.05
Class 3	5	50	1.36	0.09
Class 4	0	50	1.36	0.05
Total	10	200	1.35	0.06

(b) ANSI/AISC 370-21

Cross-section category	Number of tests	Number of FE simulations	$N_u/N_{u,AISC}$	
			Mean	COV
Compact	0	30	1.29	0.05
Non-compact	10	80	1.30	0.04
Slender	0	90	1.31	0.09
Total	10	200	1.30	0.07

(c) New proposal

Cross-section category	Number of tests	Number of FE simulations	$N_u/N_{u,p}$	
			Mean	COV
$\bar{\lambda}_p \leq 0.60$	10	150	1.14	0.05
$\bar{\lambda}_p > 0.60$	0	50	1.31	0.05
Total	10	200	1.18	0.08

4.4.2 EN 1993-1-4

For stainless steel structural cross sections subjected to combined compression and bending, EN 1993-1-4 (CEN 2015) directly employs the corresponding design provisions prescribed in EN 1993-1-1 (CEN 2014) for their mild (carbon) steel counterparts. Specifically, a linear interaction curve is employed for the design of hot-rolled stainless steel channel sections under combined compression and major-axis bending, as defined by Equation (4.2),

$$\frac{N_{u,EC3}}{N_{EC3,Rd}} + \frac{M_{uy,EC3}}{M_{EC3,y,Rd}} \leq 1 \tag{4.2}$$

where $N_{u,EC3}$ and $M_{uy,EC3}=N_{u,EC3}(e_0+\Delta_u)$ are the design failure load and failure moment, respectively, while $N_{EC3,Rd}$ and $M_{EC3,y,Rd}$ are the EC3 cross-section resistances in pure compression and pure major-axis bending, respectively. The values of $N_{EC3,Rd}$ and $M_{EC3,y,Rd}$ are associated with the cross-section class defined in EN 1993-1-4 (CEN 2015). Specifically, for Class 1 or 2 cross sections, $M_{EC3,y,Rd}$ is taken as the plastic moment capacity $M_{pl,y}=W_{pl,y}\sigma_{0.2}$, where $W_{pl,y}$ denotes the plastic section modulus; for Class 3 cross sections, $M_{EC3,y,Rd}$ is taken as the elastic moment capacity $M_{el,y}=W_{el,y}\sigma_{0.2}$, where $W_{el,y}$ denotes the elastic section modulus; for Class 4 cross sections, $M_{EC3,Rd}$ is equal to the effective moment capacity $M_{eff,y}=W_{eff,y}\sigma_{0.2}$, where $W_{eff,y}$ denotes the

effective section modulus. With regard to $N_{EC3,Rd}$, the values are respectively calculated as the yield load $N_{pl}=A\sigma_{0.2}$ and effective compression capacity $N_{eff}=A_{eff}\sigma_{0.2}$ for Class 1–3 and Class 4 cross sections, where A and A_{eff} denote the gross and effective cross-section areas, respectively. Note that A_{eff} and $W_{eff,y}$ are calculated by the EC3 effective width method (CEN 2006b, 2015).

The accuracy of the EC3 design interaction curve was evaluated based on the obtained experimental and numerical data. Table 4.4 presents the mean test and numerical to predicted failure load ratios $N_u/N_{u,pred}$ and the corresponding COVs, showing that the EC3 design interaction curve results in conservative failure load predictions. The conservatism is also seen in Figure 4.6, where the EC3 design interaction curve falls well below the normalised test and numerical data points. The EC3 design interaction curve suffers from (i) the conservative compression and bending end points (i.e. $N_{EC3,Rd}$ and $M_{EC3,y,Rd}$) calculated at the 0.2% proof stress without considering material strain hardening and (ii) the inefficient linear shape taking no account of the beneficial stress redistribution within channel section.

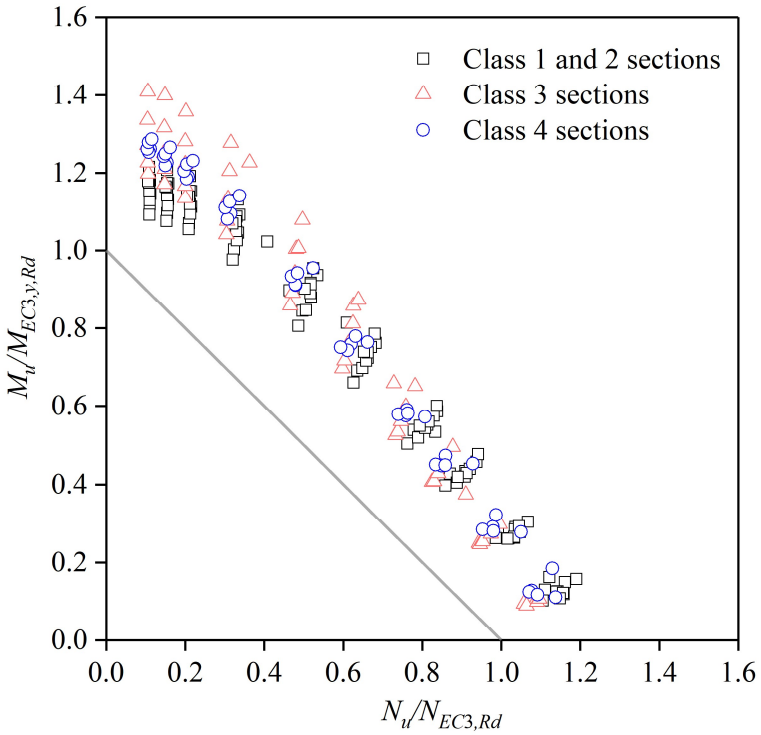

Figure 4.6. Test and FE data compared with EC3 design interaction curve.

4.4.3 ANSI/AISC 370-21

ANSI/AISC 370-21 (AISC 2021) specifies a bi-linear interaction curve for the design of hot-rolled stainless steel channel sections subjected to major-axis combined loading, as expressed by Equation (4.3), where $N_{u,AISC}$ and $M_{uy,AISC}=N_{u,AISC}(e_0+\Delta_u)$ are the design failure load and failure moment, respectively, and N_c and M_{cy} are the AISC cross-section resistances under pure compression and pure major-axis bending, respectively. The values of N_c and M_{cy} are also dependent upon the cross-section class (AISC 2021). Specifically, for compact cross sections, N_c is taken as the yield load $N_{pl}=A\sigma_{0.2}$ while M_{cy} is equal to the plastic moment capacity $M_{pl,y}=W_{pl,y}\sigma_{0.2}$; for non-compact cross sections, N_c is also equal to the yield load N_{pl}, while M_{cy} is determined with exploitation of partial plasticity and larger than the elastic moment capacity $M_{el,y}=W_{el,y}\sigma_{0.2}$; for slender cross sections, the effective cross-section geometric properties are utilized to replace the gross cross-section geometric properties for determining N_c and M_{cy}.

$$\begin{cases} \dfrac{N_{u,AISC}}{N_c}+\dfrac{8}{9}\dfrac{M_{uy,AISC}}{M_{cy}}\le 1 & \text{for } \dfrac{N_{u,AISC}}{N_c}\ge 0.2 \\ \dfrac{N_{u,AISC}}{2N_c}+\dfrac{M_{uy,AISC}}{M_{cy}}\le 1 & \text{for } \dfrac{N_{u,AISC}}{N_c}< 0.2 \end{cases} \tag{4.3}$$

The failure loads, predicted from the AISC design interaction curve, were assessed through comparing against those obtained from experiments and numerical modelling. The quantitative assessment results are reported in Table 4.4, while the graphical assessment results are presented in Figure 4.7. In general, the AISC design interaction curve was also found to yield conservative resistance predictions, owing to the conservative end points (N_c and M_{cy}), which are calculated without accounting for strain hardening, and the inefficient shape, which fails to capture stress redistribution within channel section.

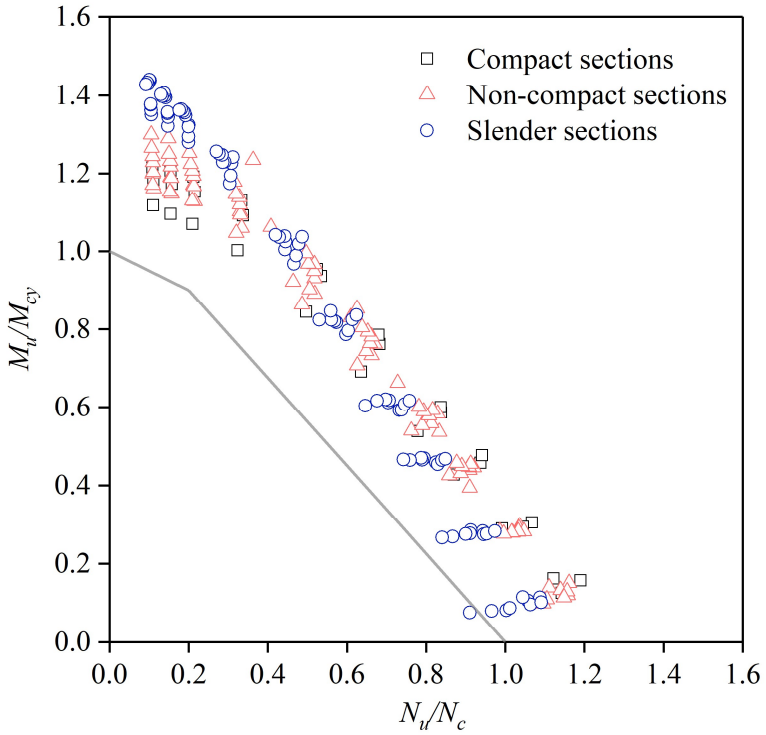

Figure 4.7. Test and FE data compared with AISC design interaction curve.

4.5 Development of new design method

To address the inaccuracy of the codified design interaction curves, new design interaction curves were developed using more accurate end points and more efficient shapes. The continuous strength method (Afshan and Gardner 2013; Zhao et al. 2017; Zhao and Gardner 2018) allows for proper consideration of material strain hardening and has been demonstrated to be able to accurately predict cross-section compression and bending resistances, which are hence ideal as the new end points.

The use of the CSM for the determination of cross-section resistance under pure compression has been described in Section 3.5 in detail. The CSM cross-section compression resistance $N_{csm,Rd}$ is equal to the product of the CSM design stress σ_{csm} and the gross cross-section area A, as defined by Equation (3.12). With regard to channel sections under major-axis bending, the CSM design strain ε_{csm} is calculated

using the CSM base curve of Equation (3.9). Then, the CSM design stress distribution is calculated based on the CSM bi-linear material model and given by Equation (3.11). Finally, the CSM cross-section bending resistance $M_{csm,y,Rd}$ is integrated from the CSM design stresses over the cross-section depth and then transformed into a simplified formulation, as given by Equation (4.4), where the coefficient α_{csm} is equal to 2.0 for channel section in major-axis bending (Zhao and Gardner 2018).

$$M_{csm,y,Rd} = \begin{cases} W_{el,y}\sigma_{0.2}\dfrac{\varepsilon_{csm}}{\varepsilon_y} & \text{for } \varepsilon_{csm} < \varepsilon_y \\ W_{pl,y}\sigma_{0.2}\left[1+\dfrac{E_{sh}}{E}\dfrac{W_{el,y}}{W_{pl,y}}\left(\dfrac{\varepsilon_{csm}}{\varepsilon_y}-1\right)-\left(1-\dfrac{W_{el,y}}{W_{pl,y}}\right)\Big/\left(\dfrac{\varepsilon_{csm}}{\varepsilon_y}\right)^{\alpha_{csm}}\right] & \text{for } \varepsilon_{csm} \geq \varepsilon_y \end{cases} \quad (4.4)$$

The experimental and numerical data are normalised by the CSM cross-section resistances and displayed in Figure 4.8. Based on the distribution of the normalised data points, a new bi-linear design interaction curve was proposed for hot-rolled stainless steel channel sections with $\bar{\lambda}_p \leq 0.6$, as defined by Equation (4.5), where $N_{u,p}$ and $M_{uy,p}=N_{u,p}(e_0+\Delta_u)$ are the design failure load and failure moment, respectively, and $a_w=(A-2tB_f)/A$ is the web-to-gross cross-section area ratio and no more than 0.5; note that the proposed bi-linear interaction curve herein is similar to that for I-sections under major-axis combined loading specified in EN 1993-1-4 (CEN 2015). Regarding hot-rolled stainless steel channel sections with $\bar{\lambda}_p > 0.6$, a linear design interaction curve was proposed, as given by Equation (4.6), in response to their elastic and linear structural behaviour. As can be seen in Figure 4.8, the proposed design interaction curves generally well capture the normalised test and numerical data points. The accuracy of the proposed design interaction curves was quantitatively assessed, with the results reported in Table 4.4, revealing that the proposed design interaction curves yield more accurate failure load predictions over their codified counterparts. The improved design accuracy is also seen in Figure 4.9 and Figure 4.10, where the cross-section resistances predicted by the proposed and codified design interaction curves are compared. It is worth noting that the proposed design interaction curves are based on and thus applicable to hot-rolled austenitic stainless steel channel sections subjected to major-axis combined loading, while their

applicability to other grades (e.g., ferritic and duplex) of stainless steel may need further investigations.

$$M_{uy,p} \le M_{csm,y,Rd} \frac{\left[1 - N_{u,p}/N_{csm,Rd}\right]}{\left(1 - 0.5a_w\right)} \quad \text{but } M_{uy,p} \le M_{csm,y,Rd} \quad \text{for } \overline{\lambda}_p \le 0.60 \tag{4.5}$$

$$\frac{N_{u,p}}{N_{csm,Rd}} + \frac{M_{uy,p}}{M_{csm,y,Rd}} \le 1 \qquad \text{for } \overline{\lambda}_p > 0.60 \tag{4.6}$$

The reliability of the developed new design interaction curves for hot-rolled stainless steel channel section stub columns under major-axis combined loading was assessed in accordance with EN 1990 (CEN 2002). In the present reliability analyses, the material over-strength ratio and the corresponding COV for austenitic stainless steel and the COV of the geometric dimensions of stainless steel sections were taken as the same as those in Section 3.5. The statistical parameters are reported in Table 4.5. It is concluded that the obtained partial safety factor is less than the current limit value of 1.1 in EN 1993-1-4 (CEN 2015) and the reliability of the proposed design interaction curves for hot-rolled stainless steel channel section stub columns under major-axis combined loading was thus confirmed.

Table 4.5. Reliability analysis results determined according to EN 1990.

No. of data	$k_{d,n}$	b	V_δ	V_r	γ_{M0}
210	3.14	1.13	0.07	0.10	0.94

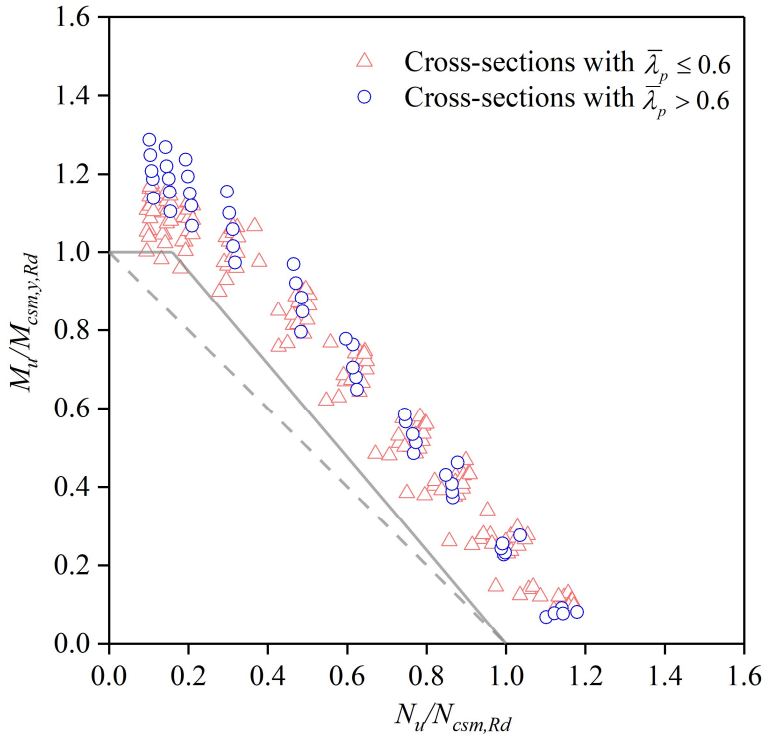

Figure 4.8. Test and FE data compared with proposed design interaction curves.

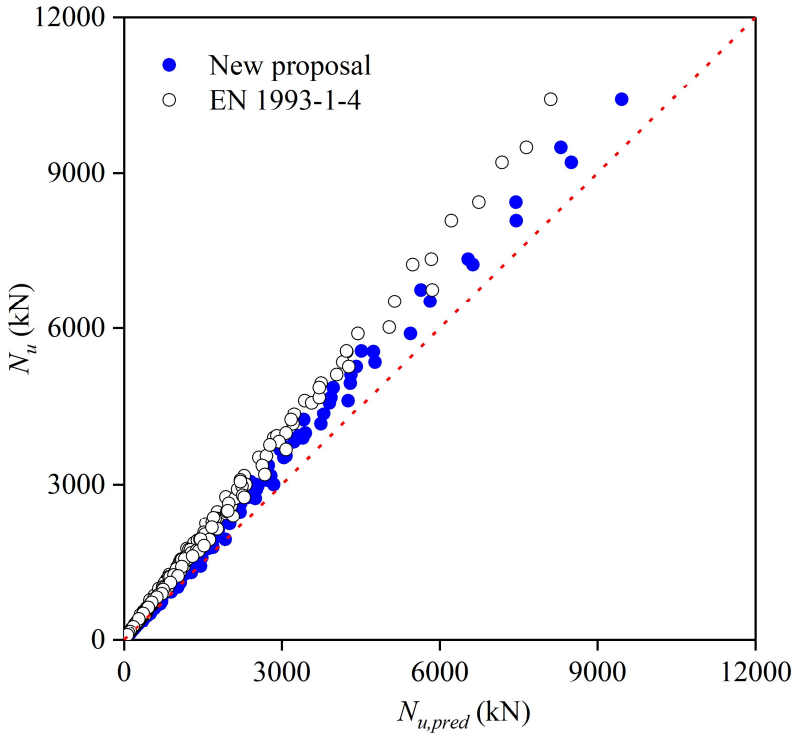

Figure 4.9. Test and FE failure loads compared with predictions from EC3 and proposed design interaction curves.

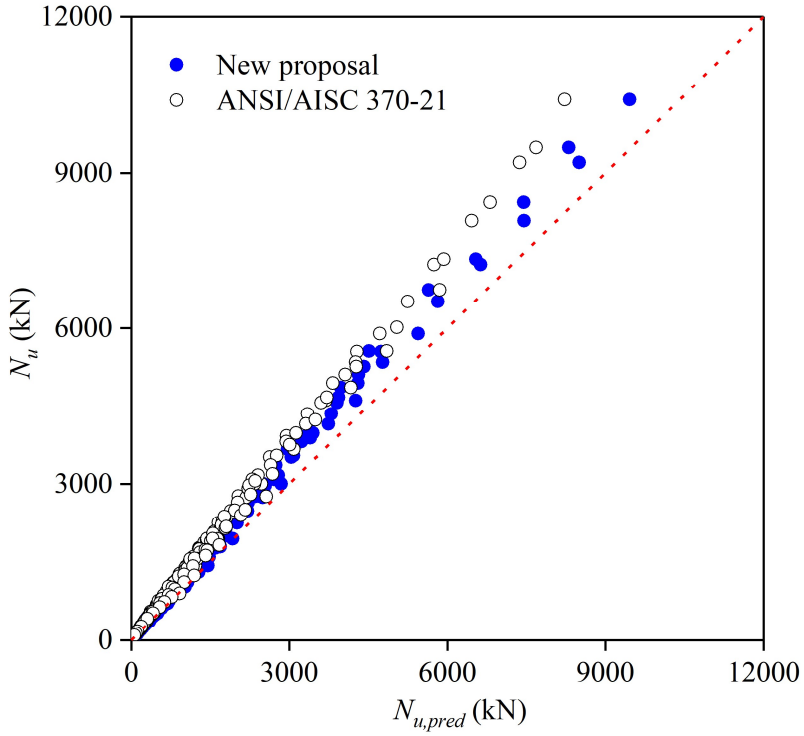

Figure 4.10. Test and FE failure loads compared with predictions from AISC and proposed design interaction curves.

4.6 Concluding remarks

An experimental and numerical modelling programme was carried out, to investigate the cross-section behaviour and resistance of hot-rolled stainless steel channel sections subjected to major-axis combined loading. The experimental programme included initial local geometric imperfection measurements and ten major-axis eccentric compression tests. The obtained experimental results were used in the numerical modelling programme to validate FE models, which were then employed to perform parametric studies to generate additional numerical data over a wide range of cross-section dimensions and loading combinations. The obtained test and numerical data were used to evaluate the accuracy of the design interaction curves, as set out in EN 1993-1-4 (CEN 2020) and ANSI/AISC 370-21 (AISC 2021). Both codified design interaction curves were shown to lead to conservative resistance predictions, owing mainly to conservative end points (calculated without considering

strain hardening) and inefficient shapes (cannot capture stress redistribution). New design interaction curves were developed through using more accurate CSM end points (calculated with proper exploitation of strain hardening of stainless steel) and more efficient shapes (properly capturing stress redistribution within channel section), and result in greatly improved design accuracy than the codified design interaction curves.

CHAPTER 5

LOCAL BUCKLING OF CHANNEL SECTIONS UNDER MINOR-AXIS COMBINED LOADING

5.1 Introduction

Experimental and numerical studies on the local buckling behaviour of hot-rolled stainless steel channel sections subjected to combined compression and minor-axis bending moment have been conducted and are fully reported in the present chapter. The testing programme included initial local geometric imperfection measurements and ten minor-axis eccentric compression tests. The numerical modelling programme included a validation study, where finite element models were developed and validated against the test results, and a series of parametric studies, where the developed finite element models were adopted to generate further numerical data over a wide range of cross-section dimensions and loading combinations. The experimentally and numerically obtained data were used to assess the accuracy of the design interaction curves for hot-rolled stainless steel channel sections under minor-axis combined loading, as given in the European code (CEN 2015) and American specification (AISC 2021). Finally, an improved design interaction curve was developed. The findings of this research have been presented by Li et al. (2022b).

5.2 Testing

5.2.1 General

Given that no tests on hot-rolled stainless steel channel sections under minor-axis combined loading have been reported to date, a testing programme was firstly conducted to obtain a test data bank. Ten channel section stub column specimens with the same size of cross-section C 100×50×5, hot-rolled from grade EN 1.4301 austenitic stainless steel sheets, were used in the testing. The channel section C 100×50×5 is defined as Class 3 based on the slenderness limits given in EN 1993-1-4 (CEN 2015). The nominal length of each stub column specimen was set equal to three times the mean outer cross-section dimensions according to the recommendations of Ziemian (2010). Prior to testing, the initial local geometric imperfections of each stub column specimen were measured, with the adopted test setup and procedures described in Section 3.2.3. Table 5.1 reports the measured geometric dimensions and initial local geometric imperfections of each hot-rolled stainless steel channel section stub column specimen

Table 5.1. Measured geometric dimensions and initial local geometric imperfections of hot-rolled stainless steel channel section stub column specimens.

Cross-section	Specimen ID	L (mm)	B_w (mm)	B_f (mm)	t (mm)	r (mm)	ω_{f1} (mm)	ω_{f2} (mm)	ω_w (mm)	ω_0 (mm)
100×50×5	C1	225.2	98.93	49.65	4.82	4.91	0.02	0.03	0.02	0.03
	C2	222.9	98.99	49.62	4.79	4.85	0.04	0.01	0.04	0.04
	C3	223.5	99.17	49.61	4.78	4.87	0.04	0.03	0.01	0.04
	C4	223.8	98.95	49.75	4.77	4.90	0.02	0.04	0.03	0.04
	C5	223.0	98.97	49.61	4.73	4.63	0.02	0.01	0.04	0.04
	RC1	223.5	99.05	49.74	4.86	4.77	0.03	0.02	0.03	0.03
	RC2	223.8	99.01	50.27	4.79	4.94	0.04	0.03	0.01	0.04
	RC3	223.7	98.97	49.59	4.75	4.85	0.01	0.03	0.02	0.03
	RC4	223.2	98.91	49.79	4.71	4.66	0.01	0.04	0.01	0.04
	RC5	221.6	98.91	49.65	4.76	4.64	0.03	0.02	0.03	0.03

5.2.2 Eccentric compression tests

Eccentric compression tests were conducted on the ten hot-rolled stainless steel channel section stub column specimens to investigate their cross-sectional behaviour and resistances under combined compression and minor-axis bending moment. For five specimens, the eccentric compression loads were applied between the cross-section elastic neutral axis and flange tips; the resulting end moments induced the maximum compressive stresses at the flange tips, with the specimens deflecting towards the web (i.e. in the 'C' orientation). For the other five specimens, the eccentric compression loads were applied between the cross-section elastic neutral axis and web; the resulting end moments induced the maximum compressive stresses in the web, with the specimens deflecting towards the flange tips (i.e. in the 'reverse C' orientation).

All the eccentric compression tests were conducted by using an INSTRON 5000 kN hydraulic testing machine at a constant rate of 0.2 mm/min. Each end of the testing machine was equipped with a knife-edge device, offering pin-ended boundary conditions to the specimen ends about the minor principal axis. The knife-edge device, as shown in Figure 5.1, consists of a pit plate with a semi-circular groove and a wedge plate with a knife-edge wedge. Prior to testing, each stub column specimen, welded with 20-mm-thick end plates, was placed between the top and bottom wedge plates, and their relative position was carefully adjusted to ensure that (i) the member longitudinal axis of the stub column specimen was perpendicular to the wedge plates and (ii) the cross-section minor principal axis was parallel to the knife edges, with the distance equal to the pre-specified initial loading eccentricity. Upon completion of the position adjustment, the stub column specimen was anchored by bolting the welded end plates to the wedge plates.

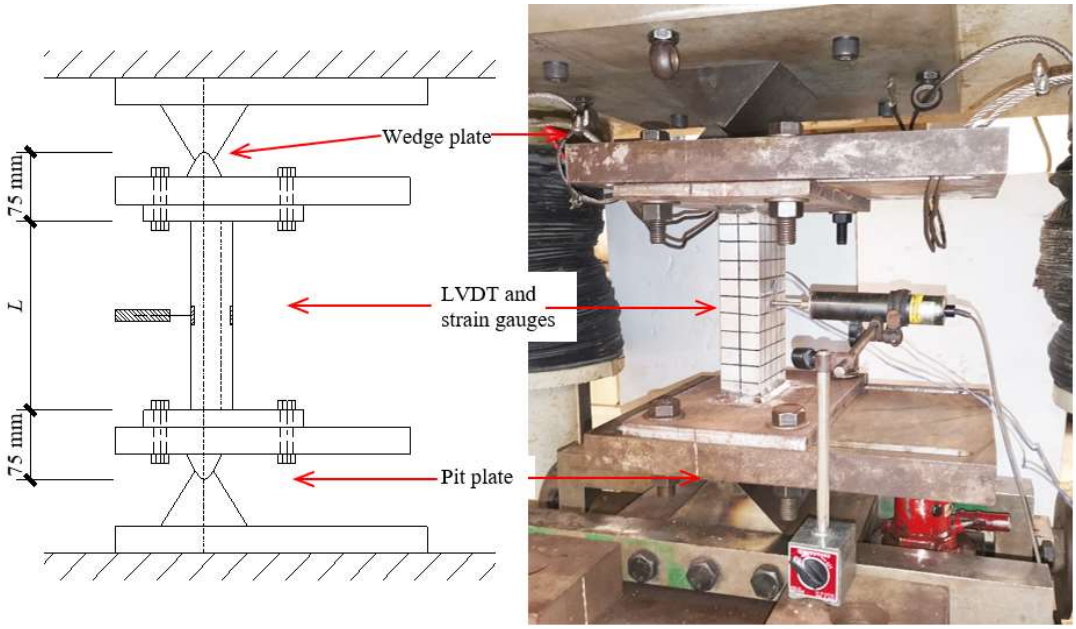

Figure 5.1. Setup for minor-axis eccentric compression tests

Figure 5.1 displays a photograph and a schematic diagram of the eccentric compression test setup, where an LVDT is attached to the web of the specimen at mid-height to record the lateral deflections about the minor principal axis and two strain gauges are affixed to the outer faces of the web and flange tip of the specimen at mid-height to measure the longitudinal strains at these locations. The readings of the LVDT and two strain gauges were used to derive the actual initial loading eccentricity e_0 of each eccentrically loaded stub column specimen to the elastic neutral axis, according to Equation (5.1) (Zhao et al. 2015, 2016a), where ε_{max}-ε_{min} is the difference of the longitudinal strains measured from the two strain gauges, Δ is the mid-height lateral deflection about the minor principal axis recorded by the LVDT, I_z is the second moment of area about the minor principal axis and N is the applied compression load. Note that Equation (5.1) was derived based on the assumption of linear elastic structural behaviour and it was thus recommended that no more than 15% of the expected failure load be used in the calculation of e_0.

$$e_0 = \frac{EI_z(\varepsilon_{max} - \varepsilon_{min})}{NB_f} - \Delta \tag{5.1}$$

For each hot-rolled stainless steel channel section stub column specimen under minor-axis combined loading, the key test results, including the failure orientation, the actual initial loading eccentricity e_0, the failure load $N_{u,test}$, the mid-height lateral deflection at the failure load Δ_u and the failure moment $M_{u,test}=N_{u,test}(e_0+\Delta_u)$ at the specimen mid-height, were measured and are presented in Table 5.2. It is concluded that hot-rolled stainless steel channel section stub columns failing in the 'C' orientation generally have lower cross-section compression resistances than their counterparts failing in the 'reverse C' orientation, and 'C' orientation failure is thus more critical. Upon testing, the specimens C1–C5 (where the eccentric compression loads were applied between the cross-section elastic neutral axis and flange tips) exhibited deformation and failure about the minor principal axis in the 'C' orientation, as illustrated in Figure 5.2, while the specimens RC1–RC5 (where the eccentric compression loads were applied between the cross-section elastic neutral axis and web) featured deformation and failure about the minor principal axis in the 'reverse C' orientation, as shown in Figure 5.3. The load–mid-height lateral deflection curves measured for the two series of hot-rolled stainless steel channel section stub column specimens failing in the 'C' and 'reverse C' orientations are presented in Figure 5.4(a) and Figure 5.4(b), respectively.

Table 5.2. Summary of minor-axis eccentric compression test results.

Cross section	Specimen ID	Failure orientation	e_0 (mm)	$N_{u,test}$ (kN)	Δ_u (mm)	$M_{u,test}$ (kNm)
C 100×50×5	C1	C	5.1	194.0	2.6	1.5
	C2	C	9.7	151.2	3.5	2.0
	C3	C	18.4	114.2	6.4	2.8
	C4	C	29.6	87.2	7.3	3.2
	C5	C	59.8	49.9	11.1	3.5
	RC1	reverse C	5.7	276.0	5.0	2.9
	RC2	reverse C	8.5	262.2	4.8	3.5
	RC3	reverse C	19.8	173.0	4.7	4.2
	RC4	reverse C	31.5	125.5	5.3	4.6
	RC5	reverse C	60.3	72.7	6.8	4.9

Figure 5.2. Experimental and numerical failure modes for specimen C5 failing in the ‘C’ orientation.

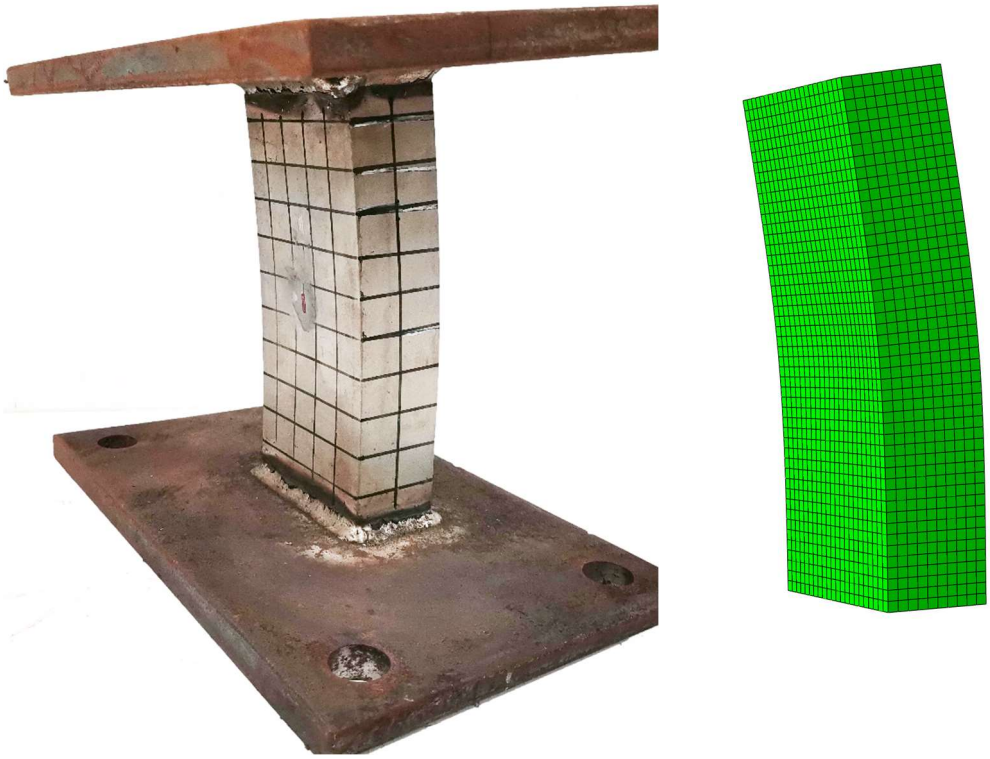

Figure 5.3. Experimental and numerical failure modes for specimen RC4 failing in the ‘reverse C’ orientation.

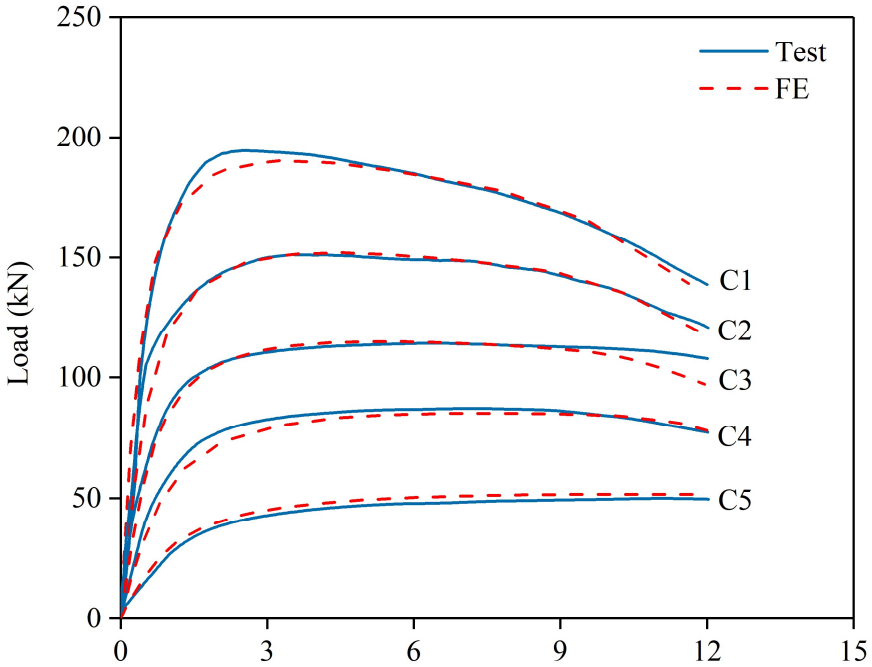

(a) In the 'C' orientation

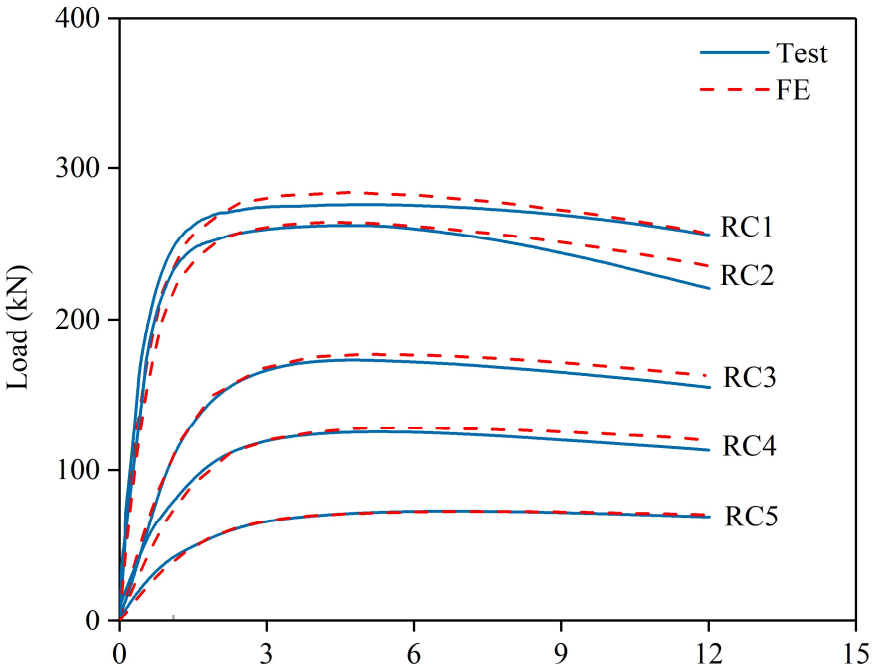

(b) In the 'reverse C' orientation

Figure 5.4. Experimental and numerical load–mid-height lateral deflection curves.

5.3 Numerical modelling

5.3.1 General

Following the testing programme, a numerical modelling programme was conducted using the nonlinear finite element software ABAQUS (ABAQUS 2014). The numerical modelling programme comprised a validation study, where FE models were developed and validated against the test results, and a series of parametric studies, where the developed FE models were adopted to generate further numerical data over a wide range of cross-section dimensions and loading combinations.

5.3.2 Development and validation of FE models

The same modelling assumptions, procedures and techniques, as those described in Section 3.3.2, were employed herein to develop the FE models of hot-rolled stainless steel channel section stub columns under minor-axis combined loading. For ease of application of boundary conditions, each end section of the FE model was firstly coupled to a reference point, which was located eccentrically to the cross-section minor principal axis, with the eccentricity equal to the corresponding actual initial loading eccentricity e_0, and also offset longitudinally from the end section by 75 mm – the distance from the specimen end to the rotation centre of the knife-edge device in the tests (see Figure 5.1). Then, one reference point was allowed to translate along the longitudinal axis and rotate about the cross-section minor principal axis, while the other reference point was only allowed to rotate about the same axis. Regarding the incorporation of initial local geometric imperfections, two local imperfection magnitudes, including the measured value ω_0 and a generalised value $t/100$, were used to scale the derived initial local geometric imperfection pattern. Finally, static Riks analyses (ABAQUS 2014) were conducted on the developed FE models to derive the numerical failure loads, load–mid-height lateral deflection curves and failure modes.

The numerically derived results were compared against their experimental counterparts, allowing the accuracy of the developed FE models to be assessed. Table 5.3 reports the ratios of the numerical to test failure loads for all the ten eccentrically loaded hot-rolled stainless steel channel section stub column specimens, with the results generally revealing that both the measured and generalised local imperfection magnitudes lead to accurate and consistent predictions of the test failure loads. Comparisons between the test and numerical failure modes for two typical specimens C5 and RC4 with failure in the 'C' and 'reverse C' orientations are respectively presented in Figure 5.2 and Figure 5.3, indicating good agreement. The test and numerical load–mid-height lateral deflection curves for the two series of eccentrically loaded hot-rolled stainless steel channel section stub column specimens failing in the 'C' and 'reverse C' orientations are displayed in Figure 5.4(a) and Figure 5.4(b), respectively, where the test curves are well replicated by their numerical counterparts. It can thus be concluded that the developed FE models are capable of simulating the eccentric compression tests on hot-rolled stainless steel channel section stub columns and deemed to be validated.

Table 5.3. Comparisons of FE failure loads with test failure loads for different initial local geometric imperfection magnitudes.

Cross section	Specimen ID	$N_{u,FE}/N_{u,test}$	
		ω_0	$t/100$
C 100×50×5	C1	0.98	0.98
	C2	1.01	1.01
	C3	1.01	1.01
	C4	0.98	0.98
	C5	1.03	1.03
	RC1	1.03	1.03
	RC2	1.01	1.01
	RC3	1.02	1.02
	RC4	1.02	1.02
	RC5	1.00	1.00
	Mean	1.01	1.01
	COV	0.02	0.02

5.3.3 Parametric studies

Having been validated in Section 5.3.2, the developed FE models were employed to conduct parametric studies to expand the test data pool over a wider range of cross-section dimensions and loading combinations. The modelling assumptions, procedures and techniques used herein were the same as those described in Section 5.3.2, but with the initial local geometric imperfection magnitude now fixed at t/100. With regard to the cross-section geometric dimensions of the modelled channel sections, the outer web widths were fixed at 180 mm and the outer flange widths were varied between 60 mm and 180 mm, with the wall thicknesses set to be equal and ranging from 6.5 mm to 23 mm, which led to a wide range of cross-section aspect ratios and dimensions being considered. It is worth noting that the modelled channel sections cover Class 1, 2 and 3 cross-sections according to the slenderness limits set out in EN 1993-1-4 (CEN 2015) and also fall in the category of compact and non-compact cross-sections according to the slenderness limits given in ANSI/AISC 370-21 (AISC 2021). The length of each FE model was set to be equal to three times the mean outer cross-section dimensions. The initial loading eccentricities at both sides of the cross-section minor principal axis were varied between 1 mm and 1024 mm, leading to a wide range of loading combinations and failure in both the 'C' and 'reverse C' orientations being considered. Finally, a total of 300 numerical data on hot-rolled stainless steel channel sections under minor-axis combined loading have been generated through the present parametric studies, with 185 for the 'C'-orientation failure cases and 115 for the 'reverse C'-orientation failure cases.

5.4 Assessment of existing international design standards

5.4.1 General

The design interaction curves for hot-rolled stainless steel channel sections under combined compression and minor-axis bending moment, as prescribed in EN 1993-

1-4 (CEN 2015) and ANSI/AISC 370-21 (AISC 2021), were described and discussed. The accuracy of each design interaction curve was assessed by comparing the test and numerical failure loads N_u against the unfactored design failure loads $N_{u,pred}$. Table 5.4 reports the quantitative assessment results, including the mean test and numerical to predicted failure load ratios $N_u/N_{u,pred}$ and the corresponding COVs.

Table 5.4. Comparisons of test and numerical failure loads with predicted failure loads from different design methods.

Failure orientation	No. of data		$N_u/N_{u,EC3}$		$N_u/N_{u,AISC}$		$N_u/N_{u,p}$	
	Test	FE	Mean	COV	Mean	COV	Mean	COV
C	5	185	1.59	0.17	1.36	0.16	1.18	0.09
reverse C	5	115	1.71	0.35	1.46	0.15	1.22	0.11
Total	10	300	1.64	0.26	1.40	0.16	1.20	0.10

5.4.2 EN 1993-1-4

For the design of hot-rolled stainless steel channel sections under minor-axis combined loading, a linear interaction curve is prescribed in EN 1993-1-4 (CEN 2015), as given by Equation (5.2), where $N_{u,EC3}$ is the design failure load, $M_{uz,EC3}= N_{u,EC3}(e_0+\Delta_u)$ is the design failure moment about the minor principal axis, in which e_0 is the initial loading eccentricity to the design neutral axis at failure, $N_{EC3,Rd}$ is the EC3 cross-section resistance under pure compression and $M_{EC3,z,Rd}$ is the EC3 cross-section resistance under pure bending about the minor principal axis. It is noteworthy that the values of e_0 and $M_{EC3,z,Rd}$ depend on the cross-section class. Specifically, for Class 1 and 2 channel sections, where the design neutral axis at failure is assumed to be located at the cross-section plastic neutral axis, e_0 is taken as the distance from the loading point to the cross-section plastic neutral axis e_{0p} and $M_{EC3,z,Rd}$ is equal to the plastic moment capacity $M_{pl,z}=W_{pl,z}\sigma_{0.2}$, in which $W_{pl,z}$ is the plastic section modulus; for Class 3 channel sections, where the design neutral axis at failure is assumed to be located at the cross-section elastic neutral axis, e_0 is taken as the distance from the loading point to the cross-section elastic neutral axis e_{0e} and $M_{EC3,z,Rd}$ reduces to the elastic moment capacity $M_{el,z}=W_{el,z}\sigma_{0.2}$, in which $W_{el,z}$ is the elastic section modulus.

$N_{EC3,Rd}$ is taken as the cross-section yield load $N_{pl}=A\sigma_{0.2}$ for non-slender (Class 1, 2 and 3) channel sections.

$$\frac{N_{u,EC3}}{N_{EC3,Rd}}+\frac{M_{uz,EC3}}{M_{EC3,z,Rd}}\leq 1 \tag{5.2}$$

The EC3 design interaction curve for hot-rolled stainless steel channel sections under minor-axis combined loading was evaluated against the test and numerical data. Figure 5.5 displays the graphical evaluation results, where the test and numerical data points, normalised by the EC3 cross-section compression and bending resistances, are compared with the EC3 design interaction curve. It can be seen that the EC3 design interaction curve lies well below the scattered test and numerical data points, indicating excessive conservatism and scatter. This is also evident in Table 5.4, where the mean test and numerical to EC3 predicted failure load ratio $N_u/N_{u,pred}$ is equal to 1.64, with the corresponding COV of 0.26, for eccentrically loaded hot-rolled stainless steel channel section stub columns. The high degree of conservatism and scatter of the EC3 failure load predictions mainly results from the conservative end points of the EC3 design interaction curve (i.e. the cross-section resistances under pure compression and pure bending), which are calculated based on the material 0.2% proof stress without considering material strain hardening of stainless steel.

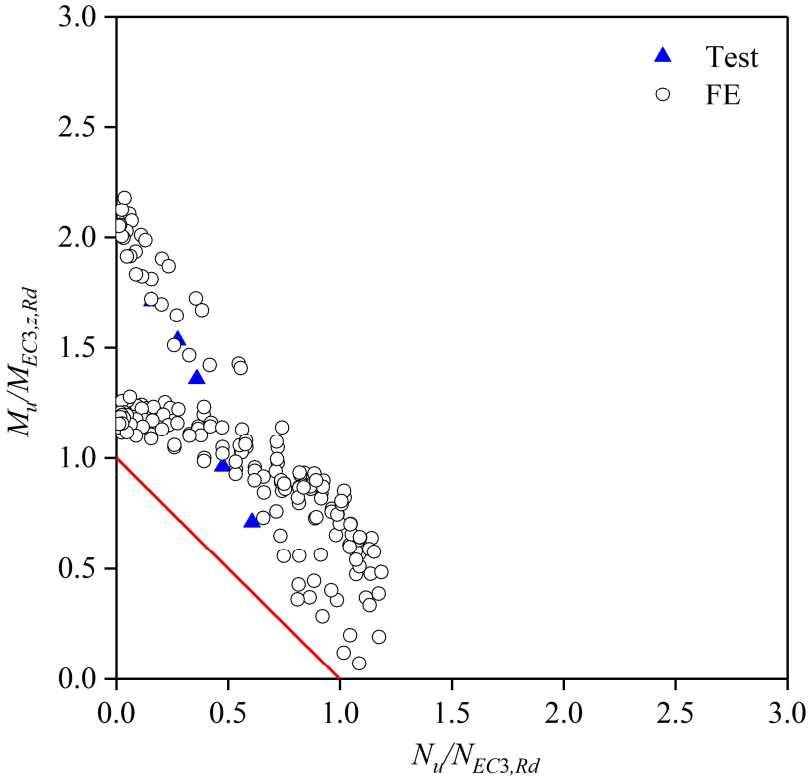

(a) In the 'C' orientation

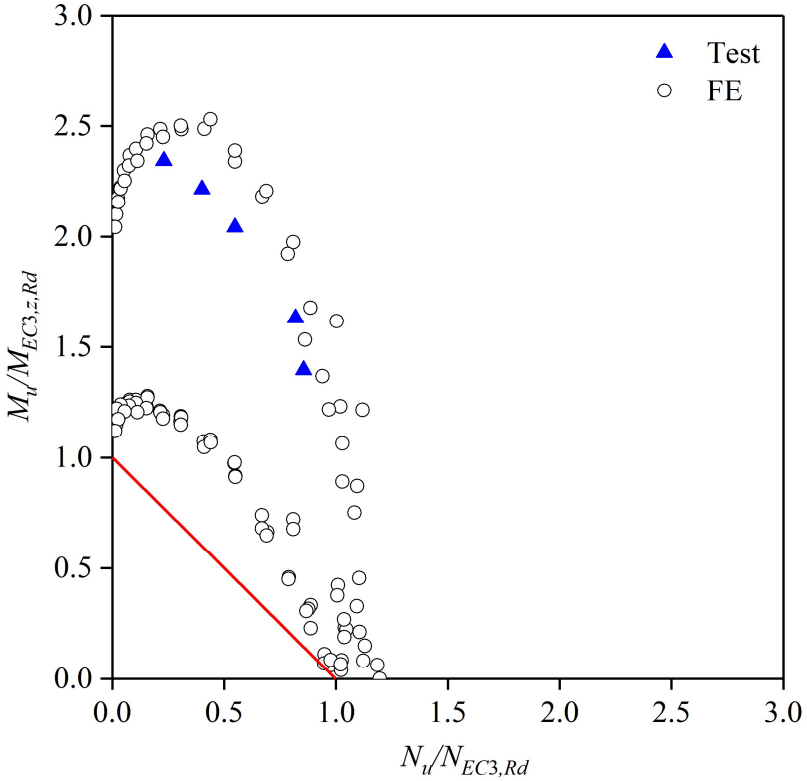

(b) In the 'reverse C' orientation

Figure 5.5. Comparisons of test and FE data against EC3 design interaction curve.

5.4.3 ANSI/AISC 370-21

ANSI/AISC 370-21 (AISC 2021) provides a bi-linear interaction curve for the design of hot-rolled stainless steel channel sections under minor-axis combined loading, as defined by Equation (5.3), where $N_{u,AISC}$ is the design failure load, $M_{uz,AISC}=N_{u,AISC}(e_0+\Delta_u)$ is the design failure moment about the minor principal axis; note that e_0 is taken as e_{0p} for compact channel sections but e_{0e} for non-compact channel sections, $N_c=A\sigma_{0.2}$ is the AISC cross-section compression resistance, and M_{cz} is the AISC cross-section minor-axis bending moment resistance, which is taken as the plastic moment capacity $M_{pl,z}=W_{pl,z}\sigma_{0.2}$ for compact channel sections and calculated with the consideration of partial plasticity for non-compact channel sections.

$$\begin{cases} \dfrac{N_{u,AISC}}{N_c}+\dfrac{8}{9}\dfrac{M_{uz,AISC}}{M_{cz}}\le 1 & \text{for } \dfrac{N_{u,AISC}}{N_c}\ge 0.2 \\ \dfrac{N_{u,AISC}}{2N_c}+\dfrac{M_{uz,AISC}}{M_{cz}}\le 1 & \text{for } \dfrac{N_{u,AISC}}{N_c}< 0.2 \end{cases} \tag{5.3}$$

The design failure loads, as determined from the AISC interaction curve for hot-rolled stainless steel channel sections under minor-axis combined loading, were compared with the corresponding test and numerical failure loads. As reported in Table 5.4, the mean test and numerical to AISC predicted failure load ratio $N_u/N_{u,AISC}$ is equal to 1.40, with the corresponding COV of 0.16, while the graphical comparison results are shown in Figure 5.6. Both the quantitative and graphical comparisons indicated that the AISC design interaction curve leads to conservative and scattered failure load predictions. This can be attributed to the conservative end points of the AISC design interaction curve, which are determined based on the 0.2% proof stress without considering material strain hardening. It is also worth noting that the AISC interaction curve results in a higher level of design accuracy and consistency than its EC3 counterpart, owing to the more efficient bi-linear shape and more accurate bending end point (determined with the consideration of partial plasticity for non-compact channel sections).

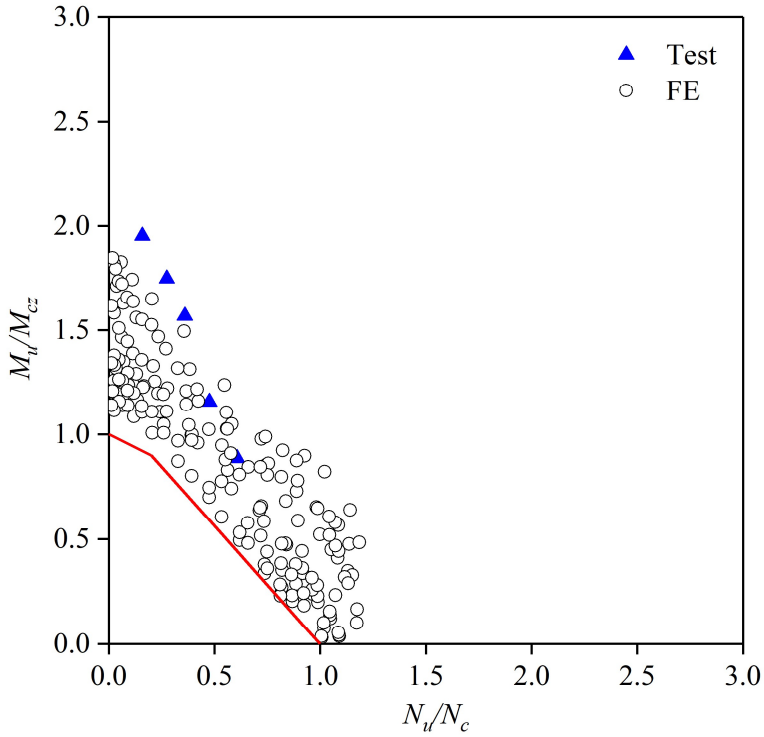

(a) In the 'C' orientation

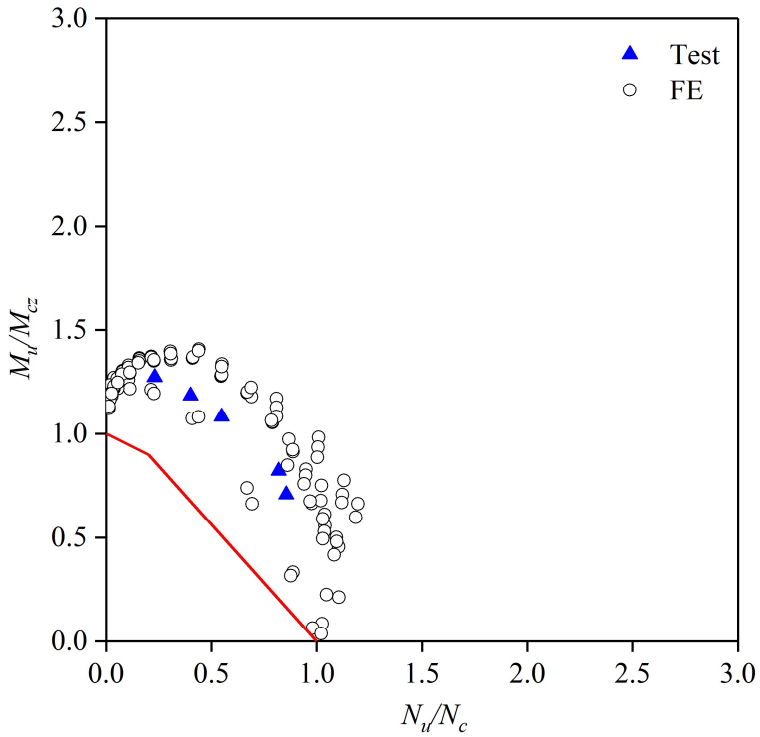

(b) In the 'reverse C' orientation

Figure 5.6. Comparisons of test and FE data against AISC design interaction curve.

5.5 Development of new design method

On the basis of the quantitative and graphical assessment results, the codified design interaction curves suffer from the conservative compression and bending end points, which are calculated without considering material strain hardening. Therefore, a new improved design interaction curve can be sought through the adoption of more accurate end points.

The continuous strength method (Afshan and Gardner 2013; Zhao et al. 2017; Zhao and Gardner 2018) is an advanced deformation-based design method, which allows for proper consideration of material strain hardening in determining cross-section resistances under isolated loading. The CSM had been shown to result in accurate and consistent compression and bending resistances of stainless steel channel sections (Zhao and Gardner 2018; Zhang et al. 2020a; Lan et al. 2021;) and the CSM cross-section compression and bending resistances are ideal end points for the new improved design interaction curve. The use of the CSM for the calculation of cross-section resistances under pure compression has been described in Section 3.5 and the CSM cross-section compression resistance $N_{csm,Rd}$ is given by Equation (3.12). With regard to the design of channel sections under minor-axis bending, the maximum tensile and compressive strains are not equal since the neutral axis is not located at the mid-point of the flange. The limiting compressive strain ε_{csm} is calculated from the CSM base curve of Equation (3.9), while the limiting tensile strain $\varepsilon_{csm,t}$ is determined based on linearly-varying through-depth strain distribution by Equation (5.4), where y_c is the distance from the maximum compressive fibre to the design neutral axis, which is assumed to be located at the mid-point between the cross-section elastic neutral axis and plastic neutral axis for channel sections with $\bar{\lambda}_p \leq 0.6$ but at the cross-section elastic neutral axis for channel sections with $\bar{\lambda}_p > 0.6$ (Zhao and Gardner 2018). The CSM cross-section bending resistance $M_{csm,z,Rd}$ is then calculated by Equation (5.5), where $\varepsilon_{csm,d}$ is the maximum of ε_{csm} and $\varepsilon_{csm,t}$ and α_{csm} is the CSM bending parameter and taken as 1.5 and 1.0 for channel sections with cross-section aspect ratios less and greater than 2.0, respectively (Zhao and Gardner 2018).

$$\varepsilon_{csm,t} = \frac{\varepsilon_{csm}\left(B_f - y_c\right)}{y_c} \tag{5.4}$$

$$M_{csm,z,Rd} = \begin{cases} W_{el,z}\sigma_{0.2}\dfrac{\varepsilon_{csm,d}}{\varepsilon_y} & \text{for } \varepsilon_{csm,d} < \varepsilon_y \\ W_{pl,z}\sigma_{0.2}\left[1+\dfrac{E_{sh}}{E}\dfrac{W_{el,z}}{W_{pl,z}}\left(\dfrac{\varepsilon_{csm,d}}{\varepsilon_y}-1\right)-\left(1-\dfrac{W_{el,z}}{W_{pl,z}}\right)\Big/\left(\dfrac{\varepsilon_{csm,d}}{\varepsilon_y}\right)^{\alpha_{csm}}\right] & \text{for } \varepsilon_{csm,d} \geq \varepsilon_y \end{cases} \tag{5.5}$$

The test and numerical data were normalised by the CSM cross-section compression and bending resistances ($N_{csm,Rd}$ and $M_{csm,z,Rd}$) and displayed in Figure 5.7. Since 'C'-orientation failure is more critical, a linear design interaction curve, anchored to the CSM end points, was developed based on the distribution pattern of hot-rolled stainless steel channel section stub columns failing in the 'C' orientation in Figure 5.7(a) and given by Equation (5.6), where $N_{u,p}$ and $M_{uz,p}=N_{u,p}(e_0+\Delta_u)$ are the design failure load and failure moment, respectively, where e_0 is the initial loading eccentricity to the CSM design neutral axis. As shown in Figure 5.7(a), the proposed design interaction curve follows closely the data points. The accuracy of the proposed design interaction curve for hot-rolled stainless steel channel section stub columns failing in the 'C' and 'reverse C' orientations was assessed, with the results reported in Figure 5.7 and Table 5.4. Overall, the new design interaction curve offers improved design accuracy and consistency than the codified design interaction curves; this is also evident in Figure 5.8 and Figure 5.9, where failure load predictions calculated by the codified and proposed design interaction curves are compared. Note that the developed design interaction curve is based on and thus applicable to hot-rolled austenitic stainless steel channel sections under minor-axis combined loading, while its applicability to other grades (e.g., ferritic and duplex) of stainless steel may need further investigations.

$$\frac{N_{u,p}}{N_{csm,Rd}} + \frac{M_{uz,p}}{M_{csm,z,Rd}} \leq 1 \tag{5.6}$$

The reliability of the new design interaction curve for hot-rolled stainless steel channel section stub columns under minor-axis combined loading was assessed in

accordance with EN 1990 (CEN 2002). In the present reliability analyses, the material over-strength ratio and the corresponding COV for austenitic stainless steel and the COV of the geometric dimensions of stainless steel sections were taken as those in Section 3.5. The statistical parameters are reported in Table 5.5. The obtained partial safety factors γ_{M0} are less than the current limit value of 1.1 in EN 1993-1-4 (CEN 2015) and the reliability of the proposed design interaction curve for hot-rolled stainless steel channel section stub columns under minor-axis combined loading was thus demonstrated.

5.6 Concluding remarks

An experimental and numerical modelling programme has been conducted to investigate the cross-sectional behaviour and resistances of hot-rolled stainless steel channel sections under combined compression and minor-axis bending moment. The experimental programme included initial local geometric imperfection measurements and ten eccentric compression tests on hot-rolled stainless steel channel sections about the minor principal axis. This was followed by a numerical modelling programme, where FE models were firstly developed and validated against the test results and then used to perform parametric studies to generate further numerical data over a wide range of cross-section dimensions and loading combinations. The obtained test and numerical data were used to assess the design interaction curves, as set out in EN 1993-1-4 (CEN 2015) and ANSI/AISC 370-21 (AISC 2021), with the results revealing that the codified design interaction curves lead to rather conservative and scattered failure load predictions, mainly owing to the conservative compression and bending end points. A new design interaction curve, anchored to more accurate CSM end points, was proposed and shown to offer improved design accuracy and consistency than the codified design interaction curves.

Table 5.5. Reliability analysis results calculated according to EN 1990.

Failure orientation	No. of data	$k_{d,n}$	b	V_δ	V_r	γ_{M0}
C	190	3.14	1.26	0.09	0.12	0.89
reverse C	120	3.17	1.21	0.11	0.14	0.99
Total	310	3.12	1.25	0.10	0.13	0.92

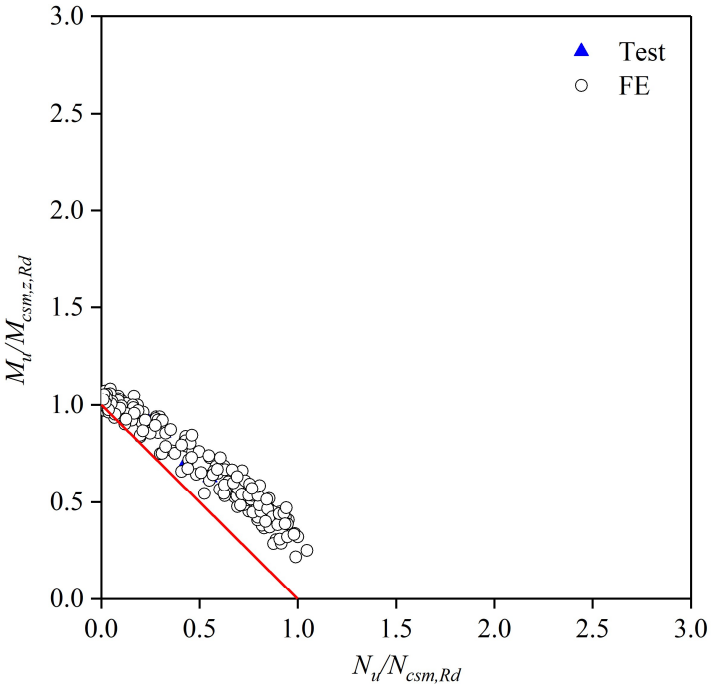

(a) In the 'C' orientation

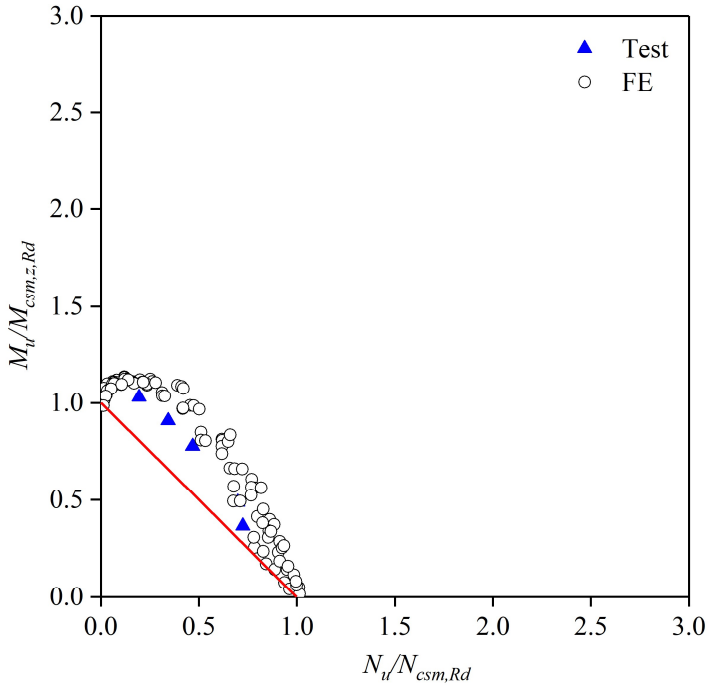

(b) In the 'reverse C' orientation

Figure 5.7. Comparisons of test and FE data against new design interaction curve.

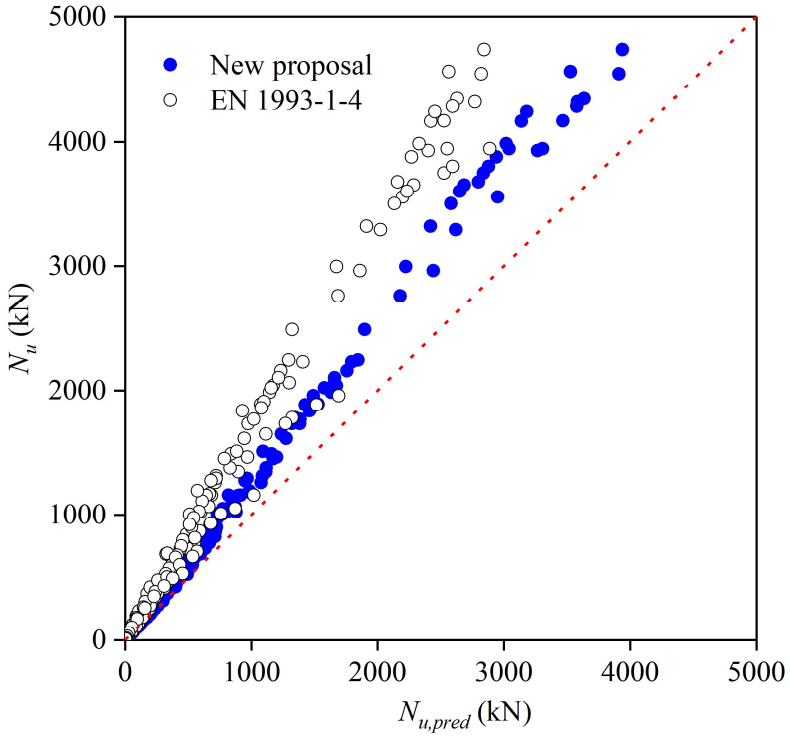

(a) In the 'C' orientation

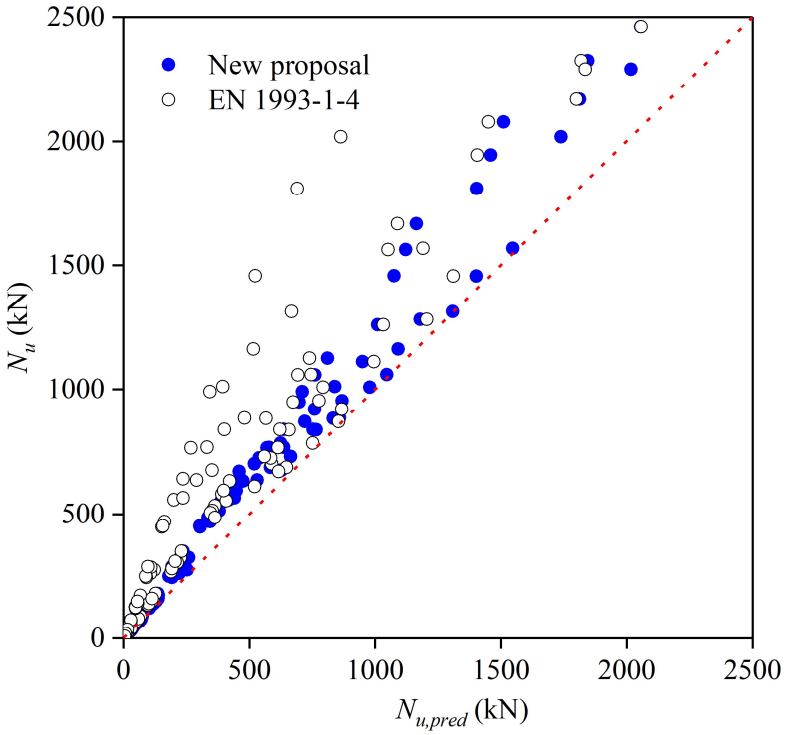

(b) In the 'reverse C' orientation

Figure 5.8. Test and FE failure loads compared with failure load predictions from EN 1993-1-4 and new proposal.

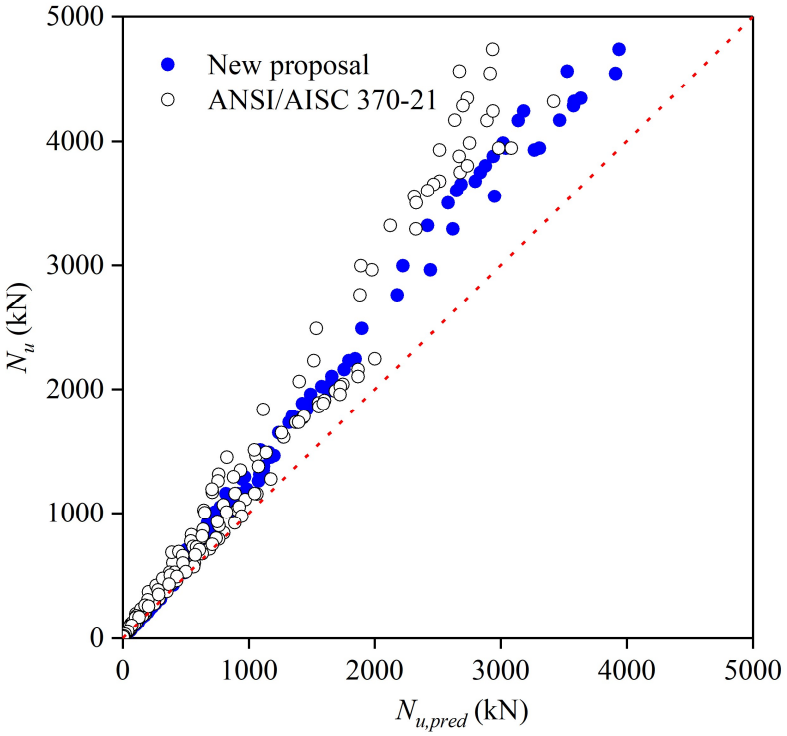

(a) In the 'C' orientation

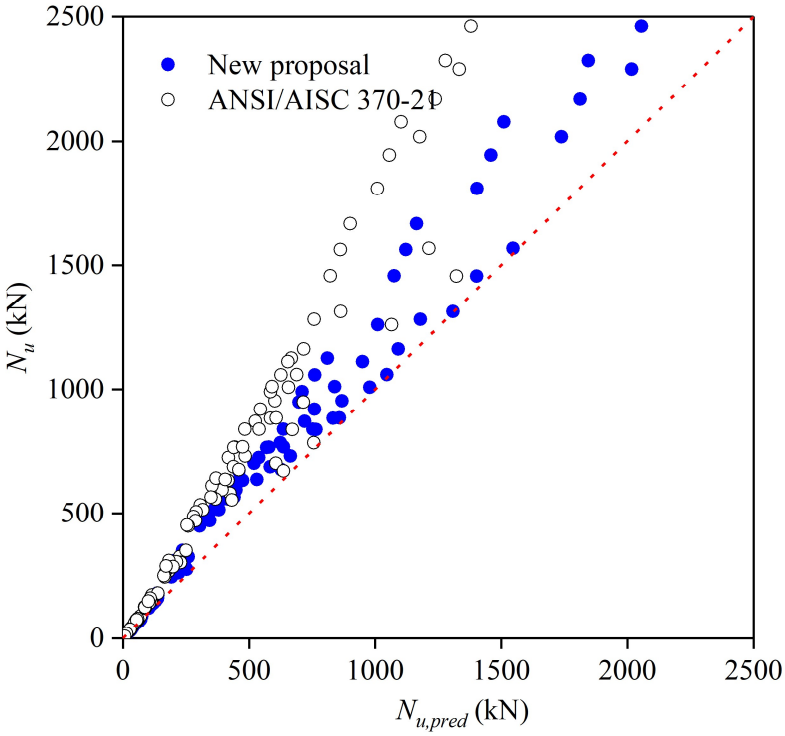

(b) In the 'reverse C' orientation

Figure 5.9. Test and FE failure loads compared with failure load predictions from ANSI/AISC 370-21 and new proposal.

CHAPTER 6

FLEXURAL BUCKLING OF CHANNEL SECTION COLUMNS

6.1 Introduction

The local buckling behaviour and cross-section resistances of hot-rolled stainless steel channel sections under isolated and combined loadings have been investigated in Chapters 3–5, while the minor-axis flexural buckling behaviour and resistances of pin-ended hot-rolled stainless steel channel section columns are studied in this chapter based on testing and numerical modelling. The testing programme included initial global and local geometric imperfection measurements and ten pin-ended column tests about the minor principal axis. Following the testing programme, a numerical modelling programme was conducted, where finite element models were developed and validated against the test results, and the validated finite element modes were then used to generate further numerical data over a wide range of cross-section dimensions and member effective lengths. The obtained test and numerical data were then adopted to assess the accuracy of relevant design rules for hot-rolled stainless steel channel section columns failing by flexural buckling about the minor principal axis, as given in the European code (CEN 2015) and American specification (AISC 2021). Finally, a revised Eurocode buckling curve was proposed. The findings of this research were reported by Li et al. (2021a).

6.2 Testing

6.2.1 General

Two plain channel sections C 80×40×5 and C 100×50×5, hot-rolled from grade EN 1.4301 austenitic stainless steel plates, were adopted in the testing programme, and it is worth noting that C 80×40×5 and C 100×50×5 are respectively categorised as Class 2 and Class 3 based on the slenderness limits given in EN 1993-1-4 (CEN 2015). For each adopted channel section, five column specimens were prepared with different member lengths, leading to a total of ten column specimens in the testing programme. The identifier of each specimen includes the cross-section label 'C1' or 'C2' ('C1' signifying channel section C 80×40×5 and 'C2' representing channel section C 100×50×5), a letter 'L' (indicating length) and a number (for the purpose of differentiating specimens with different member lengths but the same cross-section size), e.g., C2-L2. The measured geometric dimensions of each hot-rolled stainless steel channel section column specimen are reported in Table 6.1.

Table 6.1. Measured geometric dimensions and initial global and local geometric imperfections of hot-rolled stainless steel channel section column specimens.

Cross-section	Specimen ID	L (mm)	B_w (mm)	B_f (mm)	t (mm)	r (mm)	ω_0 (mm)	ω_g (mm)
C 80×40×5	C1-L1	397.4	80.47	40.28	4.73	4.70	0.03	0.13
	C1-L2	598.2	80.33	40.66	4.76	4.70	0.02	0.16
	C1-L3	799.2	80.41	40.28	4.82	4.74	0.03	-0.09
	C1-L4	998.3	80.41	40.07	4.73	4.69	0.03	-0.22
	C1-L5	1200.8	80.45	40.07	4.75	4.71	0.04	-0.32
C 100×50×5	C2-L1	500.0	98.99	49.61	4.91	4.85	0.03	0.06
	C2-L2	698.5	99.01	49.68	4.82	4.82	0.04	-0.1
	C2-L3	896.3	99.08	49.70	4.96	4.90	0.03	-0.12
	C2-L4	1120.8	99.12	49.91	4.74	4.71	0.03	0.50
	C2-L5	1299.5	99.11	49.82	4.86	4.82	0.03	0.24

6.2.2 Initial global and local geometric imperfection measurements

Initial geometric imperfections naturally exist in thin-walled steel structural members and are known to affect their buckling behaviour and resistances. Therefore, the initial global and local geometric imperfections of each hot-rolled stainless steel channel section column specimen were carefully measured. The test setup, recommended by Schafer and Peköz (1998) and having been successfully used in previous geometric imperfection measurements (dos et al. 2012; Young et al. 2018; Ye et al. 2018a; Chen et al. 2020b; Zhang et al. 2020b, 2021a; Wang et al. 2020b), was also adopted. The test setup for initial global geometric imperfection measurements is shown in Figure 6.1, where a column specimen is mounted onto the flat work bench of a CNC router, and an LVDT, pointing to the web of the column specimen, is moved along the centreline to measure the deviations about the minor principal axis (i.e. the axis of flexural buckling). The initial mid-height global geometric imperfection amplitude ω_g of each column specimen was then determined as the deviation from a linear reference line (i.e. a straight line connecting the data points recorded by the LVDT at the two ends) to the data point recorded at the mid-height, as reported in Table 6.1. It is worth noting that the obtained initial global geometric imperfection amplitude is taken as positive if the column specimen initially bows towards the flange tips – see Figure 6.2(a), but negative if the column specimen initially bows towards the web – see Figure 6.2(b). The test setup for initial local geometric imperfection measurements of a column specimen is similar to that adopted for initial global geometric imperfection measurements, as shown in Figure 6.3. It is worth mentioning that the initial local geometric imperfection of each column specimen was measured along the centrelines of the three constituent plates (one web and two flanges) over the central 300 mm; this length is regarded short enough to preclude the influence from initial global geometric imperfections, but still long enough to incorporate a typical distribution pattern of initial local geometric imperfections. For each constituent plate of a channel section column specimen, the initial local geometric imperfection magnitude was taken as the maximum deviation of the measured data set from a linear regression line fitted to the measured data set, while the initial local geometric imperfection magnitude of a channel section column

specimen ω_0 was defined as the maximum of the initial local geometric imperfection magnitudes measured from all the three constituent plates, as reported in Table 6.1.

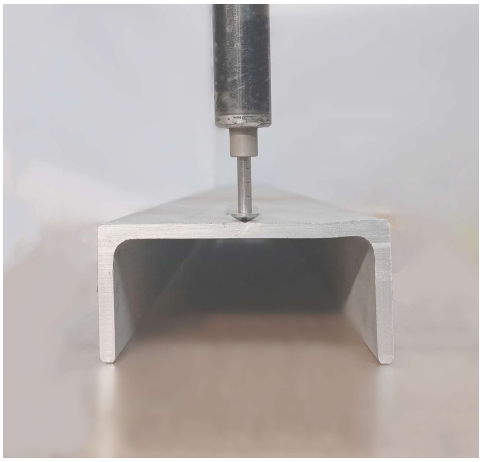

Figure 6.1. Test setup for initial global geometric imperfection measurements.

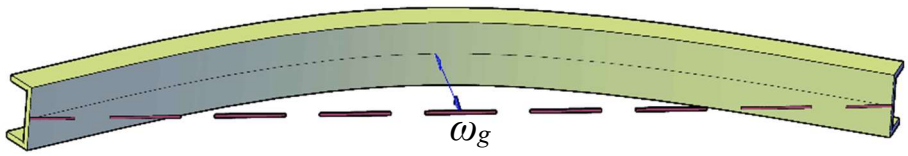

(a) Positive

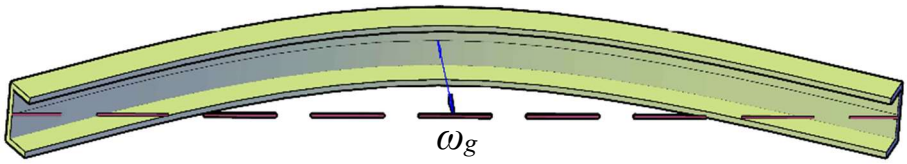

(b) Negative

Figure 6.2. Sign convention of initial global geometric imperfection ω_g.

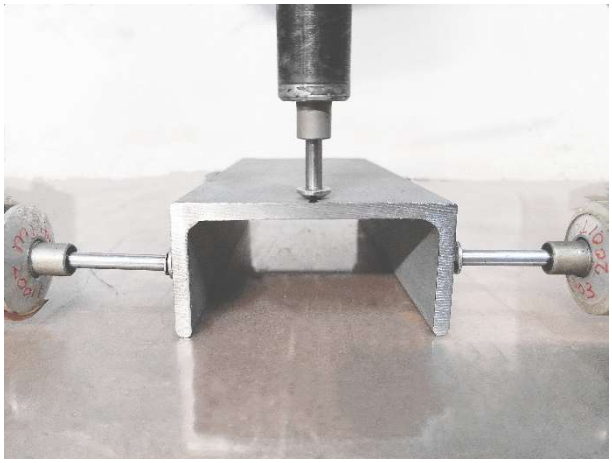

Figure 6.3. Test setup for initial local geometric imperfection measurements.

6.2.3 Pin-ended column tests

Compression tests on ten pin-ended hot-rolled stainless steel channel section columns were conducted to study their minor-axis flexural buckling behaviour and resistances. The column specimen ends were welded with steel plates, which helped prevent end cross-sections from warping and twisting. An INSTRON 5000 kN hydraulic testing machine was adopted to apply compression loads onto the column specimens and a displacement-controlled method was used to drive the testing machine, with the rate equal to 0.2 mm/min. A photograph and a schematic diagram of the pin-ended column test setup are shown in Figure 6.4. Each end of the testing machine was equipped with a knife-edge device, including a pit plate with a semi-circular groove and a wedge plate with a knife-edge wedge, to offer pin-ended boundary conditions to the column specimen ends about the axis of buckling (i.e. the minor principal axis). Prior to testing, a column specimen was firstly positioned between the top and bottom wedge plates, with the cross-section minor principal axis parallel with the knife edges and the member longitudinal axis intersecting with the knife edges at right angles, and then anchored at both ends by stiffening plates (bolted to the wedge plates using high strength bolts), before placed between the top and bottom pit plates in the testing machine. Note that the distance from the rotation centre of the knife-edge device to the end section of the specimen is equal to 75 mm, resulting in the effective length of each column specimen L_e equal to the measured member length plus an additional length of 150 mm, and the member non-dimensional slenderness about the minor principal axis (i.e. the axis of buckling) $\bar{\lambda}_z$ is calculated from Equation (6.1).

$$\bar{\lambda}_z = \sqrt{\frac{A\sigma_{0.2}L_e^2}{\pi^2 EI_z}} \tag{6.1}$$

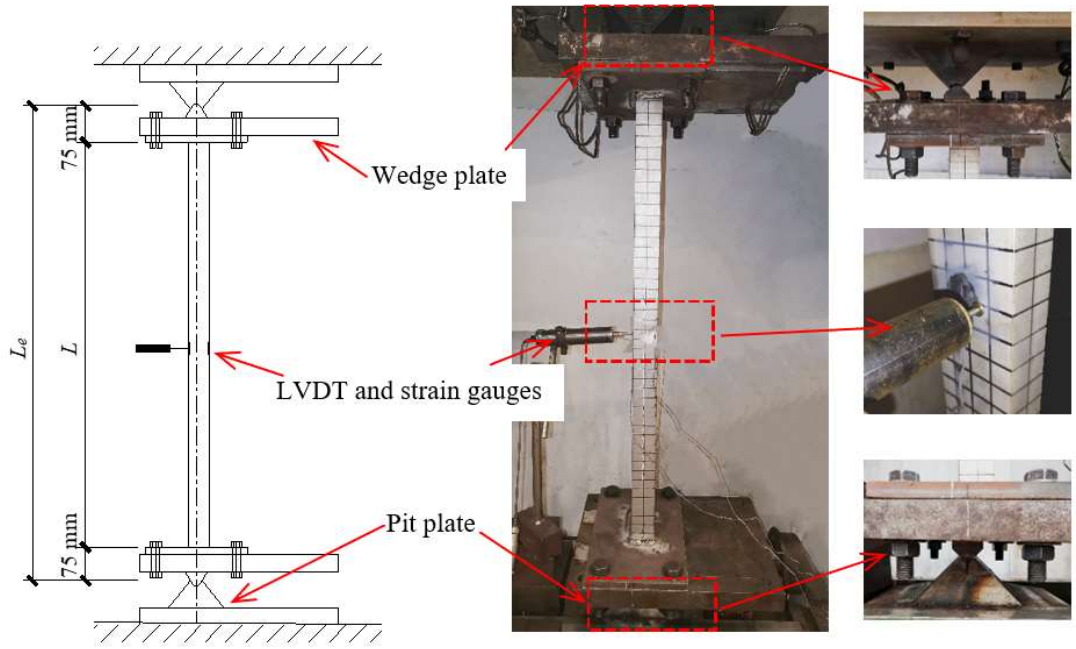

Figure 6.4. Pin-ended column test setup.

With regard to the instrumentation employed for the pin-ended column tests, as shown in Figure 6.4, an LVDT, horizontally pointing to the centreline of the web at mid-height, was adopted to monitor the lateral deflection of the column specimen along the buckling direction and two strain gauges, attached to the outer faces of the web and flange tip at the mid-height of the column specimen, were used to record the longitudinal strains at the two positions. For each column specimen, the readings from the LVDT and strain gauges were used to determine its actual overall global geometric imperfection amplitude e_m, defined as the summation of the initial loading eccentricity e_0 and the initial mid-height global geometric imperfection amplitude ω_g, based on Equation (6.2) (Huang and Young 2014; Buchanan et al. 2018; Zhang et al. 2020b), where ε_{max}-ε_{min} is the difference of the longitudinal strains measured by the one pair of strain gauges, N is the applied compression load and Δ is the mid-height lateral deflection recorded by the LVDT. Note that Equation (6.2) was obtained by assuming that the structural behaviour was close to linear elastic and it was recommended that no more than 15% of the expected failure load be used in the determination of e_m (Zhang et al. 2020b). The actual overall global geometric imperfection e_m is assumed to be positive if it leads the column specimen to bow towards the flange tips (i.e. with the relative position of the knife edge and mid-height

cross-section minor principal axis shown in Figure 6.5(a)), while the actual overall global geometric imperfection e_m is assumed to be negative if it leads the column specimen to bow towards the web (i.e. with the relative position of the knife edge and mid-height cross-section minor principal axis displayed in Figure 6.5(b)). It is worth noting that if the absolute value of the actual overall global geometric imperfection amplitude $|e_m|$ was larger than $L_e/1000$, the position of the column specimen was then carefully re-adjusted until the attainment of $|e_m|<L_e/1000$ (Huang and Young 2014; Buchanan et al. 2018; Zhang et al. 2020b). Table 6.2 reports the final actual overall global geometric imperfection amplitude e_m, together with the ratio of its absolute value to the member effective length $|e_m|/L_e$, for each hot-rolled stainless steel channel section column specimen.

$$e_m = e_0 + \omega_g = \frac{EI_z(\varepsilon_{max} - \varepsilon_{min})}{NB_f} - \Delta \tag{6.2}$$

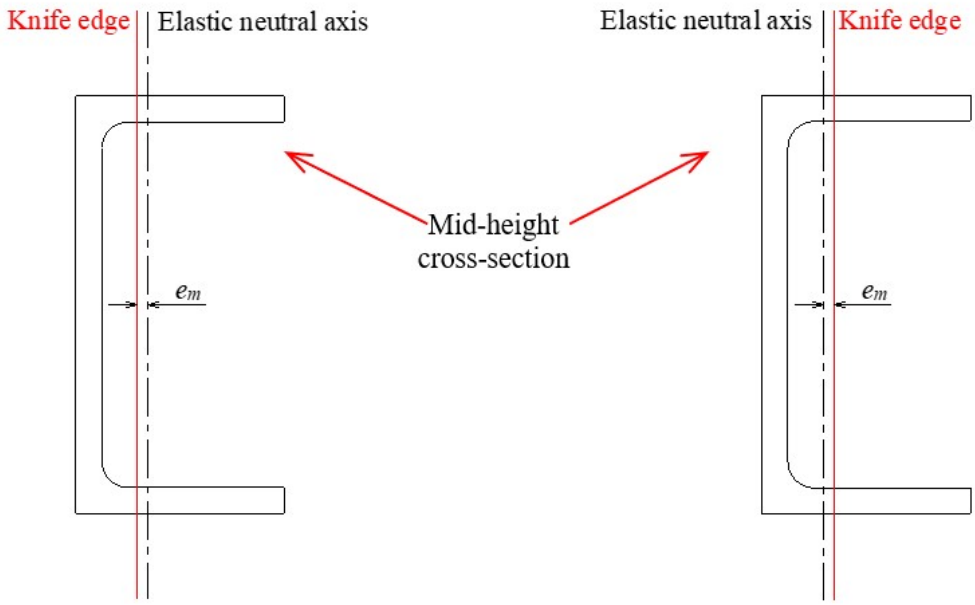

(a) Positive (b) Negative

Figure 6.5. Sign convention for actual overall global geometric imperfection e_m.

All the hot-rolled stainless steel channel section column specimens underwent noticeable global deformations upon testing and failed by visible member flexural buckling about the minor principal axis, as shown in Figure 6.6(a) and Figure 6.6(b). With regard to specimens C2-L1, C2-L4 and C2-L5 with positive actual overall

global geometric imperfection amplitudes, the induced second-order bending moments resulted in tensile stresses at the flange tips and the corresponding failure modes showed minor-axis flexural buckling in the 'reverse C' orientation. With regard to the other specimens with negative actual overall global geometric imperfection amplitudes, the induced second-order bending moments led to compressive stresses at the flange tips and the corresponding failure modes displayed minor-axis flexural buckling in the 'C' orientation. The load–mid-height lateral deflection curves measured for the C 80×40×5 and C 100×50×5 column specimens are shown in Figure 6.7(a) and Figure 6.7(b), respectively, while the key obtained test results, including the failure load $N_{u,test}$, the mid-height lateral deflection at the failure load Δ_u and the buckling orientation, are reported in Table 6.2. It is worth noting that the mid-height lateral deflections are taken as negative for channel section column specimens failing by minor-axis flexural buckling in the 'C' orientation, but positive for column specimens failing by minor-axis flexural buckling in the 'reverse C' orientation, which is consistent with the sign convention for initial and actual overall global geometric imperfections.

Table 6.2. Summary of pin-ended column test results.

Cross-section	Specimen ID	L_e (mm)	e_m (mm)	$\lvert e_m \rvert / L_e$	Failure orientation	$N_{u,test}$ (kN)	Δ_u (mm)
C 80×40×5	C1-L1	547.4	-0.45	1/1209	C	164.05	-1.34
	C1-L2	748.2	-0.39	1/1916	C	151.51	-1.24
	C1-L3	949.2	-0.57	1/1661	C	135.04	-0.92
	C1-L4	1148.3	-0.52	1/2193	C	111.43	-1.66
	C1-L5	1350.8	-0.48	1/2814	C	92.76	-1.99
C 100×50×5	C2-L1	650.0	0.42	1/1562	reverse C	338.81	5.21
	C2-L2	848.5	-0.28	1/2995	C	201.83	-0.28
	C2-L3	1046.3	-0.32	1/3244	C	194.77	-1.48
	C2-L4	1270.8	0.25	1/5043	reverse C	181.51	6.83
	C2-L5	1449.5	0.41	1/3501	reverse C	164.14	14.11

(a) C 80×40×5 specimens (from left to right: C1-L1, C1-L2, C1-L3, C1-L4 and C1-L5)

(b) C 100×50×5 specimens (from left to right: C2-L1, C2-L2, C2-L3, C2-L4 and C2-L5)

Figure 6.6. Test failure modes for hot-rolled stainless steel channel section column specimens.

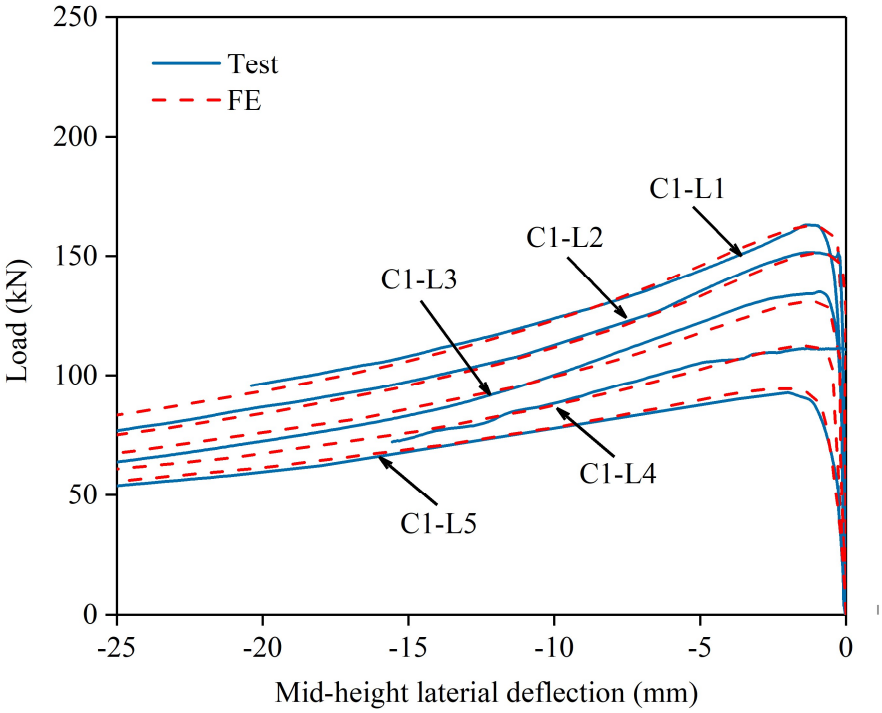

(a) C 80×40×5

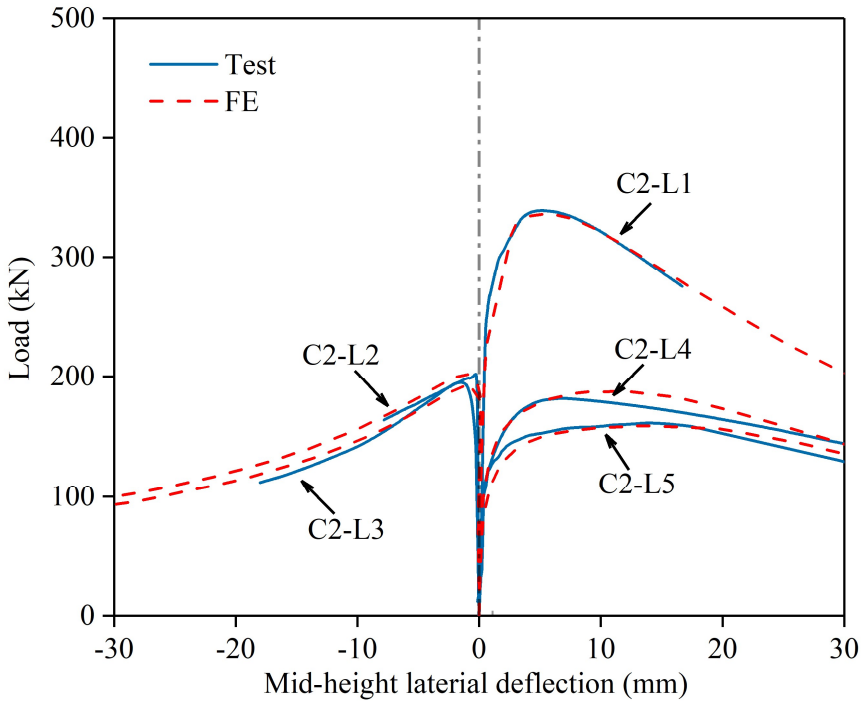

(b) C 100×50×5

Figure 6.7. Test and FE load–mid-height lateral deflection curves for column specimens.

6.3 Numerical modelling

6.3.1 General

Following the testing programme, a numerical modelling programme was conducted by means of the nonlinear finite element software ABAQUS (ABAQUS 2014). FE models were initially developed and validated against the test results and subsequently adopted to perform parametric studies to generate further numerical data on hot-rolled stainless steel channel section columns failing by minor-axis flexural buckling over a wide range of cross-section dimensions and member effective lengths.

6.3.2 Development and validation of FE models

Each hot-rolled stainless steel channel section column was modelled based on the measured cross-section dimensions and member effective length. The four-node doubly curved shell element allowing finite membrane strains and large rotations, S4R (ABAQUS 2014), has been widely adopted in previous numerical modelling of metallic channel section members (Becque and Rasmussen 2009b; Dobrić et al. 2017, 2020; Zhao and Gardner 2018; Liang et al. 2019a, 2019b, 2020; Zhang et al. 2020a, 2020b, 2020c; Dissanayake et al. 2020; Wang et al. 2020a, 2020b) and was thus also employed herein. On the basis of a prior mesh sensitivity study considering mesh sizes varying between $0.2t \times 0.2t$ and $2t \times 2t$, the final element length along the model longitudinal axis and element width along the cross-section centreline were both selected as t; this size was shown to enable an accurate simulation of membrane residual stresses and also led to a good balance between computational efficiency and accuracy. Regarding the material modelling of hot-rolled stainless steels, the measured (engineering) stress–strain curves were converted into the true stress–plastic strain curves and assigned to the corresponding FE models. Since bending residual stresses have been incorporated into the measured engineering stress–strain

curves, only membrane residual stresses were considered in this numerical modelling programme (Gardner and Cruise 2009; Huang and Young 2012; Chen and Young 2021). The membrane residual stresses were firstly predicted from the predictive model presented in Section 3.2.4 and then introduced into the FE models by means of the 'Predefined Field' command (ABAQUS 2014); Figure 6.8 depicts the membrane residual stress pattern and amplitudes incorporated into the FE model for a typical specimen C2-L1.

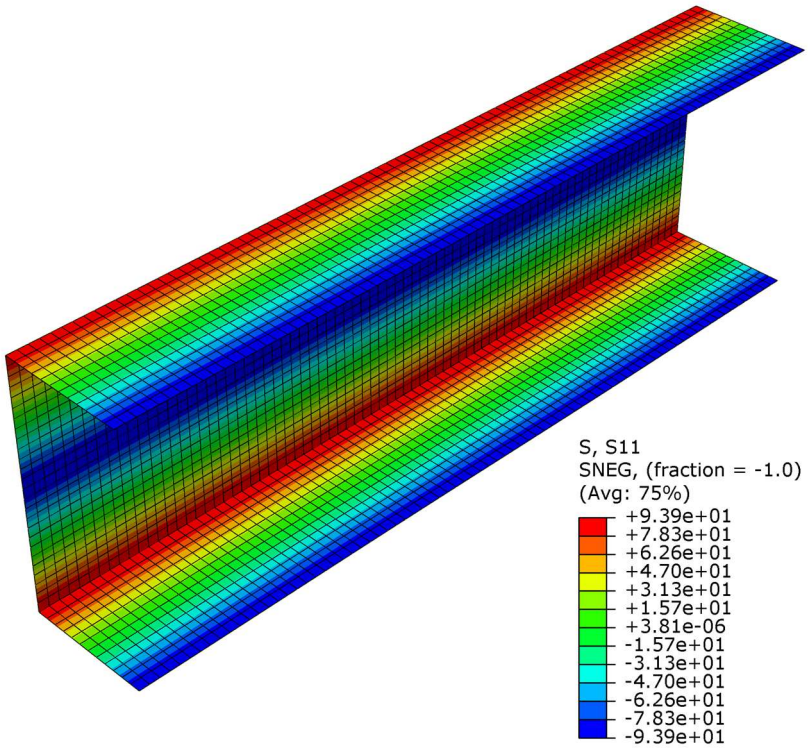

Figure 6.8. Modelled membrane residual stress pattern and amplitudes (in MPa) for specimen C2-L1.

For ease of application of boundary conditions, each end section of the channel section column FE model was coupled to a concentric reference point; the top reference point was fully restrained except for translation in the longitude direction and rotation about the minor principal axis, while the bottom reference point was only allowed for rotation about the minor principal axis, to replicate the same pin-ended boundary conditions as those adopted in the tests. In terms of the incorporation of initial global and local geometric imperfections into each channel section column FE model, the lowest elastic global (minor-axis flexural) and local buckling mode shapes

(Becque and Rasmussen 2009b; Buchanan et al. 2018; Dobrić et al. 2020; Wang et al. 2020b; Zhang et al. 2020b), obtained from an elastic eigenvalue buckling analysis, were taken as the initial global and local geometric imperfection distribution patterns, respectively; moreover, the lowest elastic global buckling mode shape was oriented such that it was consistent with that of the corresponding specimen failure orientation. Two local and global imperfection magnitude combinations, including the measured magnitude combination – $\omega_0+|e_m|$ as well as a generalised magnitude combination – $t/100+L_e/1000$, were employed to factor the obtained initial geometric imperfection distribution patterns. Upon development of the hot-rolled stainless steel channel section column FE models, the modified Risk method (ABAQUS 2014), commonly adopted for solving static numerical problems with material and geometric nonlinearities, was adopted in this study for nonlinear analyses of the developed FE models.

The numerical failure loads, load–mid-height lateral deflection curves and failure modes, as derived from the Riks analyses, were compared with those obtained from the tests, allowing the accuracy of the developed FE models to be assessed. Table 6.3 reports the numerical to test failure load ratios $N_{u,FE}/N_{u,test}$ for ten hot-rolled stainless steel channel section column specimens, with the results revealing that (i) the measured local and global imperfection magnitude combination – $\omega_0+|e_m|$ yields excellent agreement between the numerical and test failure loads, with the mean numerical to test failure load ratio of 1.00 and the corresponding COV of 0.02 and (ii) the generalised local and global imperfection magnitude combination – $t/100+L_e/1000$ also results in a satisfactory level of test failure load predictions. Figure 6.7 presents comparisons between the test and numerical load–mid-height lateral displacement curves for all the hot-rolled stainless steel channel section column specimens, evidencing that the numerical load–deformation histories well capture their test counterparts. The numerical failure modes were also shown to be in excellent agreement with their test counterparts, as displayed in Figure 6.9 and Figure 6.10 for typical specimens C1-L3 and C2-L4 with minor-axis flexural buckling in the ‘C’ and ‘reverse C’ orientations. Overall, it can be concluded that the developed FE

models can accurately simulate the test responses of the pin-ended hot-rolled stainless steel channel section column specimens and were thus deemed to be validated.

Table 6.3. Comparisons of FE failure loads with test failure loads for varying initial global and local geometric imperfection magnitude combinations.

Cross section	Specimen ID	$N_{u,FE}/N_{u,test}$	
		$\lvert\omega_g\rvert+\omega_0$	$L_e/1000+t/100$
C 80×40×5	C1-L1	0.99	0.98
	C1-L2	1.00	0.93
	C1-L3	0.97	0.89
	C1-L4	1.01	0.87
	C1-L5	1.01	0.85
C 100×50×5	C2-L1	0.99	0.88
	C2-L2	1.00	0.92
	C2-L3	0.99	0.87
	C2-L4	1.03	0.98
	C2-L5	0.97	0.92
	Mean	1.00	0.91
	COV	0.02	0.05

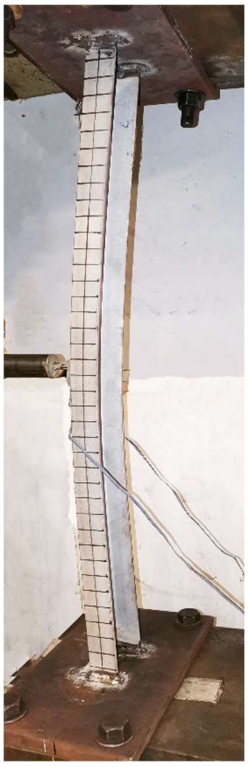

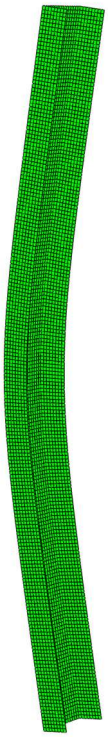

Figure 6.9. Test and FE failure modes for specimen C1-L3 (with minor-axis flexural buckling in the 'C' orientation).

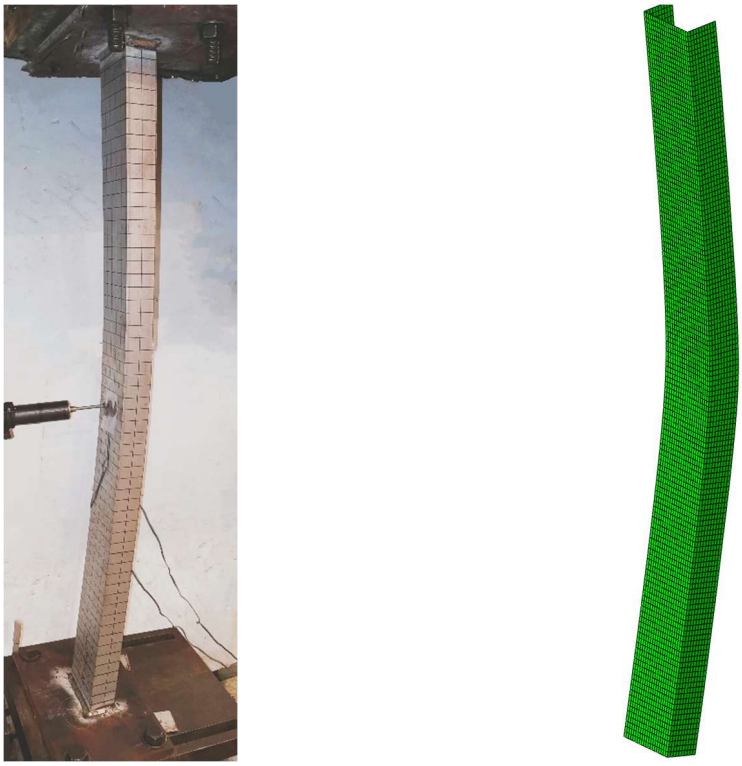

Figure 6.10. Test and FE failure modes for specimen C2-L4 (with minor-axis flexural buckling in the 'reverse C' orientation).

6.3.3 Parametric studies

Having been validated in Section 6.3.2, the developed column FE models were adopted to perform parametric studies to generate further numerical data on hot-rolled stainless steel channel section columns over a wide range of cross-section dimensions and member effective lengths. In the parametric studies, the adopted modelling procedures and techniques were the same as those described in Section 6.3.2, but with the use of the generalised imperfection magnitude combination – $t/100$ and $L_e/1000$ and the material properties of the hot-rolled stainless steel channel section C 80×40×5. Regarding the modelled cross-section geometric dimensions, the outer web widths B_w of all the modelled channel sections were fixed at 180 mm, while three outer flange widths B_f equal to 180 mm, 90 mm and 60 mm were selected, with the wall thicknesses t varied between 6 mm and 25 mm, leading to three cross-section web-to-flange aspect ratios (1.0, 2.0 and 3.0) and a range of cross-section sizes being

considered. It is worth highlighting that (i) the modelled channel sections cover three classes (Class 1–3) of non-slender cross-sections defined in EN 1993-1-4 (CEN 2015) and are also categorised as non-slender cross-sections prescribed in ANSI/AISC 370-21 (AISC 2021). For each modelled channel section, ten member effective lengths, ranged from 400 mm to 12000 mm, were selected, to obtain a wide spectrum of member non-dimensional slendernesses $\bar{\lambda}_z$ from 0.2 to 3.5. A numerical data bank, including 180 data on hot-rolled stainless steel channel section columns failing by minor-axis flexural buckling, has been generated through the parametric studies, with 108 in the 'C' orientation and 72 in the 'reverse C' orientation.

6.4 Assessment of existing international design standards

6.4.1 General

In this section, the existing design rules for pin-ended hot-rolled stainless steel channel section columns prone to minor-axis flexural buckling, as set out in the European code EN 1993-1-4 (CEN 2015) and American specification ANSI/AISC 370-21 (AISC 2021), were discussed, with their accuracy evaluated against the obtained test and numerical data. Table 6.4 reports the quantitative evaluation results, including the mean test and numerical to (unfactored) predicted failure load ratios and the corresponding COVs, while the graphical evaluation results are shown in Figures 6.11–6.13. Based on the quantitative and graphical evaluation results, the shortcomings of the codified design rules were discussed and highlighted.

Table 6.4. Comparisons of test and FE failure loads with predicted flexural buckling resistances.

Failure orientation	No. of data		$N_u/N_{u,EC3}$		$N_u/N_{u,AISC}$		$N_u/N_{u,p}$	
	Test	FE	Mean	COV	Mean	COV	Mean	COV
C	7	108	0.88	0.12	1.03	0.15	1.02	0.11
reverse C	3	72	1.06	0.03	1.25	0.04	1.22	0.06
Total	10	180	0.95	0.13	1.12	0.15	1.10	0.13

6.4.2 EN 1993-1-4

With regard to the design of column members failing by global buckling (e.g., flexural, torsional and flexural-torsional buckling), the concept of buckling curves, as developed based on the Perry-Robertson buckling formula, is adopted. Four buckling curves are defined in EN 1993-1-4 (CEN 2015) and reflect the different effects of initial geometric imperfections and residual stresses on the column buckling resistances. The unfactored EC3 design resistance of a column failing by global buckling $N_{u,EC3}$ is calculated from Equation (6.3), where χ is the reduction factor and determined from the EC3 design buckling curves, as given by Equation (6.4), where ϕ is a buckling parameter, as calculated from Equation (6.5), where α_{EC3} is the imperfection factor and $\overline{\lambda}_0$ is the limiting slenderness; note that the values of α_{EC3} and $\overline{\lambda}_0$ are equal to 0.49 and 0.40, respectively, for stainless steel channel section columns failing by flexural buckling about the minor principal axis.

$$N_{u,EC3} = \chi A \sigma_{0.2} \tag{6.3}$$

$$\chi = \frac{1}{\phi + \sqrt{\phi^2 - \overline{\lambda}_z^2}} \leq 1 \tag{6.4}$$

$$\phi = 0.5[1 + \alpha_{EC3}(\overline{\lambda}_z - \overline{\lambda}_0) + \overline{\lambda}_z^2] \tag{6.5}$$

The EC3 flexural buckling resistance predictions $N_{u,EC3}$ were evaluated against the test and numerical failure loads N_u. The graphical evaluation results are displayed in Figure 6.11, in which the test and numerical failure loads N_u, categorised by failure orientation, are normalised by the cross-section yield loads $A\sigma_{0.2}$ and plotted against the member non-dimensional slendernesses $\overline{\lambda}_z$, along with the EC3 design buckling curve, and in Figure 6.12, in which the test and numerical to EC3 predicted failure load ratios $N_u/N_{u,EC3}$, categorised by failure orientation, are plotted against the member non-dimensional slendernesses $\overline{\lambda}_z$. It can be observed that (i) the test and numerical data points for hot-rolled stainless steel channel section columns failing in the 'C' orientation lie below those for hot-rolled stainless steel channel section columns failing in the 'reverse C' orientation, which is attributed to the fact that the

second-order bending moment associated with 'C'-orientation flexural buckling leads to compressive stresses at the flange tips and hence would accelerate the global instability; (ii) the EC3 design buckling curve generally yields safe-sided, accurate and consistent flexural buckling resistance predictions for hot-rolled stainless steel channel section columns failing in the 'reverse C' orientation; (iii) the EC3 design buckling curve, however, leads to a rather large number of unsafe-sided flexural buckling resistance predictions for hot-rolled stainless steel channel section columns with failure in the 'C' orientation, especially those falling within the intermediate and low member non-dimensional slenderness range. The above analyses and discussions are also supported by the quantitative evaluation results reported in Table 6.4, where the mean ratios of $N_u/N_{u,EC3}$ are equal to 0.88 and 1.06 for hot-rolled stainless steel channel section columns failing by minor-axis flexural buckling in the 'C' and 'reverse C' orientations, with the corresponding COVs of 0.12 and 0.03.

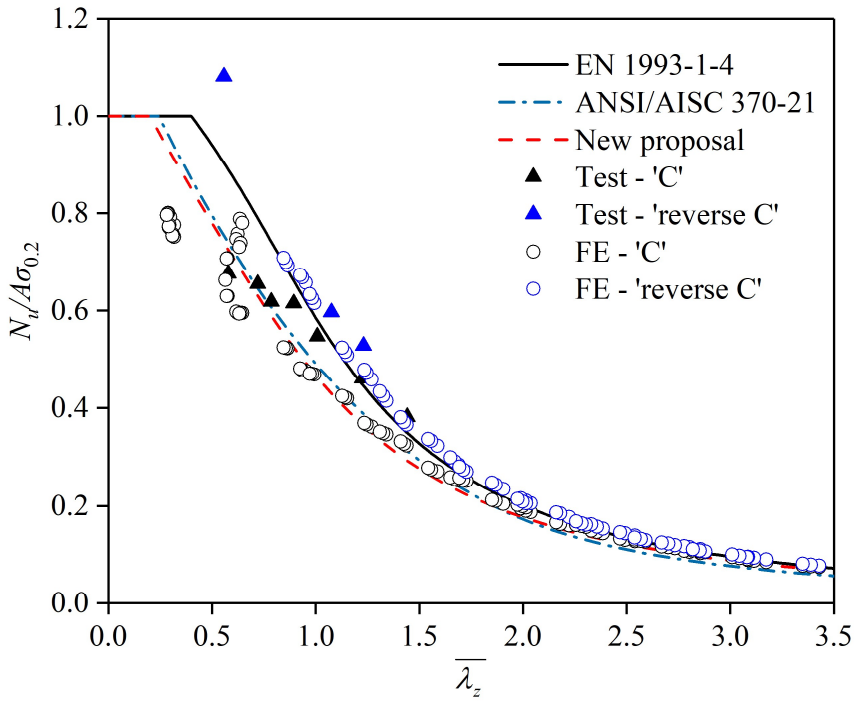

Figure 6.11. Comparisons of test and FE failure loads with codified and proposed design buckling curves.

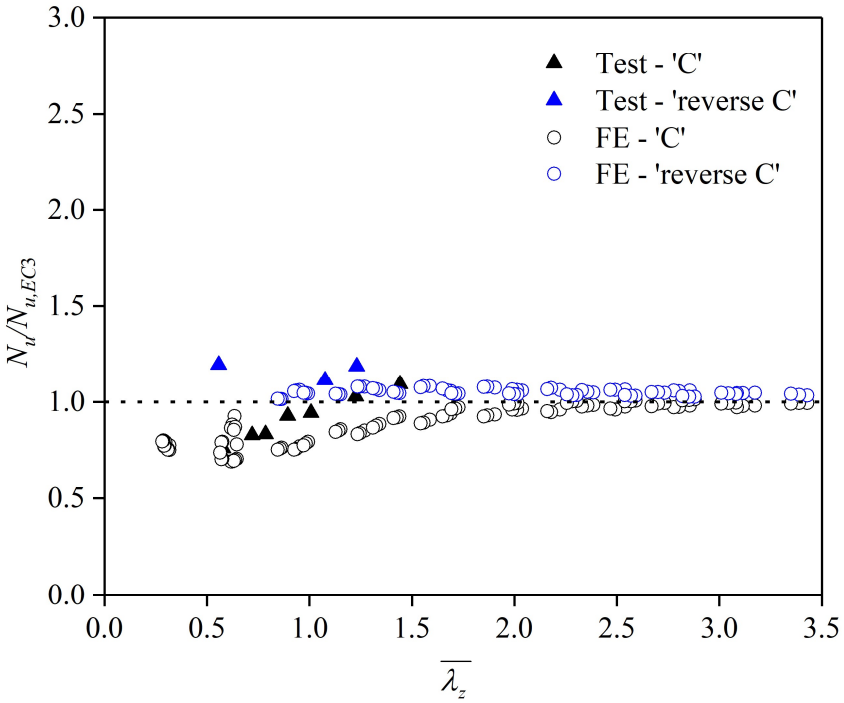

Figure 6.12. Comparisons of test and FE failure loads with EC3 flexural buckling resistance predictions.

6.4.3 ANSI/AISC 370-21

The American specification ANSI/AISC 370-21 (AISC 2021) uses the critical stress approach to determine the strengths of hot-rolled stainless steel structural columns. For non-slender element compression members failing by flexural buckling, the design member strength $N_{u,AISC}$ is determined as the product of the critical stress F_{cr} and the gross cross-section area A, as given by Equation (6.6), where the critical stress F_{cr} is dependent on the member non-dimensional slenderness $\overline{\lambda_z}$ and determined from a buckling curve defined by Equation (6.7), where F_e is the Euler buckling stress, and α, β_0, β_1 and β_2 are the four flexural buckling coefficients and taken as 0.56, 0.759, 0.409 and 0.690, respectively, for hot-rolled stainless steel channel section columns failing by flexural buckling about the minor principal axis.

$$N_{u,AISC} = AF_{cr} \tag{6.6}$$

$$F_{cr} = \begin{cases} \sigma_{0.2} & \text{for } \bar{\lambda}_z \leq \dfrac{\beta_0}{\pi} \\ 1.2\left[\beta_1^{\left(\frac{\sigma_{0.2}}{F_e}\right)^{\alpha}}\right]\sigma_{0.2} & \text{for } \dfrac{\beta_0}{\pi} < \bar{\lambda}_z \leq \sqrt{3.2} \\ \beta_2 F_e & \text{for } \sqrt{3.2} < \bar{\lambda}_z \end{cases} \quad (6.7)$$

The design flexural bucking strengths $N_{u,AISC}$ of hot-rolled stainless steel channel section columns, as predicted from ANSI/AISC 370-21 (AISC 2021), were assessed through comparisons against the test and numerical failure loads N_u. The quantitative assessment results are reported in Table 6.4, where the mean ratios of $N_u/N_{u,AISC}$ are equal to 1.03 and 1.25, for hot-rolled stainless steel channel section columns with failure in the 'C' and 'reverse C' orientations, respectively, with the corresponding COVs of 0.15 and 0.04. The graphical assessment results are presented in Figure 6.13, where the ratios of $N_u/N_{u,AISC}$ are plotted against the member non-dimensional slendernesses $\overline{\lambda_z}$. In comparison with the EC3 design buckling curve, the AISC design buckling curve results in more accurate and safe-sided flexural buckling strength predictions for hot-rolled stainless steel channel section columns over the whole considered range of member non-dimensional slendernesses up to 3.5.

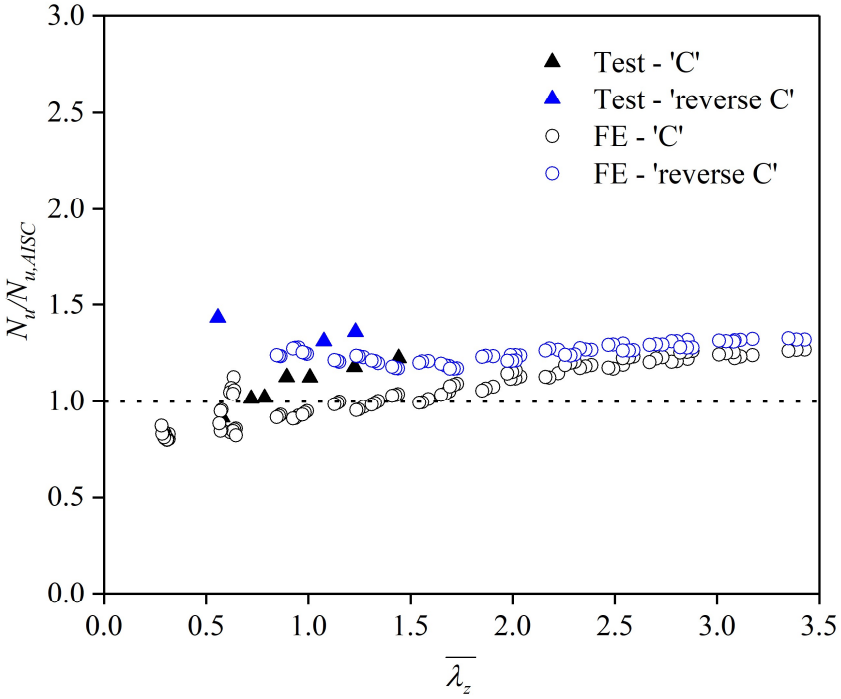

Figure 6.13. Comparisons of test and FE failure loads with AISC flexural buckling resistance predictions.

6.5 Development of new design method

In view of the fact that the EC3 design buckling curve yields a rather large number of unsafe-sided flexural buckling resistance predictions for hot-rolled stainless steel channel section columns with member non-dimensional slendernesses up to around 1.7, there is a necessity to develop a new, more accurate, EC3 design method. In this section, a new design method was developed based on the original EC3 design buckling curve, but with the use of the revised limiting slenderness $\overline{\lambda}_0$ equal to 0.2 and revised imperfection factor α_{EC3} equal to 0.76. The predicted flexural buckling resistances $N_{u,p}$ were now calculated from the revised EC3 design buckling curve and compared with the test and numerical failure loads N_u. The graphical and quantitative comparison results are presented in Figure 6.11 and Figure 6.14 and Table 6.4, respectively. In comparison with the original EC3 design buckling curve, the revised EC3 design buckling curve leads to a much higher degree of design accuracy with a greatly reduced number of unsafe flexural buckling resistance predictions for hot-rolled stainless steel channel section columns. It is worth noting that the proposed

design buckling curve is for non-slender (i.e. Class 1–3) hot-rolled stainless steel channel section columns with member non-dimensional slendernesses less than 3.5.

The reliability of the revised EC3 design buckling curve was assessed through statistical analyses, according to the requirements of EN 1990 (CEN 2002). In the reliability analyses, the material over-strength ratio and the corresponding COV for austenitic stainless steel and the COV of the geometric dimensions of stainless steel members were the same as those in Section 3.5. The key statistical parameters, calculated based on a total of 190 test and numerical data, are reported in Table 6.5, where γ_{M1} is the partial safety factor for stainless steel member resistance. As reported in Table 6.5, the resulting (calculated) partial safety factor for the revised EC3 design buckling curve is equal to 1.07, which is less than the currently adopted value of 1.10 in EN 1993-1-4 (CEN 2015). This demonstrates that the revised EC3 design buckling curve for pin-ended hot-rolled stainless steel channel section columns failing by minor-axis flexural buckling satisfies the reliability requirements of EN 1990 (CEN 2002).

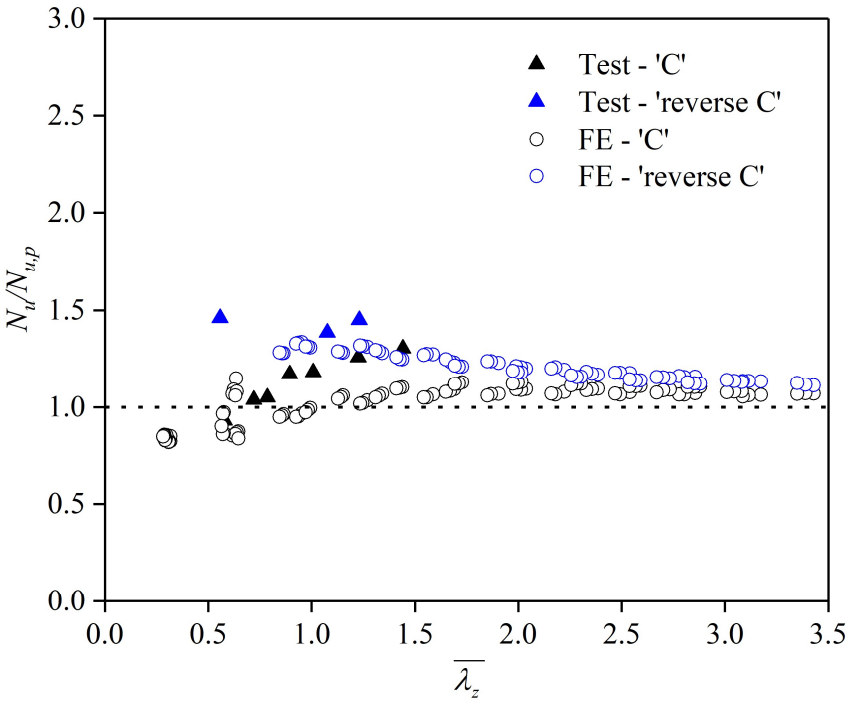

Figure 6.14. Comparisons of test and FE failure loads with flexural buckling resistance predictions from new design approach.

Table 6.5. Reliability analysis results determined according to EN 1990.

Design method	No. of test and FE data	$k_{d,n}$	b	V_δ	V_r	γ_{M1}
Revised EN 1993-1-4	190	3.20	1.09	0.09	0.12	1.07
Original EN 1993-1-4	190	3.20	0.91	0.09	0.12	1.27

6.6. Conclusions

The minor-axis flexural buckling behaviour and resistances of pin-ended hot-rolled stainless steel channel section columns have been investigated through a testing and numerical modelling programme. The testing programme included initial global and local geometric imperfection measurements and compression tests on ten pin-ended hot-rolled stainless steel channel section column specimens about the minor principal axis. The test setup and procedures were reported in detail. The key obtained test results, including the failure loads, load–mid-height lateral deflection curves and failure modes with minor-axis flexural buckling in the 'C' and 'reverse C' orientations, were presented and discussed. The test results were used in a parallel numerical modelling programme for validating the developed FE models, which were then adopted to perform parametric studies to generate further numerical data over a wide range of cross-section dimensions and member effective lengths. The test and numerical data were used to assess the accuracy of the codified design buckling curves, as set out in EN 1993-1-4 (CEN 2015) and ANSI/AISC 370-21 (AISC 2021), for pin-ended hot-rolled stainless steel channel section columns prone to flexural buckling about the minor principal axis. The EC3 design buckling curve was found to lead to many unsafe flexural buckling resistance predictions for hot-rolled stainless steel channel section columns with failure in the 'C' orientation, while the AISC design buckling curve results in accurate resistance predictions. A revised EC3 design buckling curve was proposed with the imperfection factor α_{EC3}=0.76 and limiting slenderness $\overline{\lambda}_0$ =0.2, and shown to offer accurate, consistent, safe-sided and reliable flexural buckling resistance predictions for pin-ended hot-rolled stainless steel channel section columns.

CHAPTER 7

GLOBAL BUCKLING OF CHANNEL SECTION BEAM-COLUMNS

7.1 Introduction

The global buckling behaviour of hot-rolled stainless steel channel section beam-columns under combined compression and minor-axis bending moment has been studied based on testing and numerical modelling and reported in this chapter. A testing programme was conducted on ten hot-rolled stainless steel channel section beam-columns, with five buckling towards webs and the other five buckling towards flange tips. This was followed by a numerical modelling programme, in which finite element models were firstly developed and validated against the test results and then used to perform parametric studies to generate further numerical data over a wide range of cross-section dimensions, member effective lengths and loading combinations. The test and numerical results were adopted to assess the current design interaction curves given in the European code (CEN 2015) and American specification (AISC 2021), for hot-rolled stainless steel channel section beam-columns under minor-axis combined loading. A new design interaction curve was then developed. The findings of this research have been reported by Li et al. (2022c).

7.2 Testing

7.2.1 General

An experimental programme was firstly conducted to generate a test data bank on hot-rolled stainless steel channel section beam-columns. Two plain channel sections C 80×40×5 and C 100×50×5, as hot-rolled from grade EN 1.4301 austenitic stainless steel plates, were adopted in the experimental programme and respectively classified as Class 2 and Class 3 based on the slenderness limits given in EN 1993-1-4 (CEN 2015). For each hot-rolled austenitic stainless steel channel section, five beam-column specimens with the same nominal member length were prepared and planned to be tested under eccentric compression loads at different initial loading eccentricities. The specimen ID consists of a letter ('A' and 'B' signifying C 80×40×5 and C 100×50×5, respectively) and a number (for differentiating the specimens with the same nominal member length but different initial loading eccentricities), e.g., A3. The initial global and local geometric imperfection measurements for each beam-column specimen were conducted and employed the same test setup and procedures as those described in Section 6.2.2. Table 7.1 reports the measured geometric dimensions and initial global and local geometric imperfections of each hot-rolled stainless steel channel section beam-column specimen. Note that the initial mid-height global geometric imperfection amplitude is positive if the beam-column specimen initially bows towards flange tips – see Figure 6.2(a), but negative if the beam-column specimen initially bows towards web – see Figure 6.2(b).

Table 7.1. Measured geometric dimensions and initial global and local geometric imperfections of hot-rolled stainless steel channel section beam-column specimens.

Cross-section	Specimen ID	L (mm)	B_w (mm)	B_f (mm)	t (mm)	r (mm)	ω_g (mm)	ω_0 (mm)
C 80×40×5	A1	798.2	80.34	39.92	4.82	4.81	0.16	0.03
	A2	796.0	80.48	40.15	4.86	4.82	-0.19	0.04
	A3	799.7	80.35	40.11	4.83	4.79	0.10	0.03
	A4	799.5	80.49	40.20	4.75	4.79	-0.16	0.03
	A5	797.2	80.55	40.30	4.81	4.84	-0.09	0.04
C 100×50×5	B1	797.4	99.04	50.02	4.88	4.85	-0.17	0.02
	B2	800.0	99.00	49.93	4.88	4.81	-0.09	0.02
	B3	795.3	98.99	50.03	4.84	4.89	-0.22	0.02
	B4	800.9	99.01	49.91	4.77	4.83	-0.14	0.04
	B5	797.5	99.02	50.34	4.87	4.84	-0.15	0.03

7.2.2 Beam-column (eccentric compression) tests

Eccentric compression tests were conducted on ten hot-rolled stainless steel channel section beam-columns to study their global buckling behaviour and load-carrying capacities under combined compression and minor-axis bending moment. The initial loading eccentricities to the cross-section elastic neutral axis were varied, leading to a wide range of combinations of compression load and bending moment. It is worth noting that the initial loading eccentricities are taken as positive if the resulting initial end moments lead the beam-column specimens to bow towards the flange tips but negative if the resulting initial end moments lead the beam-column specimens to bow towards the webs. Positive initial loading eccentricities were applied to the C 80×40×5 beam-column specimens, while negative initial loading eccentricities were applied to the C 100×50×5 beam-column specimens. A displacement-controlled INSTRON 5000 kN hydraulic testing machine was used for all the eccentric compression tests, with the rate of 0.2 mm/min. Each end of the testing machine was equipped with a knife-edge device – see Figure 7.1, including a pit plate containing a semi-circular groove and a wedge plate containing a knife-edge wedge, to offer pin-ended boundary conditions to the specimen ends about the minor principal axis. Prior to testing, each channel section beam-column specimen was welded with steel plates

at both ends, which helped prevent end cross-sections from twisting and warping. The channel section beam-column specimen welded with end plates was then placed between the top and bottom wedge plates, and their relative position was carefully adjusted by means of a laser and two spirit levels, to ensure that (i) the member longitudinal axis of the beam-column specimen was intersected with the wedge plates at right angles and (ii) the cross-section minor principal axis was parallel to the knife edges, with the distance equal to the pre-specified initial loading eccentricity. Upon completion of the member alignment and position adjustment, the beam-column specimen was anchored by bolting the end plates to the wedge plates. It is worth highlighting that the distance from the specimen end to the rotation centre of the knife-edge device is equal to 75 mm (see Figure 7.1). The member effective length is thus taken as L_e=L+150 mm and the corresponding member non-dimensional slenderness about the minor principal axis is calculated from Equation (6.1).

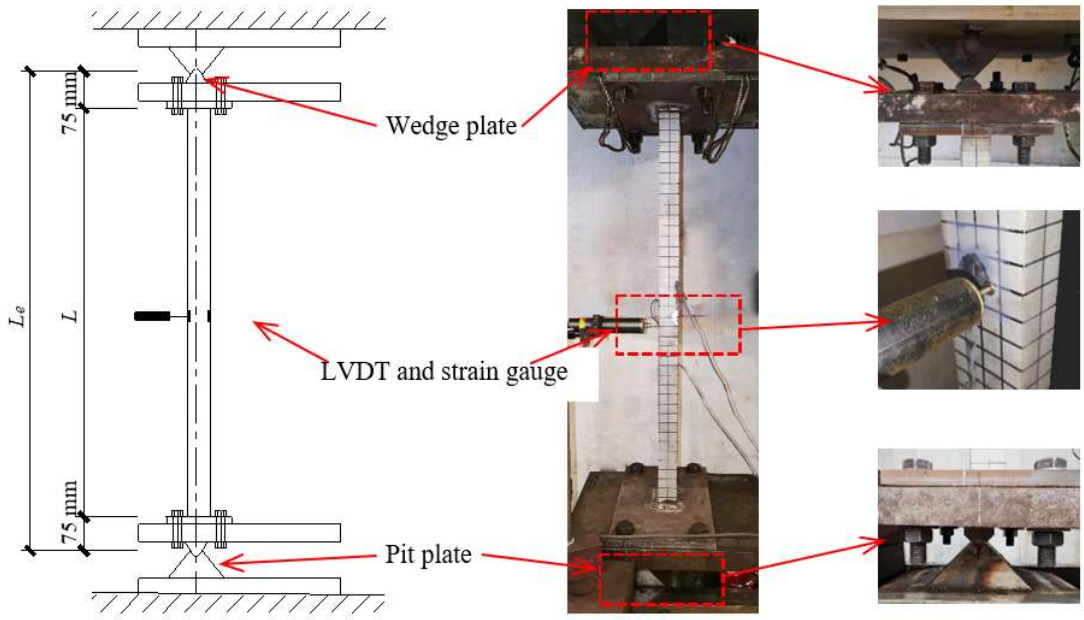

Figure 7.1. Beam-column test setup.

Figure 7.1 shows the eccentric compression test setup, where (i) two strain gauges are attached to the outer faces of the web and flange tip of the specimen at mid-height to measure the longitudinal strains at these two positions and (ii) an LVDT is perpendicularly pointing to the centreline of the web at the specimen mid-height to measure the lateral deflections about the minor principal axis. The strain gauge and

LVDT readings were used to calculate the actual initial loading eccentricity to the cross-section elastic neutral axis e_0, based on Equation (7.1) (Zhao et al. 2016d; Zhang et al. 2021a), where N is the applied eccentric compression load, I_z is the second moment of area about the minor principal axis, Δ is the mid-height lateral deflection measured by the LVDT and ε_{max}-ε_{min} is the difference of the longitudinal strains measured by the two strain gauges. Note that Equation (7.1) was derived by assuming that the structural behaviour was close to linear elastic and it was suggested that no more than 15% of the expected failure load be used in the calculation of e_0 (Zhang et al. 2021a).

$$e_0 = \frac{EI_z(\varepsilon_{max} - \varepsilon_{min})}{NB_f} - \Delta\text{-}\omega_g \tag{7.1}$$

The deformed failure mode for each C 80×40×5 beam-column specimen (i.e. under eccentric compression load with a positive initial loading eccentricity) featured noticeable minor-axis global buckling in the 'reverse C' orientation, as illustrated in Figure 7.2. The deformed failure mode for each C 100×50×5 beam-column specimen (i.e. under eccentric compression load with a negative initial loading eccentricity) featured noticeable minor-axis global buckling in the 'C' orientation, as illustrated in Figure 7.3. The load–mid-height lateral deflection curves measured for the C 80×40×5 and C 100×50×5 beam-column specimens are shown in Figure 7.4(a) and Figure 7.4(b), respectively; note that the mid-height lateral deflections are taken as positive for the C 80×40×5 beam-column specimens with global buckling in the 'reverse C' orientation, but negative for the C 100×50×5 beam-column specimens with global buckling in the 'C' orientation. The key obtained test results are reported in Table 7.2, including the actual (calculated) initial loading eccentricity to the cross-section elastic neutral axis e_0, the failure load $N_{u,test}$, the mid-height lateral deflection at the failure load Δ_u and the first-order elastic bending moment at the failure load $M_{u,1st,el}$, the second-order elastic bending moment at the failure load $M_{u,2nd,el}$ and the second-order inelastic bending moment at the failure load $M_{u,2nd,inel}$, which are calculated by Equations (7.2)–(7.4), respectively.

$$M_{u,1st,el} = N_{u,test}\left(e_0 + \omega_g\right) \tag{7.2}$$

$$M_{u,2nd,el} = \frac{N_{u,test}\left(e_0 + \omega_g\right)}{1 - \frac{N_{u,test}L_e^2}{\pi^2 EI}} \tag{7.3}$$

$$M_{u,2nd,inel} = N_{u,test}\left(e_0 + \omega_g + \Delta_u\right) \tag{7.4}$$

7.3 Numerical modelling

7.3.1 General

Following the testing programme, a numerical modelling programme was conducted by using the nonlinear finite element software ABAQUS (ABAQUS 2014). FE models were firstly developed and validated against the test results and then employed to perform parametric studies to generate further numerical data over a wide range of cross-section dimensions, member effective lengths and loading combinations.

Table 7.2. Summary of beam-column test results.

Cross-section	Specimen ID	L_e (mm)	e_0 (mm)	Failure orientation	$N_{u,test}$ (kN)	Δ_u (mm)	$M_{u,1st,el}$ (kNm)	$M_{u,2nd,el}$ (kNm)	$M_{u,2nd,inel}$ (kNm)
C 80×40×5	A1	948.2	80.76	reverse C	21.92	20.58	1.77	1.96	2.22
	A2	946.0	50.60	reverse C	33.64	18.29	1.70	1.97	2.31
	A3	949.7	19.99	reverse C	65.54	15.69	1.32	1.82	2.35
	A4	949.5	10.15	reverse C	93.81	14.56	0.94	1.55	2.30
	A5	947.2	8.02	reverse C	106.17	12.84	0.84	1.50	2.21
C 100×50×5	B1	947.4	-4.29	C	127.44	-5.12	-0.57	-0.77	-1.22
	B2	950.0	-11.05	C	92.34	-7.50	-1.03	-1.27	-1.72
	B3	945.3	-20.02	C	70.49	-8.79	-1.43	-1.67	-2.05
	B4	950.9	-50.05	C	39.04	-15.47	-1.96	-2.14	-2.56
	B5	947.5	-80.89	C	29.51	-19.20	-2.39	-2.54	-2.96

Figure 7.2. Test and FE failure modes for specimen A3 (with minor-axis global buckling in the ‘reverse C’ orientation).

Figure 7.3. Test and FE failure modes for specimen B3 (with minor-axis global buckling in the ‘C’ orientation).

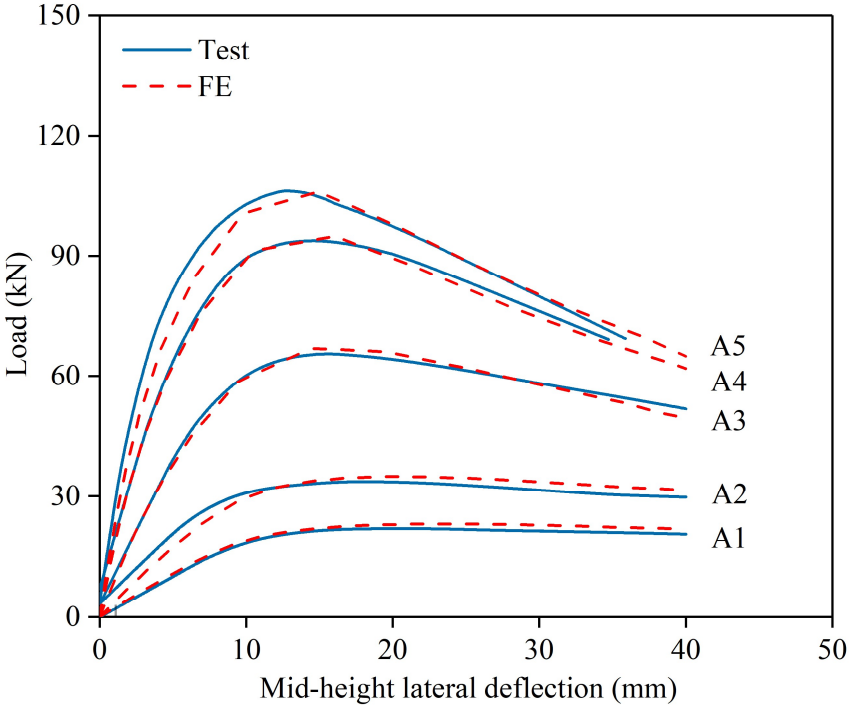

(a) C 80×40×5 specimens

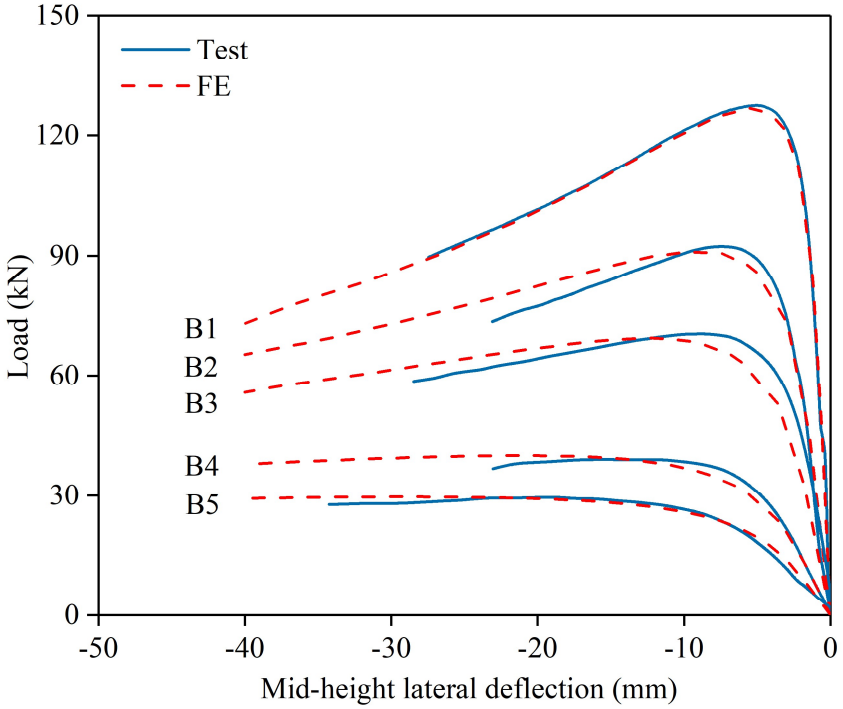

(b) C 100×50×5 specimens

Figure 7.4. Test and FE load–mid-height lateral deflection curves.

7.3.2 Development and validation of FE models

Each hot-rolled stainless steel channel section beam-column FE model was developed based on the measured cross-section geometric dimensions and member effective length, using the same modelling assumptions, procedures and techniques as those described in Section 6.3.2. Regarding the modelling of the pin-ended boundary conditions, each end of the beam-column FE model was coupled to an eccentric reference point, with the eccentricity equal to that applied in the corresponding eccentric compression test. The bottom reference point was fully restrained except for rotation about the minor principal axis, while the top reference point was allowed for rotation about the minor principal axis as well as translation in the longitudinal direction, to replicate the pin-ended boundary conditions used in the tests. Regarding the incorporation of initial geometric imperfections into each FE model, an elastic eigenvalue buckling analysis (ABAQUS 2014) was firstly conducted to obtain the lowest elastic global and local buckling mode shapes, which were taken as the initial global and local geometric imperfection distribution patterns, respectively; moreover, the lowest elastic global buckling mode shape was orientated such that it was consistent with the corresponding measured initial global geometric imperfection shape. Two (global and local) imperfection magnitude combinations, including the measured magnitude combination – $|\omega_g|+\omega_0$ and a generalised magnitude combination – $L_e/1000+t/100$, were adopted to factor the obtained initial geometric imperfection distribution patterns. Upon development of the hot-rolled stainless steel channel section beam-column FE models, the modified 'Riks' method (ABAQUS 2014), considering both material and geometric nonlinearities, was adopted to solve them.

Validation of the FE models was conducted by comparing the numerically derived results (including the failure loads, failure modes and load–deformation curves) with those obtained from the tests. Table 7.3 reports the numerical to test failure load ratios $N_{u,FE}/N_{u,test}$ for all the ten hot-rolled stainless steel channel section beam-column specimens, with the results revealing that (i) the measured imperfection magnitudes result in good agreement between the test and numerical failure loads, with the mean

$N_{u,FE}/N_{u,test}$ ratio equal to 1.01 and the corresponding COV of 0.02 and (ii) the generalised imperfection magnitudes also lead to accurate and consistent predictions of the test failure loads, with the mean $N_{u,FE}/N_{u,test}$ ratio equal to 1.00 and the corresponding COV of 0.04. The test failure modes for hot-rolled stainless steel channel section beam-columns were also well replicated by their numerical counterparts; Figure 7.2 and Figure 7.3 illustrate the comparison results for two typical specimens A3 and B3 with minor-axis global buckling in the 'reverse C' and 'C' orientations, respectively. The test and numerical load–mid-height lateral deflection curves for all the hot-rolled stainless steel channel section beam-column specimens are compared in Figure 7.4, indicating good agreement. Overall, it can be concluded that the developed FE models are capable of simulating the test structural responses and observations of the hot-rolled stainless steel channel section beam-column specimens and thus deemed to be validated.

Table 7.3. Comparisons of FE failure loads with test failure loads for varying initial global and local geometric imperfection magnitude combinations.

Cross-section	Specimen ID	$N_{u,FE}/N_{u,test}$	
		$\lvert\omega_g\rvert+\omega_0$	$L_e/1000+t/100$
C 80×40×5	A1	1.05	1.05
	A2	1.04	1.02
	A3	1.02	1.00
	A4	1.01	0.97
	A5	1.00	0.96
C 100×50×5	B1	0.99	0.96
	B2	0.99	0.97
	B3	0.99	0.98
	B4	1.03	1.06
	B5	1.00	1.02
	Mean	1.01	1.00
	COV	0.02	0.04

7.3.3 Parametric studies

Having been validated in Section 7.3.2, the developed FE models were used herein to conduct parametric studies to expand the test data pool over a wider range of cross-section dimensions, member effective lengths and loading combinations. In the

parametric studies, the modelling procedures and techniques were the same as those described in Section 7.3.2, but with the use of the generalised imperfection magnitudes (L_e/1000 and t/100). The cross-section dimensions of the modelled hot-rolled stainless steel channel section beam-columns were summarised as follows. Specifically, the outer web widths were fixed at 150 mm, while five outer flange widths equal to 150, 100, 75, 60 and 50 mm were selected, resulting in five cross-section web-to-flange aspect ratios (1.0, 1.5, 2.0, 2.5 and 3.0); the wall thicknesses were then varied between 5.0 mm and 20 mm, ensuring that the modelled hot-rolled stainless steel channel sections covered Class 1–3 cross-sections defined in EN 1993-1-4 (CEN 2015). For each modelled hot-rolled stainless steel channel section, a series of member effective lengths were selected to cover a wide range of member non-dimensional slendernesses from 0.4 to 3.0. Then, for each developed hot-rolled stainless steel channel section beam-column model, an extensive variety of initial loading eccentricities from 1 mm to 1000 mm were chosen and the initial loading eccentricities at both sides of the cross-section elastic neutral axis were considered, to study the global buckling behaviour and load-carrying capacities of hot-rolled stainless steel channel section beam-columns under a broad range of combinations of compression load and minor-axis bending moment and failing in both 'C' and 'reverse C' orientations. Overall, 1341 numerical data on hot-rolled stainless steel channel section beam-columns have been generated from the parametric studies.

7.4 Assessment of existing international design standards

7.4.1 General

The current design interaction curves for hot-rolled stainless steel channel section beam-columns, as set out in the European code EN 1993-1-4 (CEN 2015) and American specification ANSI/AISC 370-21 (AISC 2021), were firstly assessed against the obtained test and numerical data. The shortcomings of the codified design interaction curves were highlighted. Table 7.4 reports the mean test and numerical to (unfactored) predicted failure load ratios $N_u/N_{u,pred}$ and the corresponding COVs for

each of the codified design methods. Figure 7.6 and Figure 7.7 display the graphical assessment results, where the test and numerical to predicted failure load ratios $N_u/N_{u,pred}$ are plotted against the angle θ. The angle $\theta = \tan^{-1}\left[\left(N_{u,pred}/N_R\right)/\left(M_{u,pred}/M_R\right)\right]$ is introduced to reflect the combination of compression load and minor-axis bending moment, as also graphically defined in Figure 7.5, where $N_{u,pred}$ is the predicted failure load and $M_{u,pred}=N_{u,pred}e_0$ is the predicted failure moment, while N_R denotes the member resistance under pure compression (i.e. column minor-axis flexural buckling resistance) and M_R denotes the member resistance under pure bending (i.e. cross-section minor-axis bending moment resistance); note that the value of θ changes from 0° to 90° when the applied combined loading varies from pure bending to pure compression.

Table 7.4. Comparisons of test and FE failure loads with predicted failure loads.

(a) EN 1993-1-4

Failure orientation	Class 1 and 2			Class 3			Total		
	No. of data	Mean	COV	No. of data	Mean	COV	No. of data	Mean	COV
C	417	1.00	0.06	249	1.35	0.16	666	1.13	0.19
reverse C	455	1.25	0.06	220	1.76	0.09	675	1.42	0.18
Total	872	1.13	0.12	469	1.54	0.18	1341	1.28	0.22

(b) ANSI/AISC 370-21

Failure orientation	Compact			Non-compact			Total		
	No. of data	Mean	COV	No. of data	Mean	COV	No. of data	Mean	COV
C	417	0.88	0.08	249	1.22	0.11	666	1.01	0.19
reverse C	455	1.05	0.09	220	1.06	0.08	675	1.05	0.08
Total	872	0.97	0.12	469	1.14	0.12	1341	1.03	0.14

(c) New design method[a]

Failure orientation	Class 1 and 2			Class 3			Total		
	No. of data	Mean	COV	No. of data	Mean	COV	No. of data	Mean	COV
C	417	1.05	0.03	249	1.08	0.03	666	1.06	0.03
reverse C	455	1.29	0.10	220	1.30	0.08	675	1.29	0.09
Total	872	1.18	0.13	469	1.19	0.12	1341	1.18	0.12

Note: [a] The cross-section classes are determined based on EN 1993-1-4 (CEN 2015).

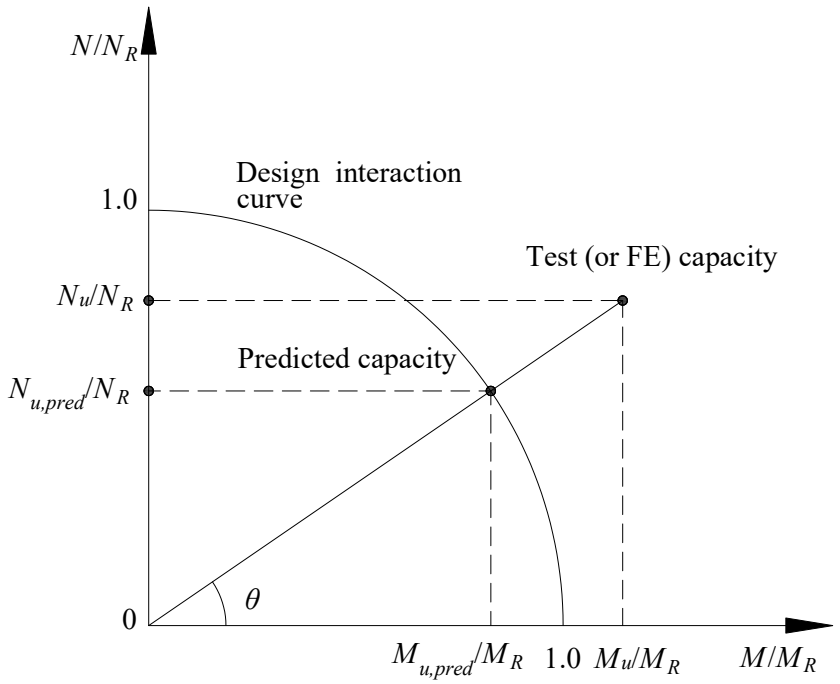

Figure 7.5. Definition of θ.

7.4.2 EN 1993-1-4

The European code EN 1993-1-4 (CEN 2015) prescribes the use of an interaction curve for the design of stainless steel open and tubular section beam-columns. The EC3 design interaction curve is expressed by Equation (7.5), where $N_{b,z,Rd}$ is the EC3 column buckling resistance and calculated based on the EC3 design buckling curve; for stainless steel open section columns susceptible to minor-axis flexural buckling, the imperfection factor is taken as α_{EC3}=0.49 and the limiting slenderness is taken as $\bar{\lambda}_0$=0.4, $M_{EC3,z,Rd}$ is the EC3 cross-section minor-axis bending moment resistance, which is equal to the plastic moment capacity $M_{pl,z}$ for Class 1 and 2 channel sections but the elastic moment capacity $M_{el,z}$ for Class 3 channel sections without considering material strain hardening, and k_z is the EC3 interaction factor considering the interaction between compression load and bending moment, as defined by Equation (7.6); note that $N_{b,z,Rd}$ and $M_{EC3,z,Rd}$ are actually the end points of the EC3 design interaction curve, while k_z defines the shape.

$$\frac{N_{u,EC3}}{N_{b,z,Rd}} + k_z \frac{M_{uz,EC3}}{M_{EC3,z,Rd}} = 1 \tag{7.5}$$

$$1.2 \leq k_z = 1 + 2(\overline{\lambda_z} - 0.5)\frac{N_{u,EC3}}{N_{b,z,Rd}} \leq 1.2 + 2\frac{N_{u,EC3}}{N_{b,z,Rd}} \tag{7.6}$$

The EC3 design interaction curve for hot-rolled stainless steel channel section beam-columns was assessed against the obtained test and numerical data. Table 7.4(a) reports the quantitative assessment results, arranged by failure orientation and cross-section class, while the corresponding graphical assessment results are presented in Figure 7.6. It is evident that the EC3 design interaction curve generally leads to inaccurate and scattered failure load predictions for hot-rolled stainless steel channel section beam-columns, which can be attributed to the inaccurate end points and the improper shape. Moreover, for channel section beam-columns failing by global buckling in the 'reverse C' orientation (i.e. with lower susceptibility to buckling and higher load-carrying capacities), the predicted failure loads are more conservative than those for channel section beam-columns failing by global buckling in the 'C' orientation. It is also worth noting that the predictions are more conservative for Class 3 channel section beam-columns than for Class 1 and 2 channel section beam-columns, mainly owing to the use of the elastic moment capacity as the bending end point of the EC3 design interaction curve without considering any material plasticity. In addition, many of the predictions for Class 1 and 2 channel section beam-columns are unsafe, regardless of the combined loading cases, owing principally to the improper shape of the EC3 design interaction curve and the unconservative compression end point.

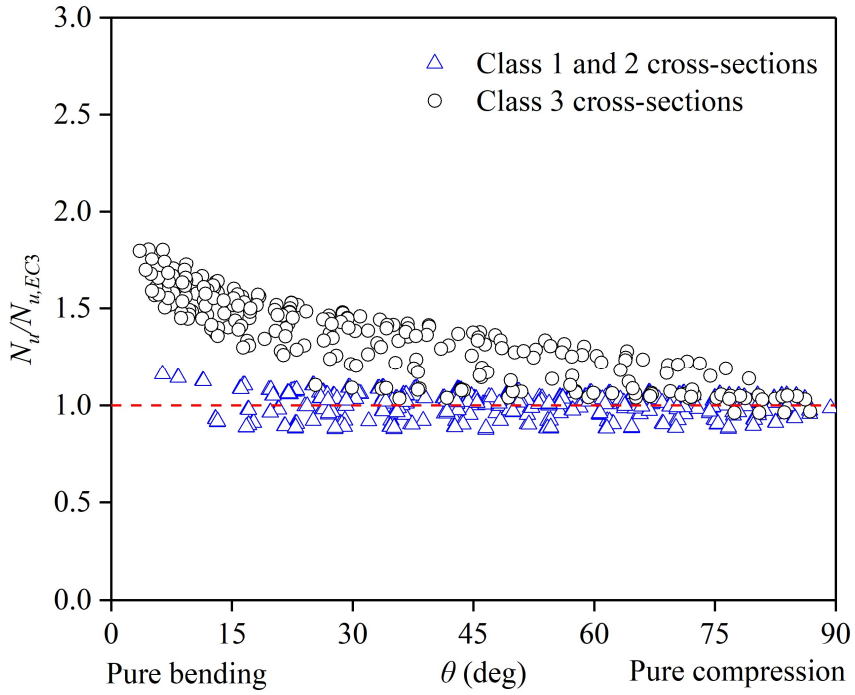

(a) In the 'C' orientation

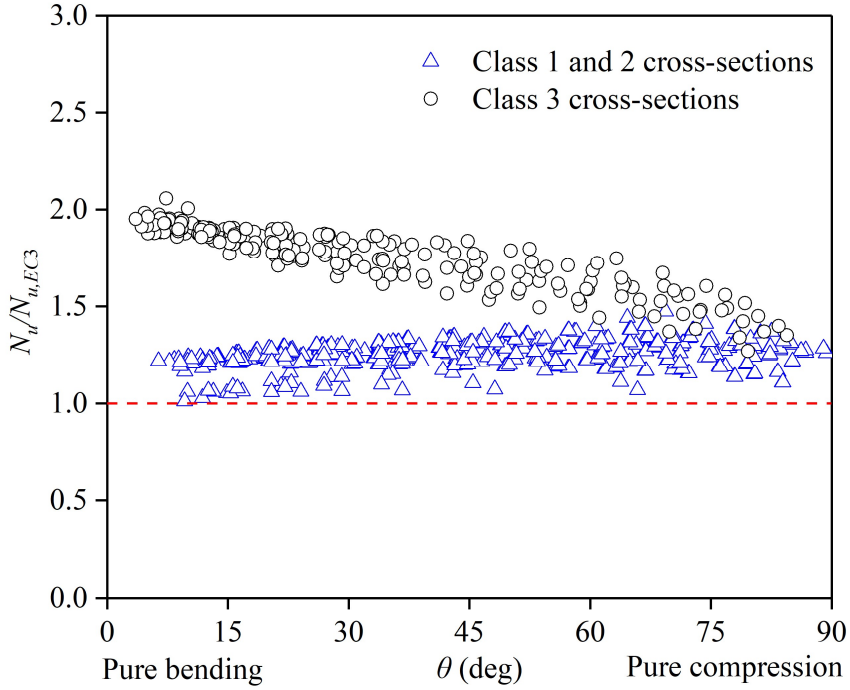

(b) In the 'reverse C' orientation

Figure 7.6. Comparisons of hot-rolled stainless steel channel section beam-column test and FE failure loads with predicted failure loads from EN 1993-1-4.

7.4.3 ANSI/AISC 370-21

For the design of hot-rolled stainless steel channel section beam-columns, a two-stage interaction curve is adopted by the American specification ANSI/AISC 370-21 (AISC 2021), as defined by Equation (7.7), where $N_c=AF_{cr}$ is the AISC column buckling resistance and determined by the critical stress method, in which F_{cr} is the member critical stress for columns susceptible to minor-axis flexural buckling and calculated from Equation (7.8), where F_e is the Euler buckling stress, and α, β_0, β_1 and β_2 are the four flexural buckling coefficients and taken as 0.56, 0.759, 0.409 and 0.690, respectively, M_{cz} is the AISC cross-section minor-axis bending moment resistance, which is taken as the plastic moment capacity for compact cross-sections and determined by considering partial plasticity for non-compact cross-sections, and $\alpha_A=1/(1-N_{u,AISC}/N_{cr})$ is the amplification factor to consider all the interaction effects, in which N_{cr} is the Euler buckling load about the minor principal axis.

$$\begin{cases} \dfrac{N_{u,AISC}}{N_c}+\dfrac{8}{9}\dfrac{\alpha_A M_{u,AISC}}{M_{cz}}=1 & \text{for } \dfrac{N_{u,AISC}}{N_c}\geq 0.2 \\ \dfrac{N_{u,AISC}}{2N_c}+\dfrac{\alpha_A M_{u,AISC}}{M_{cz}}=1 & \text{for } \dfrac{N_{u,AISC}}{N_c}< 0.2 \end{cases} \tag{7.7}$$

$$F_{cr}=\begin{cases} \sigma_{0.2} & \text{for } \bar{\lambda}_z \leq \dfrac{\beta_0}{\pi} \\ 1.2\left[\beta_1^{\left(\frac{\sigma_{0.2}}{F_e}\right)^{\alpha}}\right]\sigma_{0.2} & \text{for } \dfrac{\beta_0}{\pi}<\bar{\lambda}_z \leq \sqrt{3.2} \\ \beta_2 F_e & \text{for } \sqrt{3.2}<\bar{\lambda}_z \end{cases} \tag{7.8}$$

The failure loads, as calculated based on the AISC design interaction curve, were evaluated against the test and numerical failure loads. The quantitative evaluation results are reported in Table 7.4(b), while the graphical evaluation results are displayed in Figure 7.7. On the basis of the quantitative and graphical evaluation results, it can be concluded that the AISC design interaction curve (similar to its EC3 counterpart) results in inaccurate and scattered failure load predictions for hot-rolled stainless steel channel section beam-columns, which can be attributed to the inaccurate end points and the improper shape.

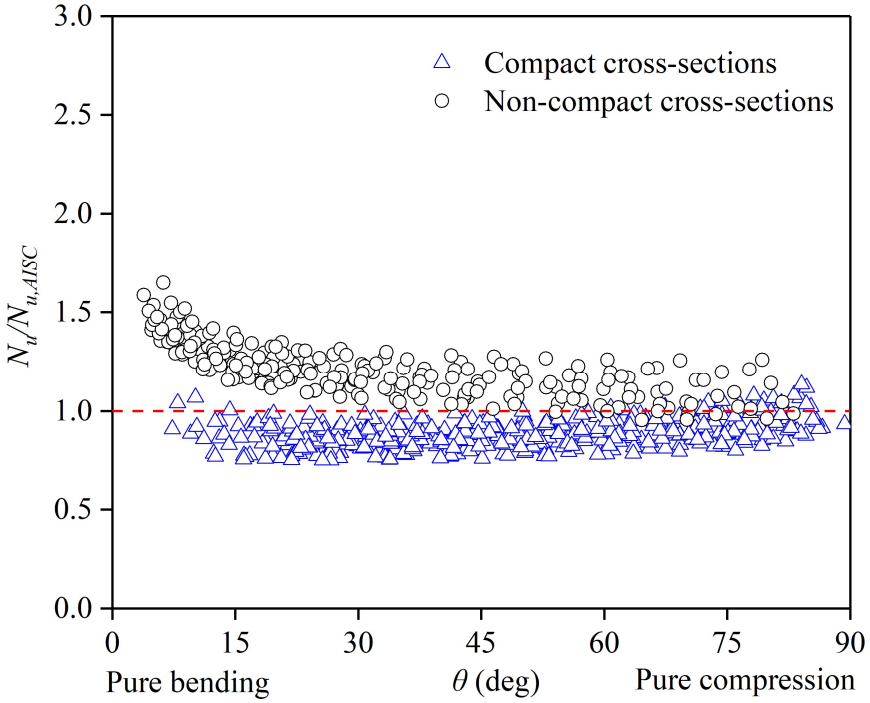

(a) In the 'C' orientation

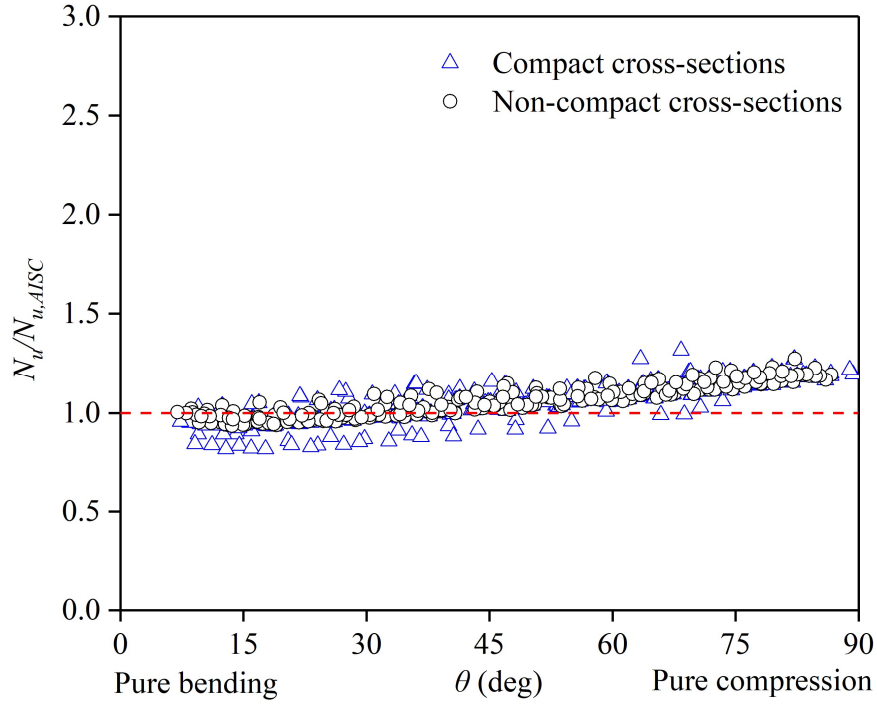

(b) In the 'reverse C' orientation

Figure 7.7. Comparisons of hot-rolled stainless steel channel section beam-column test and FE failure loads with predicted failure loads from ANSI/AISC 370-21.

7.5 Development of new design method

In this section, a new improved design interaction curve is proposed through adopting more accurate end points and then developing more proper shape. Considering that the codified bending end point (i.e. cross-section minor-axis bending moment resistance) suffers from being determined without considering material strain hardening, the new bending end point is now determined by using the CSM (Afshan and Gardner 2013; Zhao et al. 2017; Zhao and Gardner 2018), which is a deformation-based design approach exploiting material strain hardening in the design. In view of the fact that the codified design rules usually result in over-predicted resistances for hot-rolled stainless steel channel section columns prone to minor-axis flexural buckling, a revised EC3 design buckling curve has been previously proposed in Section 6.5 and is ideal to be used to calculate the compression end point of the new design interaction curve.

The use of the CSM for the calculation of cross-section resistances under pure minor-axis bending has been described in Section 5.5. The CSM cross-section bending resistance $M_{csm,z,Rd}$ is given by Equitation (5.5). The new column flexural buckling resistance $N_{br,z,Rd}$ is calculated by the revised EC3 buckling curve for hot-rolled stainless steel channel section columns, which adopts the format of the original EC3 design buckling curve, but with a revised limiting slenderness $\overline{\lambda}_0$ equal to 0.20 and a revised imperfection factor α_{EC3} equal to 0.76. Therefore, the new design interaction curve was proposed, as given by Equation (7.9). Derivation of the new interaction factor k_n is conducted based on one typical Class 1 channel section C 150×60×9 and one typical Class 3 channel section C 150×60×6. Specifically, FE models with various member non-dimensional slendernesses under a range of loading combinations were firstly developed, from which the FE failure loads $N_{u,p}$ and failure moments $M_{u,p}$ were determined; the value of k_n for each member non-dimensional slenderness $\overline{\lambda}_z$ and compression load level $n_b=N_{u,p}/N_{br,z,Rd}$ was then calculated according to Equation (7.10), which is a re-arrangement of Equation (7.9).

$$\frac{N_{u,p}}{N_{br,z,Rd}} + k_n \frac{M_{u,p}}{M_{csm,z,Rd}} = 1 \tag{7.9}$$

$$k_n = (1 - \frac{N_{u,p}}{N_{br,z,Rd}}) / \frac{M_{u,p}}{M_{csm,z,Rd}} \tag{7.10}$$

The two sets of the numerically calculated k_n data points corresponding to different cross-section classes show a relatively low level of scatter; typical k_n data points for n_b=0.3 are illustrated in Figure 7.8. Therefore, the upper set of the numerically calculated k_n (represented for clarity as curves passing through the data points – see Figure 7.9) is used to derive a formula for k_n. Given that each of the $k_n - \overline{\lambda}_z$ curves for different compression load levels displays a bi-linear trend, the formula for k_n is assumed to be of the traditional bi-linear form, as commonly used for beam-column interaction factors (Greiner and Lindner 2006; Boissonnade et al. 2006) and given by Equation (7.11), where D_1 and D_2 are the coefficients defining the relevant linear relationship between k_n and $\overline{\lambda}_z$ in the low member non-dimensional slenderness range, while D_3 is a limit value, beyond which the interaction factor k_n remains constant (i.e. there is a zero slope to the proposed $k_n - \overline{\lambda}_z$ curve for $\overline{\lambda}_z \geq D_3$). Following a series of regression fits, the values of D_1, D_2 and D_3 are finally selected as 4.0, 0.2 and 1.1, respectively, and reported in Table 7.5; note that the corresponding coefficients for duplex and ferritic stainless steel channel section beam-columns, which are out of the scope of the present study, have also been derived and shown in Table 7.5. The numerically calculated $k_n - \overline{\lambda}_z$ curves are compared with the corresponding proposed curves in Figure 7.10, indicating good agreement for various member non-dimensional slendernesses and compression load levels. It is worth noting that the proposed design interaction curve is applicable for non-slender hot-rolled stainless steel channel section beam-columns with member non-dimensional slendernesses less than 3.0 subjected to any case of minor-axis combined loading.

$$k_n = 1 + D_1(\overline{\lambda}_z - D_2)n_b \leq 1 + D_1(D_3 - D_2)n_b \tag{7.11}$$

The proposed design interaction curve for hot-rolled stainless steel channel section beam-columns was assessed by comparing the predicted failure loads against the test and numerical failure loads. As can be seen from Table 7.4(c), where the quantitative assessment results are reported, the mean $N_u/N_{u,p}$ ratios are lower than their EC3 counterparts and the COVs are only about one half of the corresponding codified values, revealing a higher degree of design accuracy and consistency. This is also supported by the graphical assessment results in Figure 7.11, where the $N_u/N_{u,p}$ ratios for various cross-section dimensions, member non-dimensional slendernesses and combinations of loading show a consistent trend and are just above 1.0 (indicating accurate and safe failure load predictions).

Table 7.5. Proposed coefficients for k_n.

Material grade	D_1	D_2	D_3
Austenitic stainless steel	4.0	0.2	1.1
Ferritic stainless steel	4.0	0.2	1.1
Duplex stainless steel	4.0	0.2	1.1

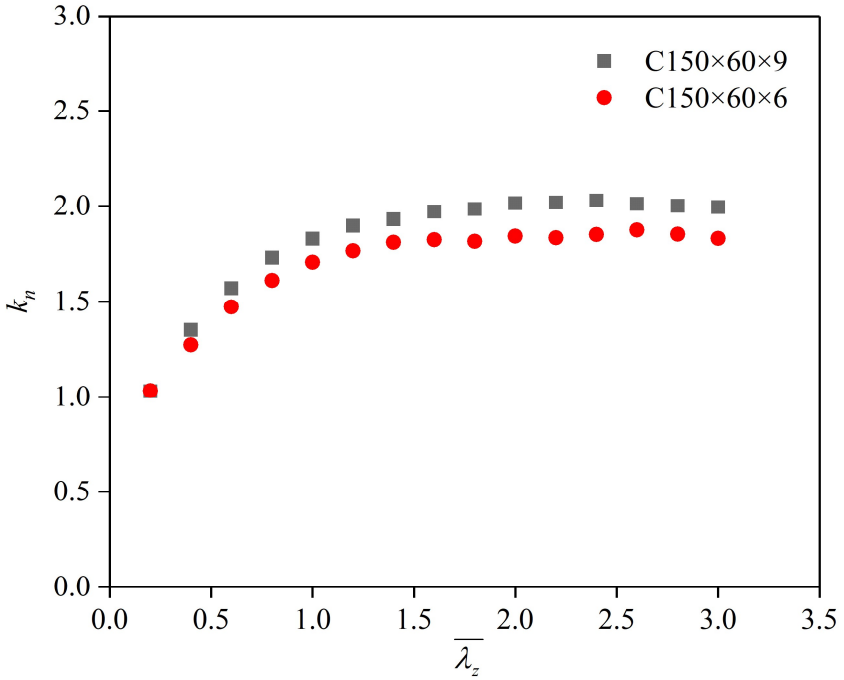

Figure 7.8. Typical numerically calculated k_n corresponding to n_b=0.3.

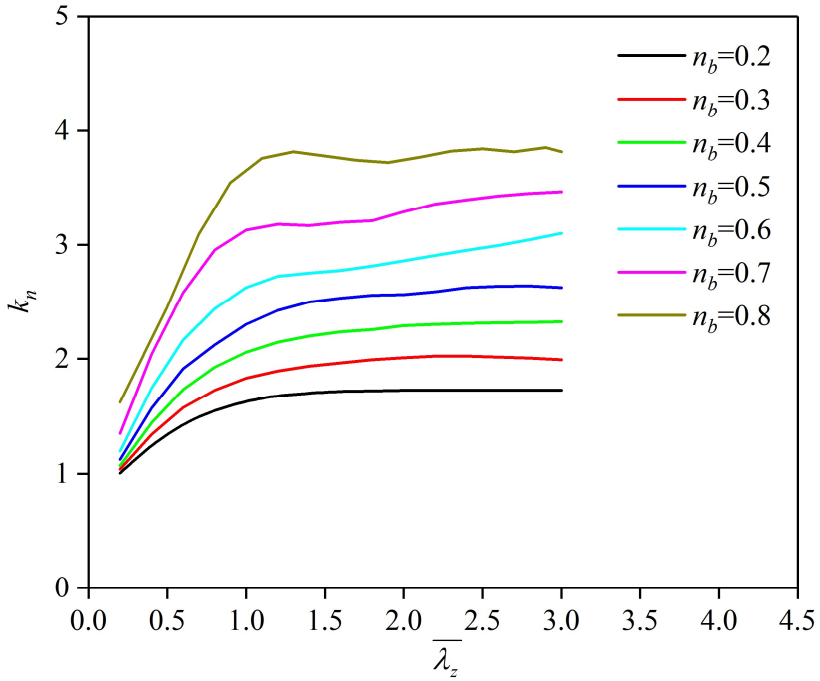

Figure 7.9. The upper set of the numerically calculated k_n.

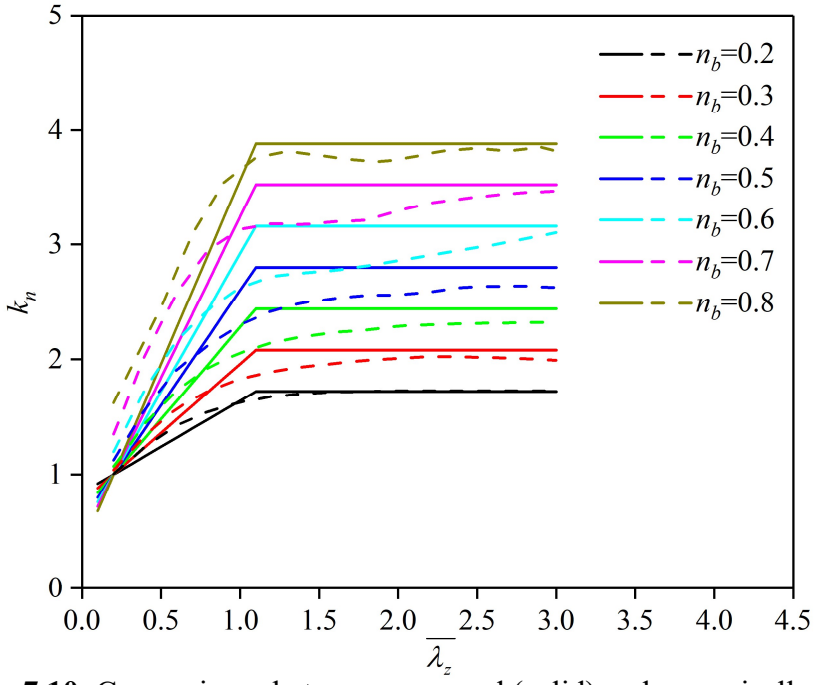

Figure 7.10. Comparisons between proposed (solid) and numerically calculated (dotted) curves for k_n.

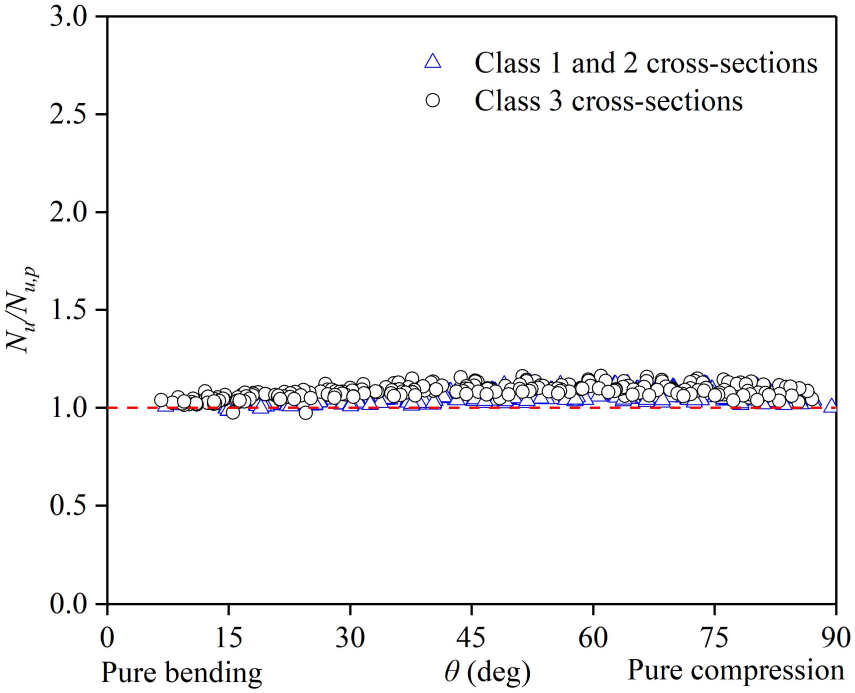

(a) In the 'C' orientation

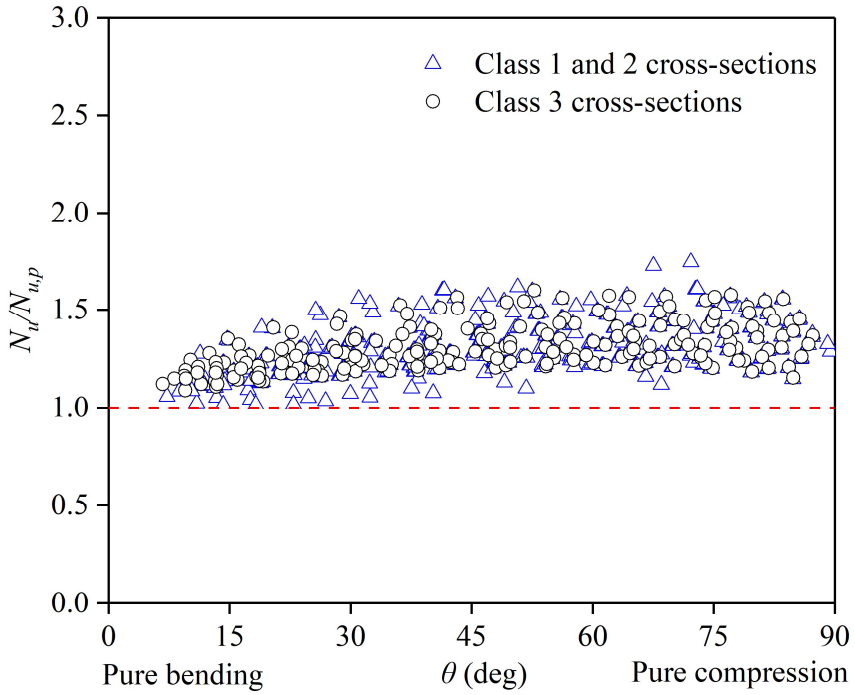

(b) In the 'reverse C' orientation

Figure 7.11. Comparisons of hot-rolled stainless steel channel section beam-column test and FE failure loads with predicted failure loads from new proposal.

The reliability of the proposed design interaction curve for hot-rolled stainless steel channel section beam-columns was evaluated, according to the requirements and procedures given in EN 1990 (CEN 2002). In the present reliability analyses, the material over-strength ratio and the corresponding COV for austenitic stainless steel and the COV of the geometric dimensions of stainless steel members were taken as those in Section 3.5. Table 7.6 reports the key calculated statistical parameters. The resulting (required) partial safety factors γ_{M1}, as reported in Table 7.6, are less than the current limit value of 1.1 in EN 1993-1-4 (CEN 2015), therefore demonstrating the reliability of the proposed design interaction curve for hot-rolled stainless steel channel section beam-columns.

Table 7.6. Reliability analysis results calculated according to EN 1990.

Orientation	No. of data	$k_{d,n}$	b	V_δ	V_r	γ_{M1}
C	666	3.10	1.08	0.03	0.08	0.93
reverse C	675	3.10	1.40	0.09	0.12	0.80
Total	1341	3.10	1.24	0.12	0.14	0.97

7.6 Conclusions

The structural behaviour and load-carrying capacities of hot-rolled stainless steel channel section beam-columns under minor-axis combined loading have been experimentally and numerically studied and presented in this chapter. The testing programme included initial global and local geometric imperfection measurements and ten eccentric compression tests. The key test results, including the failure loads, load–mid-height lateral deflection curves and failure modes with buckling in both the 'C' and 'reverse C' orientations, were presented and discussed. Upon testing, numerical modelling was conducted, where FE models were developed and validated against the test results and then used to perform parametric studies to generate further numerical data over a wide range of cross-section dimensions, member effective lengths and loading combinations. On the basis of the test and numerical failure loads, the current design interaction curves for hot-rolled stainless steel channel section beam-columns, as set out in EN 1993-1-4 (CEN 2015) and ANSI/AISC 370-21

(AISC 2021), were assessed and found to result in inaccurate and scattered failure load predictions, owing to the inaccurate end points and shapes. Finally, a new design interaction curve, anchored to more accurate end points and featuring more proper shape, was proposed to overcome the aforementioned shortcomings. The new design interaction curve was shown to yield accurate, consistent and reliable failure load predictions for hot-rolled stainless steel channel section beam-columns.

CHAPTER 8

CONCLUSIONS AND SUGGESTIONS FOR FUTURE RESEARCH

8.1 Conclusions

In this chapter, the key research findings and conclusions of this thesis are summarised, while more detailed concluding remarks can be found at the end of each chapter. Suggestions for future research are also given.

Experimental and numerical studies of hot-rolled stainless steel channel sections under pure compression have been conducted, as reported in Chapter 3. The experimental programme includes material testing, membrane residual stress measurements, initial local geometric imperfection measurements and six stub column tests. A membrane residual stress predictive model has been developed based on the measured data. It is worth noting that the predictive model for the membrane residual stresses in hot-rolled stainless steel channel sections is the first around the world to be reported in Li et al. (2021a). On the basis of the obtained test and numerical data, the accuracy of the EC3 slenderness limits for the classification of hot-rolled stainless steel outstand and internal plate elements and the codified design rules in EN 1993-1-4 (CEN 2015) and ANSI/AISC 370-21 (AISC 2021) for predicting cross-section compression resistances have been evaluated. The EC3

slenderness limits are overall accurate when adopted for the classification of hot-rolled stainless steel channel sections under pure compression, while the codified EC3 and AISC design rules are found to lead to unduly conservative and scattered cross-section compression resistance predictions, owing principally to the neglect of the beneficial material strain hardening of stainless steel and the favourable cross-section plate element interaction. The advanced continuous strength method (Afshan and Gardner 2013; Zhao et al. 2017) has also been assessed and shown to yield much more accurate and consistent cross-section resistance predictions over the codified design rules, due to the rational exploitation of the favourable material strain hardening and cross-section plate element interaction.

The local buckling behaviour and cross-section resistance of hot-rolled stainless steel channel section stub columns under combined compression and bending have been experimentally and numerically investigated in Chapters 4 and 5. The testing programme, including initial local geometric imperfection measurements, ten eccentrically loaded channel section stub column tests about the major principal axis and ten eccentrically loaded channel section stub column tests about the minor principal axis, has been firstly performed, followed by a numerical modelling programme. Note that these eccentric compression tests on hot-rolled stainless steel channel section stub columns are the first around the world to be reported (Li et al. 2022a, 2022b). The obtained test and numerical results have been employed to assess the accuracy and consistency of the relevant design interaction curves for hot-rolled stainless steel channel sections under combined compression and bending, as provided in EN 1993-1-4 (CEN 2015) and ANSI/AISC 370-21 (AISC 2021). It has been found from the assessment results that the codified design interaction curves result in considerably conservative and scattered cross-section resistance predictions. The conservatism of the codified design interaction curves is attributed to the conservative end points, which are calculated without considering the beneficial strain hardening of stainless steel, and inefficient shape, which fails to consider the favourable stress redistribution within channel section. To address the shortcomings of the codified design interaction curves, new improved design interaction curves, anchored to more accurate CSM end points and featuring more efficient shape, have

been thus developed and found to lead to a much higher level of design accuracy and consistency than their codified counterparts.

The world's first experimental and numerical investigations into the flexural buckling behaviour and resistance of hot-rolled stainless steel channel section columns have been reported in Chapter 6 (Li et al. 2021). An experimental programme includes initial global and local geometric imperfection measurements and pin-ended compression tests on ten hot-rolled stainless steel channel section column specimens. The relevant design buckling curves, as set out in EN 1993-1-4 (CEN 2015) and ANSI/AISC 370-21 (AISC 2021), have been assessed based on the obtained test and numerical data. The EC3 design buckling curve has been found to lead to many unsafe flexural buckling resistance predictions for hot-rolled stainless steel channel section columns with failure in the 'C' orientation, while the AISC design buckling curve results in accurate resistance predictions. Finally, a revised EC3 design buckling curve has been proposed and shown to lead to a much higher level of design accuracy and consistency than the existing version of EN 1993-1-4 (CEN 2015).

In Chapter 7, the global buckling behaviour and resistance of pin-ended hot-rolled stainless steel channel section beam-columns under combined compression and bending moment have been experimentally and numerically studied for the first time around the world (Li et al. 2022c). The experimental programme has been performed on ten hot-rolled stainless steel channel section beam-columns, with five buckling towards webs and the other five buckling towards flange tips. Then, the accuracy of the codified design interaction curves, as set out in EN 1993-1-4 (CEN 2015) and ANSI/AISC 370-21 (AISC 2021), has been assessed based on the obtained test and numerical failure loads. Both the codified design interaction curves have been found to lead to inaccurate and scattered resistance predictions. Finally, a new improved design interaction curve, with more accurate end points and efficient shape, has been developed and found to lead to accurate and consistent resistance predictions for hot-rolled stainless steel channel section beam-columns.

Overall, the cross-section and member behaviour and resistance of hot-rolled stainless steel channel section structural components subjected to isolated and combined loading have been investigated and reported in this thesis. The codified design provisions in the current international design standards and the advanced continuous strength method have been discussed and evaluated, with their advantages and disadvantages discussed. Moreover, a new design buckling curve for hot-rolled stainless steel channel section columns and improved design interaction curves for hot-rolled stainless steel channel section stub columns and beam-columns under combined loading have been developed and shown to lead to a much higher level of design accuracy and consistency. Statistical analyses have also been performed to confirm the reliability of these proposed design approaches. These research findings and new design methods will serve as a reference for future revisions of EN 1993-1-4 (CEN 2015) and ANSI/AISC 370-21 (AISC 2021).

8.2 Suggestions for future work

On the basis of the present research, suggestions for future research on hot-rolled stainless steel channel section members are given herein. First of all, studies on the behaviour and load-carrying capacities of hot-rolled stainless steel channel section members under other loading conditions are required. For example, the global buckling behaviour of hot-rolled stainless steel channel section beam-columns under moment gradients, the crippling buckling behaviour of hot-rolled stainless steel channel sections under flange loading and the in-plane flexural behaviour of hot-rolled stainless steel channel section beams.

The global buckling behaviour of hot-rolled stainless steel channel section columns and beam-columns is sensitive to boundary conditions. Minor-axis pin-ended boundary conditions have been considered in this thesis, while future studies could be performed to examine the global buckling behaviour of hot-rolled stainless steel channel section columns and beam-columns under other boundary conditions, e.g., major-axis pin-ended boundary conditions and fix-ended boundary conditions.

While this thesis focuses on the structural behaviour of hot-rolled stainless steel channel sections, further research on other cross-section profiles, e.g., T-sections, angle sections and cruciform sections can be promoted. Interactive buckling would be triggered for hot-rolled stainless steel structural members with slender cross-sections and special design attention is thus given to the shift in neutral axis for those with slender channel sections.

Finally, the structural behaviour of hot-rolled stainless steel channel section members in fire (at elevated temperatures) and after exposure to fire (after exposure to elevated temperatures) requires studies. Laboratory tests and numerical simulations could be conducted to study their fire and post-fire behaviour and resistance under various loading conditions, followed by the development of efficient design methods.

REFERENCES

ABAQUS. (2014) "ABAQUS/Standard User's Manual Volumes I-III and ABAQUS CAE Manual", Version 6.14, Hibbitt, Karlsson & Sorensen, Inc., Pawtucket, USA.

Ádány, S., and Schafer, B. W. (2008) "A full modal decomposition of thin-walled, single-branched open cross-section members via the constrained finite strip method", Journal of Constructional Steel Research, Vol. 64, No. 1, pp. 12–29.

Afshan, S. and Gardner, L. (2013) "The continuous strength method for structural stainless steel design", Thin-Walled Structures, Vol. 68, pp. 42–49.

Afshan, S., Francis, P., Baddoo, N. R. and Gardner, L. (2015) "Reliability analysis of structural stainless steel design provisions", Journal of Constructional Steel Research, Vol. 114, pp. 293–304.

AISC. (2021) "ANSI/AISC 370-21: Specification for Structural Stainless Steel Buildings", American Instiucte of Steel Construction (AISC), Chicago, USA.

AISI. (1962) "Specification for the Design of Light Gauge Cold-Formed Stainless Steel Structure Members", American Instiucte of Steel Construction (AISC), Washington, D.C., USA.

Anbarasu, M., and Ashraf, M. (2016) "Behaviour and design of cold-formed lean duplex stainless steel lipped channel columns", Thin-walled structures, Vol. 104, pp. 106–115.

Anbarasu, M., and Murugapandian, G. (2016) "Experimental study on cold-formed steel web stiffened lipped channel columns undergoing distortional–global interaction", Materials and Structures, Vol. 49, No. 4, pp. 1433–1442.

Arrayago, I., Real, E. and Gardner, L. (2015) "Description of stress–strain curves for stainless steel alloys", Materials & Design, Vol. 87, pp. 540–552.

ASCE. (2002) "SEI/ASCE 8-02: Specification for the Design of Cold-formed Stainless Steel Structural Members", American Society of Civil Engineers (ASCE), Reston, USA.

Ashraf, M., Gardner, L. and Nethercot, D. A. (2006) "Compression strength of stainless steel cross-sections", Journal of Constructional Steel Research, Vol. 62, No. 1–2, pp. 105–115.

Ashraf, M., Gardner, L. and Nethercot, D. A. (2008a) "Structural stainless steel design: resistance based on deformation capacity", Journal of Structural Engineering (ASCE), Vol. 134, No. 3, pp. 402– 411.

Ashraf, M., Gardner, L. and Nethercot, D. A. (2008b) "Resistance of stainless steel CHS columns based on cross-section deformation capacity", Journal of Constructional Steel Research, Vol. 64, No. 9, pp. 962–970.

Baddoo, N. R. (2008) "Stainless steel in construction: A review of research, applications, challenges and opportunities", Journal of Constructional Steel Research, Vol. 64, No. 11, pp. 1199–1206.

Baddoo, N. R. (2013) "100 years of stainless steel: A review of structural applications and the development of design rules", The Structural Engineer, Vol. 91, pp. 10–18.

Baddoo, N. R., Burgan, R. and Ogden, R. (1997) "Architect's guide to stainless steel", The Steel Construction Institute, UK.

Becque, J. and Rasmussen, K. J. R. (2009a) "Experimental investigation of local-overall interaction buckling of stainless steel lipped channel columns", Journal of Constructional Steel Research, Vol. 65, No. 8–9, pp. 1677– 1684.

Becque, J. and Rasmussen, K. J. R. (2009b) "A numerical investigation of local overall interaction buckling of stainless steel lipped channel columns", Journal of Constructional Steel Research, Vol. 65, No. 8–9, pp. 1685– 1693.

Boissonnade, N., Greiner, R., Jaspart, J. P., and Lindner, J. (2006) "Rules for member stability in EN 1993-1-1: background documentation and design guidelines", ECCS European Convention for constructional steelwork.

BSK. (2003) "BSK 99: Swedish Regulations for Steel Structures", Swedish National Board of Housing, Building and Planning (Boverket), Sweden.

Buchanan, C., Gardner, L. and Liew, A. (2016) "The continuous strength method for the design of circular hollow sections", Journal of Constructional Steel Research, Vol. 118, pp. 207–216.

Buchanan, C., Real, E. and Gardner, L. (2018) "Testing, simulation and design of cold-formed stainless steel CHS columns", Thin-Walled Structures, Vol. 130, pp. 297– 312.

Camotim, D., and Dinis, P. B. (2011) "Coupled instabilities with distortional buckling in cold-formed steel lipped channel columns", Thin-Walled Structures, Vol. 49, No. 5, pp. 562–575.

CEN. (1996) “ENV 1993-1-4: Eurocode 3 – Design of steel structures – Part 1-4: General rules – Supplementary rules for stainless steels”, European Committee for Standardization (CEN), Brussels, Belgium.

CEN. (2002) “EN 1990: Eurocode Basis of structural design”, European Committee for Standardization (CEN), Brussels, Belgium.

CEN. (2006a) “EN 1993-1-4:2006: Eurocode 3 – Design of steel structures – Part 1-4: General rules – Supplementary rules for stainless steels”, European Committee for Standardization (CEN), Brussels, Belgium.

CEN. (2006b) “EN 1993-1-5: Eurocode 3 – Design of steel structures – Part 1-5: Plated structural elements”, European Committee for Standardization (CEN), Brussels, Belgium.

CEN. (2014) “EN 1993-1-1:2005+A1:2014: Eurocode 3 – Design of steel structures – Part 1-1: General rules General rules and rules for buildings”, European Committee for Standardization (CEN), Brussels, Belgium.

CEN. (2015) “EN 1993-1-4:2006+A1:2015: Eurocode 3 – Design of steel structures – Part 1-4: General rules – Supplementary rules for stainless steels, including Amendment A2”, European Committee for Standardization (CEN), Brussels, Belgium.

CEN. (2016) “EN ISO 6892-1: Metallic materials tensile testing – Part 1: Method of test at room temperature”, European Committee for Standardization (CEN), Brussels, Belgium.

Centre for Advanced Structural Engineering. (1990) “Compression tests of stainless steel tubular columns”, Investigation report S770, University of Sydney.

Chen, M. T., and Young, B. (2021) “Beam-column design of cold-formed steel semi-oval hollow non-slender sections”, Thin-Walled Structures, Vol. 162, 107376.

Chen, M., Fan, S., Tao, Y., Li, S., and Liu, M. (2018) “Design of the distortional buckling capacity of stainless steel lipped C-section columns”, Journal of Constructional Steel Research, Vol. 147, pp. 116–131.

Chen, M., Fan, S., Li, C., and Zeng, S. (2020a) “Direct strength method for stainless steel lipped channel columns undergoing local buckling”, International Journal of Steel Structures, Vol. 20, No. 6, pp. 1822–1830.

Chen, M. T., Young, B., Martins, A. D., Camotim, D., and Dinis, P. B. (2020b) “Experimental investigation on cold-formed steel stiffened lipped channel columns undergoing local-distortional interaction”, Thin-Walled Structures, Vol. 150, 106682.

Chen, M., Fan, S., Liu, J., Li, J., Li, D., and Yu, G. (2022) “Design of stainless steel lipped channel columns subjected to distortional-global interactive buckling using the direct strength method”, Thin-Walled Structures, Vol. 179, 109698.

Cruise, R. B. and Gardner, L. (2008) “Residual stress analysis of structural stainless steel sections”, Journal of Constructional Steel Research, Vol. 64, No. 3, 352–366.

Dinis, P. B., and Camotim, D. (2004) “Local-plate and distortional post-buckling behavior of cold-formed steel columns: elastic and elastic–plastic FEM analysis”, Proceedings of SSRC Annual Stability Conference. Atlanta, Georgia,

Dinis, P. B., Camotim, D., Martins, A. D., and Landesmann, A. (2020) “Global-global interaction in cold-formed steel channel columns: relevance, post-buckling behavior, strength and DSM design”, Proceedings of Structural Stability Research Council Annual Stability Conference, RH Jordan, ed. Structural Stability Research Council (SSRC), Atlanta, Georgia.

Dissanayake, D. M. M. P., Pologanathan, K., Gunalan, S., Tsavdaridis, K. D., Nagaratnam, B. and Wanniarachchi, K. S. (2020) "Numerical modelling and shear design rules of stainless steel lipped channel sections", Journal of Constructional Steel Research, Vol. 168, 105873.

Dobrić, J., Buđevac, D., Marković, Z., and Gluhović, N. (2017) "Behaviour of stainless steel press-braked channel sections under compression", Journal of Constructional Steel Research, Vol. 139, pp. 236–253.

Dobrić, J., Ivanović, J., and Rossi, B. (2020) "Behaviour of stainless steel plain channel section columns", Thin-Walled Structures, Vol. 148, 106600.

dos Santos, E. S., Batista, E. M., and Camotim, D. (2012) "Experimental investigation concerning lipped channel columns undergoing local–distortional–global buckling mode interaction", Thin-Walled Structures, Vol. 54, pp. 19–34.

ECCS. (1976) "Manual on Stability of Steel Structures", Second edition, European Convention for Constructional Steelwork (ECCS) – Committee 8 – Stability, Brussels, Belgium.

Euro Inox (1994) "Design Manual for Structural Stainless Steel", First Edition, Steel Construction Institute, UK.

Fan, S., Liu, F., Zheng, B., Shu, G., and Tao, Y. (2014) "Experimental study on bearing capacity of stainless steel lipped C section stub columns", Thin-Walled Structures, Vol. 83, pp. 70–84.

Fan, S., Mo, H., Ding, Z., Zeng, S., and Jiang, Q. (2021) "Research on local buckling capacity of lipped C-section stainless steel beams under weak axis bending", Structures, Vol. 33, pp. 3570–3587.

Fan, S., Wu, Y., Du, L., Liu, M., and Wu, Q. (2022) "Experimental study and numerical simulation analysis of distortional buckling capacity of stainless steel lipped C-section beams", Engineering Structures, Vol. 250, 113428.

Galambos, T. V., and Ketter, R. L. (1959) "Columns under combined bending and thrust", Journal of the Engineering Mechanics Division, Vol. 85, No. 2, pp. 1–30.

Gardner, L. (2002) "A new approach to structural stainless steel design", PhD Thesis. Department of Civil and Environmental Engineering, Imperial College London, UK.

Gardner, L. (2005) "The use of stainless steel in structures", Progress in Structural Engineering and Materials, London, UK, Vol. 7, No. 2, pp. 45–55.

Gardner, L. (2008a) "Aesthetics, economics and design of stainless steel structures", Advanced Steel Construction, Vol. 4, No. 2, pp. 113– 122.

Gardner, L. (2008b) "The continuous strength method", Proceedings of the Institution of Civil Engineers-Structures and Buildings, Vol. 161, No. 3, pp. 127–133.

Gardner, L. (2019) "Stability and design of stainless steel structures–Review and outlook", Thin-Walled Structures, Vol. 141, pp. 208– 216.

Gardner, L. and Ashraf, M. (2006) "Structural design for non-linear metallic materials", Engineering Structures, Vol. 28, No. 6, pp. 926–934.

Gardner, L., and Cruise, R. B. (2009) "Modeling of residual stresses in structural stainless steel sections", Journal of Structural Engineering (ASCE), Vol. 135, No. 1, pp. 42–53.

Gardner, L. and Nethercot, D. A. (2004) "Experiments on stainless steel hollow sections–Part 1: Material and cross-sectional behaviour", Journal of Constructional Steel Research, Vol. 60, No. 9, pp. 1291– 1318.

Gedge, G. (2008) "Structural uses of stainless steel – buildings and civil engineering", Journal of Constructional Steel Research, Vol. 64, No. 11, pp. 1194–1198.

Greiner, R., and Lindner, J. (2006) "Interaction formulae for members subjected to bending and axial compression in Eurocode 3—the Method 2 approach", Journal of Constructional Steel Research, Vol. 62, No. 8, pp. 757–770.

Gunalan, S., and Mahendran, M. (2013) "Improved design rules for fixed ended cold-formed steel columns subject to flexural–torsional buckling", Thin-Walled Structures, Vol. 73, pp. 1–17.

Hill, H. N. (1944) "Determination of stress-strain relations from offset yield strength values", National Advisory Committee for Aeronautics, Technical Note No. 927, Washington, DC, USA.

Hradil, P., Talja, A., Real, E., Mirambell, E. and Rossi, B. (2013) "Generalized multistage mechanical model for nonlinear metallic materials", Thin-Walled Structures, Vol. 63, pp. 63– 69.

Huang, Y. and Young, B. (2012) "Material properties of cold-formed lean duplex stainless steel sections", Thin-Walled Structures, Vol. 54, pp. 72– 81.

Huang, Y. and Young, B. (2014) "Structural performance of cold-formed lean duplex stainless steel columns", Thin-Walled Structures, Vol. 83, pp. 59– 69.

Kuwamura, H. (2003) "Local buckling of thin-walled stainless steel members", Steel Structures, Vol. 3, No. 3, pp. 191–201.

Kwon, Y. B., and Hancock, G. J. (1992) “Tests of cold-formed channels with local and distortional buckling”, Journal of structural engineering (ASCE), Vol. 118, No. 7, pp. 1786–1803.

Kwon, Y. B., Kim, N. G., and Hancock, G. J. (2007) “Compression tests of welded section columns undergoing buckling interaction”, Journal of Constructional Steel Research, Vol. 63, No. 12, pp. 1590–1602.

Kwon, Y. B., Kim, B. S., and Hancock, G. J. (2009) “Compression tests of high strength cold-formed steel channels with buckling interaction”, Journal of Constructional Steel Research, Vol. 65, No. 2, pp. 278–289.

Lan, X., Li, S., and Zhao, O. (2021) “Local buckling of hot-rolled stainless steel channel section stub columns after exposure to fire”, Journal of Constructional Steel Research, Vol. 187, pp. 106950.

Lay, M. G., and Ward, R (1969) “Residual stresses in steel sections”, Journal of the Australian Steel Institute, Vol. 3, No. 3, pp. 2–21.

Lecce, M. and Rasmussen, K. J. R. (2006a) “Distortional buckling of cold-formed stainless steel sections: experimental investigation”, Journal of Structural Engineering (ASCE), Vol. 132, No. 4, pp. 497– 504.

Lecce, M., and Rasmussen, K. (2006b) “Distortional buckling of cold-formed stainless steel sections: Finite-element modeling and design”, Journal of Structural Engineering (ASCE), Vol. 132, No. 4, pp. 505–514.

Li, S., Zhang, L., Liang, Y., and Zhao, O. (2021a) “Experimental and numerical investigations of hot-rolled stainless steel channel section columns susceptible to flexural buckling”, Thin-Walled Structures, Vol. 164, pp. 107791.

Li, S., Zhang, L., and Zhao, O. (2022a) "Cross-section behavior and design of hot-rolled stainless steel channel sections under major-axis combined loading", Journal of Structural Engineering (ASCE), Vol. 148, No. 8, 04022110.

Li, S., Zhang, L., and Zhao, O. (2022b) "Testing, modelling and design of hot-rolled stainless steel channel sections under combined compression and minor-axis bending moment", Thin-Walled Structures, Vol. 172, 108836.

Li, S., Zhang, L., and Zhao, O. (2022c) "Global buckling and design of hot-rolled stainless steel channel section beam–columns", Thin-Walled Structures, Vol. 170, 108433.

Li, Y. C., Zhou, T. H., Sang, L. R., and Zhang, L. (2020) "Design method for cold-formed steel u-section short columns", Advanced Steel Construction, Vol. 16, No. 2, pp. 146–155.

Li, Y., Zhou, T., Li, D., Ding, J., and Li, C. (2021b) "Experimental investigation and design of cold-formed steel U-section columns with the local and global interactive buckling", Structures, Vol. 33, pp. 3371–3381.

Li, Z., and Schafer, B. W. (2010) "Buckling analysis of cold-formed steel members with general boundary conditions using CUFSM conventional and constrained finite strip methods", Proceedings of the 20th International Specialty Conference on Cold-Formed Steel Structures, Orlando, FL, USA.

Liang, Y., Zhao, O., Long, Y. L. and Gardner, L. (2019a) "Stainless steel channel sections under combined compression and minor axis bending–Part 1: Experimental study and numerical modelling", Journal of Constructional Steel Research, Vol. 152, pp. 154–161.

Liang, Y., Zhao, O., Long, Y. L. and Gardner, L. (2019b) "Stainless steel channel sections under combined compression and minor axis bending–Part 2: Parametric studies and design", Journal of Constructional Steel Research, Vol. 152, pp. 162–172.

Liang, Y., Zhao, O., Long, Y. L. and Gardner, L. (2020) "Experimental and numerical studies of laser-welded stainless steel channel sections under combined compression and major axis bending moment", Thin-Walled Structures, Vol. 157, 107035.

Liew, A. and Gardner, L. (2015) "Ultimate capacity of structural steel cross-sections under compression, bending and combined loading", Structures, Vol. 1, pp. 2–11.

Maduliat, S., Bambach, M. R., and Zhao, X. L. (2012) "Inelastic behaviour and design of cold-formed channel sections in bending", Thin-walled structures, Vol. 51, pp. 158–166.

Madugula, M. K. S., Haidur, R., Monforton, G. R., and Marshall, D. G. (1997) "Additional residual stress and yield stress test on hot-rolled angles", Proceedings of the Structural Stability Research Council Annual Technical Session, Toronto, pp. 55–68.

Mahar, A. M., Jayachandran, S. A., and Mahendran, M. (2021) "Direct strength method for cold-formed steel unlipped channel columns subject to local buckling", International Journal of Steel Structures, Vol. 21, No. 6, pp. 1977–1987.

Mirambell, E. and Real, E. (2000) "On the calculation of deflections in structural stainless steel beams: an experimental and numerical investigation", Journal of Constructional Steel Research, Vol. 54, No. 1, pp. 109–133.

Quach, W. M., Teng, J. G. and Chung, K. F. (2008) "Three-stage full-range stress strain model for stainless steel", Journal of Structural Engineering (ASCE), Vol. 134, No. 9, pp. 1518–1527.

Ramberg, W. and Osgood, W. R. (1943) "Description of stress strain curves by three parameters", National Advisory Committee for Aeronautics, Technical Note No. 902, Washington, DC, USA.

Rasmussen, K. J. R., and Hancock, G. J. (1989) "Compression tests of welded channel section columns", Journal of Structural Engineering (ASCE), Vol. 115, No. 4, pp. 789–808.

Rasmussen, K. J. R. (2003) "Full-range stress strain curves for stainless steel alloys", Journal of Constructional Steel Research, Vol. 59, No. 1, pp. 47– 61.

Rossi, B., Jaspart, J. P. and Rasmussen, K. J. R. (2010a) "Combined distortional and overall flexural-torsional buckling of cold-formed stainless steel sections: experimental investigations", Journal of Structural Engineering (ASCE), Vol. 136, No. 4, pp. 354–360.

Rossi, B., Jaspart, J. P. and Rasmussen, K. J. R. (2010b) "Combined distortional and overall flexural-torsional buckling of cold-formed stainless steel sections: design", Journal of Structural Engineering (ASCE), Vol. 136, No. 4, pp. 361–369.

Saliba, N. and Gardner, L. (2013) "Cross-section stability of lean duplex stainless steel welded I-sections", Journal of Constructional Steel Research, Vol. 80, pp. 1–14.

Santos, E. S., Dinis, P. B., Batista, E. M., and Camotim, D. (2014) "Cold-formed steel lipped channel columns undergoing local-distortional-global interaction: experimental and numerical investigation", Proceedings of the 22nd International Specialty Conference on Cold-Formed Steel Structures, Orlando, FL, USA, pp. 193–211.

Schafer, B. W. and Ádány, S. (2006) "Buckling analysis of cold-formed steel members using CUFSM: conventional and constrained finite strip methods",

Proceedings of the 18th International Specialty Conference on Cold-Formed Steel Structures, Orlando, FL, USA.

Schafer, B. W. and Peköz, T. (1998) "Computational modelling of cold-formed steel: characterizing geometric imperfections and residual stresses", Journal of Constructional Steel Research, Vol. 47, No. 3, pp. 193–210.

Schafer, B. W. (2002) "Local, distortional, and Euler buckling of thin-walled columns", Journal of structural engineering (ASCE), Vol. 128, pp. 289–299.

Schafer, B. W. (2008) "The direct strength method of cold-formed steel member design", Journal of constructional steel research, Vol. 64, pp. 766–778.

Schafer, B. W. (2019) "Advances in the Direct Strength Method of cold-formed steel design", Thin-Walled Structures, Vol. 140, pp. 533–541.

Sivakumaran, K. S., and Abdel-Rahman, N. (1998) "A finite element analysis model for the behaviour of cold-formed steel members", Thin-walled structures, Vol. 31, No. 4, pp. 305–324.

Silvestre, N., and Camotim, D. (2006) "Local-plate and distortional post-buckling behavior of cold-formed steel lipped channel columns with intermediate stiffeners", Proceedings of the 17th International Specialty Conference on Cold-Formed Steel Structures, Orlando, FL, USA, pp. 1–18.

Shanmugam, N. E., and Dhanalakshmi, M. (2001) "Design for openings in cold-formed steel channel stub columns", Thin-walled structures, Vol. 39, No. 12, pp. 961–981.

Sun, Y., Liu, Z., Liang, Y. and Zhao, O. (2019) "Experimental and numerical investigations of hot-rolled austenitic stainless steel equal-leg angle sections", Thin-Walled Structures, Vol. 144, 106225.

Sun, Y. and Zhao, O. (2019) “Material response and local stability of high-chromium stainless steel welded I-sections”, Engineering Structures, Vol. 178, pp. 212–226.

Szalai, J., and Papp, F. (2005) “A new residual stress distribution for hot-rolled I-shaped sections”, Journal of Constructional Steel Research, Vol. 61, No. 6, pp. 845–861.

Tebedge, N., Alpsten, G., and Tall, L. J. E. M. (1973) “Residual-stress measurement by the sectioning method”, Experimental Mechanics, Vol. 13, No. 2, pp. 88–96.

Theofanous, M., Liew, A. and Gardner, L. (2015) “Experimental study of stainless steel angles and channels in bending”, Structures, Vol. 4, pp. 80–90.

Torabian, S., Zheng, B., and Schafer, B. W. (2014) “Development of a new beam-column design method for cold-formed steel lipped channel members”, Proceedings of the 22nd International Specialty Conference on Cold-Formed Steel Structures, Orlando, FL, USA, pp. 359–375.

Torabian, S., Zheng, B., and Schafer, B. W. (2015) “Experimental response of cold-formed steel lipped channel beam-columns”, Thin-walled structures, Vol. 89, pp. 152–168.

Torabian, S., and Schafer, B. W. (2018) “Development and experimental validation of the direct strength method for cold-formed steel beam-columns”, Journal of Structural Engineering (ASCE), Vol. 144, No. 10, 04018175.

Ungermann, D., Brune, B., and Lübke, S. (2012a) “Experimental investigations on plain channels in coupled instabilities”, Steel Construction, Vol. 5, No. 2, pp. 87–92.

Ungermann, D., Brune, B., and Lübke, S. (2012b) "Numerical and analytical investigations on plain channels in coupled instabilities", Steel Construction, Vol. 5, No. 4, pp. 205–211.

Ungermann, D., Lübke, S., and Brune, B. (2014) "Tests and design approach for plain channels in local and coupled local-flexural buckling based on Eurocode 3", Thin-walled structures, Vol. 81, pp. 108–120.

Wang, C., Zhang, Z., Zhao, D., and Liu, Q. (2016) "Compression tests and numerical analysis of web-stiffened channels with complex edge stiffeners", Journal of constructional steel research, Vol. 116, pp. 29–39.

Wang, F., Zhao, O., and Young, B. (2019) "Flexural behaviour and strengths of press-braked S960 ultra-high strength steel channel section beams", Engineering Structures, 200, 109735.

Wang, F., Zhao, O. and Young, B. (2020a) "Testing and numerical modelling of S960 ultra-high strength steel angle and channel section stub columns", Engineering Structures, Vol. 204, 109902.

Wang, F., Liang, Y. and Zhao, O. (2020b) "Experimental and numerical studies of pin-ended press-braked S960 ultra-high strength steel channel section columns", Engineering Structures, Vol. 215, 110629.

Winter, G. (1947) "Strength of thin steel compression flanges", Transactions of the American Society of Civil Engineers, 112(1), pp. 527–554.

Xiang, Y., Zhou, X., Shi, Y., Xu, L. and Xu, Y. (2020) "Experimental investigation and finite element analysis of cold-formed steel channel columns with complex edge stiffeners", Thin-Walled Structures, Vol. 152, 106769.

Yan, J., and Young, B. (2002) “Column tests of cold-formed steel channels with complex stiffeners”, Journal of Structural Engineering (ASCE), Vol. 128, No. 6, pp. 737–745.

Yang, D., and Hancock, G. J. (2004) “Compression tests of high strength steel channel columns with interaction between local and distortional buckling”, Journal of Structural Engineering (ASCE), Vol. 130, No. 12, pp. 1954–1963.

Ye, J., Hajirasouliha, I., and Becque, J. (2018a) “Experimental investigation of local-flexural interactive buckling of cold-formed steel channel columns”, Thin-walled structures, Vol. 125, pp. 245–258.

Ye, J., Mojtabaei, S. M., and Hajirasouliha, I. (2018b) “Local-flexural interactive buckling of standard and optimised cold-formed steel columns”, Journal of constructional steel research, Vol. 144, pp. 106–118.

Young, BW. (1972) “Residual stresses in hot-rolled members”, IABSE international colloquium on column strength.

Young, B. (2004) “Design of channel columns with inclined edge stiffeners”, Journal of Constructional Steel Research, Vol. 60, No. 2, pp. 183–197.

Young, B., and Rasmussen, K. J. R. (1995) “Compression tests of fixed-ended and pin-ended cold-formed plain channels”.

Young, B., and Rasmussen, K. J. (1998a) “Tests of fixed-ended plain channel columns”, Journal of Structural Engineering (ASCE), Vol. 124, No. 2, pp. 131–139.

Young, B., and Rasmussen, K. J. (1998b) “Shift of the effective centroid of channel columns”, Proceedings of the 14th International Specialty Conference on Cold-Formed Steel Structures, Orlando, FL, USA, pp. 265–287.

Young, B., and Rasmussen, K. J. (1998c) "Design of lipped channel columns", Journal of Structural Engineering (ASCE), Vol. 124, No. 2, pp. 140–148.

Young, B., and Rasmussen, K. J. (1999) "Behaviour of cold-formed singly symmetric columns", Thin-walled structures, Vol. 33, No. 2, pp. 83–102.

Young, B., and Hancock, G. J. (2003) "Compression tests of channels with inclined simple edge stiffeners", Journal of Structural Engineering (ASCE), Vol. 129, No. 10, 1403–1411.

Young, B., Dinis, P. B., and Camotim, D. (2018) "CFS lipped channel columns affected by LDG interaction. Part I: Experimental investigation", Computers & Structures, Vol. 207, pp. 219–232.

Young, B., Silvestre, N., and Camotim, D. (2013) "Cold-formed steel lipped channel columns influenced by local-distortional interaction: strength and DSM design", Journal of structural Engineering (ASCE), Vol. 139, No. 6, pp. 1059–1074.

Yu, C., and Schafer, B. W. (2002) "Local buckling tests on cold-formed steel beams", Proceedings of the 16th International Specialty Conference on Cold-Formed Steel Structures, Orlando, FL, USA.

Yu, C., and Schafer, B. W. (2006) "Distortional buckling tests on cold-formed steel beams", Proceedings of the 17th International Specialty Conference on Cold-Formed Steel Structures, Orlando, FL, USA.

Zhang, Y., Wang, C., and Zhang, Z. (2007) "Tests and finite element analysis of pin-ended channel columns with inclined simple edge stiffeners", Journal of Constructional Steel Research, Vol. 63, No. 3, pp. 383–395.

Zhang, L., Wang, F., Liang, Y., and Zhao, O. (2019) "Press-braked S690 high strength steel equal-leg angle and plain channel section stub columns: Testing, numerical simulation and design", Engineering Structures, Vol. 201, 109764.

Zhang, L., Tan, K. H. and Zhao, O. (2020a) "Local stability of press-braked stainless steel angle and channel sections: Testing, numerical modelling and design analysis", Engineering Structures, Vol. 203, 109869.

Zhang, L., Tan, K. H. and Zhao, O. (2020b) "Press-braked stainless steel channel section columns failing by flexural buckling: Testing, numerical simulation and design", Thin-Walled Structures, Vol. 157, 107066.

Zhang, L., Wang, F., Liang, Y., and Zhao, O. (2020c) "Experimental and numerical studies of press-braked S690 high strength steel channel section beams", Thin-Walled Structures, Vol. 148, 106499.

Zhang, L., Li, S., Tan, K. H. and Zhao, O. (2021a) "Experimental and numerical investigations of press-braked stainless steel channel section beam-columns", Thin-Walled Structures, Vol. 161, 107344.

Zhang, L., Zhong, Y. and Zhao, O. (2021b) "Experimental and numerical investigations of press-braked stainless steel channel sections under minor-axis combined loading", Thin-Walled Structures, Vol. 166, 108049.

Zhang, L., Zhong, Y. and Zhao, O. (2021c) "Press-braked stainless steel channel sections under major-axis combined loading: tests, simulations and design", Journal of Constructional Steel Research, Vol. 187, 106932.

Zhang, L., Liang, Y., and Zhao, O. (2022) "Experimental and numerical study of press-braked S690 high-strength steel channel–section columns failing by minor-axis flexural buckling", Journal of Structural Engineering (ASCE), Vol. 148, No. 8, 04022094.

Zhang, L., and Zhao, O. (2022) "Experimental and numerical study of press-braked S690 high strength steel slender channel section columns prone to local–flexural interactive buckling", Engineering Structures, Vol. 264, 114468.

Zhao, O., Afshan, S. and Gardner, L. (2017) "Structural response and continuous strength method design of slender stainless steel cross-sections", Engineering Structures, Vol. 140, pp. 14–25.

Zhao, O. and Gardner, L. (2018) "The continuous strength method for the design of mono-symmetric and asymmetric stainless steel cross-sections in bending", Journal of Constructional Steel Research, Vol. 150, pp. 141–152.

Zhao, O., Gardner, L., and Young, B. (2016a) "Structural performance of stainless steel circular hollow sections under combined axial load and bending–Part 1: Experiments and numerical modelling", Thin-Walled Structures, Vol. 101, pp. 231–239.

Zhao, O., Gardner, L., and Young, B. (2016b) "Structural performance of stainless steel circular hollow sections under combined axial load and bending–Part 2: Parametric studies and design", Thin-Walled Structures, Vol. 101, pp. 240–248.

Zhao, O., Rossi, B., Gardner, L. and Young, B. (2016c) "Experimental and numerical studies of ferritic stainless steel tubular cross sections under combined compression and bending", Journal of Structural Engineering (ASCE), Vol. 142, No. 2, 04015110.

Zhao, O., Gardner, L., and Young, B. (2016d) "Testing and numerical modelling of austenitic stainless steel CHS beam–columns", Engineering Structures, Vol. 111, pp. 263–274.

Zhao, O., Rossi, B., Gardner, L., and Young, B. (2015a) "Behaviour of structural stainless steel cross-sections under combined loading–Part I: Experimental study", Engineering Structures, Vol. 89, pp. 236–246.

Zhao, O., Rossi, B., Gardner, L., and Young, B. (2015b) "Behaviour of structural stainless steel cross-sections under combined loading–Part II: Numerical modelling and design approach", Engineering Structures, Vol. 89, pp. 247–259.

Zhou, F. and Young, B. (2020) "Web crippling of aluminium alloy channel sections with flanges restrained", Thin-Walled Structures, Vol. 148, 106576.

Zhu, J. H., Li, Z. Q., Su, M. N. and Young, B. (2019) "Behaviour of aluminium alloy plain and lipped channel columns", Thin-Walled Structures, Vol. 135, pp. 306–316.

Ziemian, R. D. (2010) "Guide to Stability Design Criteria for Metal Structures", Sixth Editions, John Wiley & Sons, Inc., Hoboken, New Jersey, US.